UNIVERSITY OF CALIFORNIA
RIVERSIDE

Spin Dynamics of Two-Magnet Heterostructure Nanodevices

A Dissertation submitted in partial satisfaction
of the requirements for the degree of

Doctor of Philosophy

in

Physics

by

Bassim Saleh Arkook

September 2020

Dissertation Committee:

Dr. Igor Barsukov, Chairperson
Dr. Jing Shi
Dr. Peng Wei

The Dissertation of Bassim Saleh Arkook is approved:

Committee Chairperson

University of California, Riverside

Acknowledgments

I am grateful to my advisor Dr. Igor Barsukov, for his help and supporting my adventure of scientific insight; he is a person of distinguished knowledge, experience, and incredibly humble. It is a great honor to be his first Ph.D. student who graduated from his group. I would also like to thank the dissertation committee members, Dr. Jing Shi and Dr. Peng Wei, for their time and effort on examining my dissertation.

I want to reveal my gratitude to my previous advisor Prof. Robert Haddon (died on April 21, 2016), without whose assistant and guidance I would not have been here. It was one of my goals to complete my Ph.D. under his supervision, but there is nothing more painful than the untimely death of someone dear to the heart.

I would like to acknowledge everyone whom I had the pleasure to work with over the years: Dr. Victor Ortiz, Dr. Mingguang Chen, Dr. Matthew Moser, Wangxiang Li, Dr. Dejan Stekovic, Dr. Guanghui Li, Dr. Mikhail E. Itkis, Dr. Elena Bekyarova, Dr. Sakhrat Khizroev, Dr. Ilya N Krivorotov, Dr. Christopher Safranski, Dr. Jing Shi, Dr. Junxue Li, Dr. Mohammed Aldosary, David Nelson, Rodolfo Rodriguez, Arezoo Etesamirad, Esther Cookson, Hassan Alghamdi, Abdulrahman Albariqi, Mohammed Alghamdi, Shirash Regmi, Erik Hagen, Abdullah Almujtabi, Nancy Jahr and Dr. Yas Al-Hadeethi.

I would also like to thank my parents, Saleh Arkook and Fatimah Abdulraheem, and my brothers, Samir and Samer, for their love, unlimited support, and honest prayers. I want to thank my wife, Sarah Iwaza, for her powerful, irresistible brightness, never-ending care of our kids and house. Lastly, I would also like to acknowledge the scholarship fund from King Abdulaziz University granted to me to accomplish my Ph.D. degree.

To my parents for all the moral support.

To my wife for all the true love.

To my kids; my lovely world.

ABSTRACT OF THE DISSERTATION

Spin Dynamics of Two-Magnet Heterostructure Nanodevices

by

Bassim Saleh Arkook

Doctor of Philosophy, Graduate Program in Physics
University of California, Riverside, September 2020
Dr. Igor Barsukov, Chairperson

Spintronics research bears great potential for advancing information technologies and strengthen this rapidly developing sector of the economy. The ever-growing thirst for smaller and faster information technologies is accompanied by the urgent need to design them to be energy-efficient. This challenge is met by developing novel concepts that may promise substantial performance improvement of future spintronics applications.

In this work, the two-magnet paradigm is explored. Its main idea lies in combining two magnetic materials within one spintronic device to tailor its magnetic properties/parameters in a way that would not be achievable with a single magnetic material. Generally, a combination of magnetic materials within one heterostructure is considered to complicate the spin physics of such a device significantly and thus typically avoided.

Recent developments in spin-orbitronics have pushed metallic ferromagnets into the focus of research due to the plethora of spin-charge effects with unusual symmetries. These effects may enable the designing of novel spintronics applications that have been considered unrealistic. On the other hand, magnetic insulators have proven to be beneficial

spintronic materials by dint of their low magnetic damping, lack of electrical shunting, and magnetic tunability by growth parameters.

The spin physics of the two-magnet heterostructures is explored by directly interfacing magnetic insulator with a metallic ferromagnet in a nanoscale multilayer device. By carrying out microwave spectroscopy on the nanodevices, spin-wave modes are observed that, as supported by micromagnetic simulations, delocalize over both layers and show features of hybridized spin dynamics. By applying the temperature gradient across the nanodevice layers, thermal spin currents are studied, resulting in magnetic auto-oscillations. These auto-oscillations are a manifestation of a thermally driven condensation of hybrid magnons – a phenomenon that is novel from both experimental and theoretical standpoint. The auto-oscillations are converted into sizeable electric microwave signals under large spin-charge effects inherent to ferromagnetic metals. The results indicate that the two-magnet paradigm brings significant performance improvements for spintronics applications such as spin-torque oscillators, magnetic memory, and neuromorphic networks.

The paradigm is further explored by studying the effect of large thermal and spin-orbit torques on the hybridized spin dynamics of the two-magnet heterostructures. A critical phenomenon is observed that manifests through the formation of a solitonic dynamic mode in the heterostructure. While a satisfying theoretical model is yet to be developed, the experimental data suggest that a breathing domain wall forms in the nanodevice. The soliton oscillates at microwave frequencies below but comparable to the spin-wave frequencies and results in microwave emission with powers that exceed those of a spin torque oscillator by about three orders of magnitude. This observation suggests that the two-magnet devices

could be used in magnetic switching and magnetic memory applications.

The two-magnet paradigm is further advanced by exchanging metallic ferromagnets with novel van der Waals two-dimensional magnetic layers. The 2D magnets are usually deposited by exfoliation, which results in laterally micrometer size confined flakes. Thus, an approach for designing and fabricating microscale two-magnet heterostructures has been developed. Moreover, inductive microwave spectroscopy technique with a sensitivity allowing for exploring such microstructures has been developed and tested. The data suggest hybridization of spin-wave modes in the magnetic insulator with critical spin fluctuations of the 2D magnetic subsystem, occurring near the van der Waals magnet's magnetic phase transitions. The results open new avenues for research on two-magnet heterostructures with 2D magnets to advance future spintronics technologies.

This work does not give an exhaustive answer to the question on the future of the two-magnet heterostructures in spintronics technologies. However, it presents preliminary data that points out the paradigm's potential and seeks to advance understanding of the related spin physics that may be critical and instructive for the research to come.

Contents

List of Figures

Chapter 1

Introduction

1.1 Motivation

Spin electronics materials are expected to revolutionize the information technologies by providing energy-efficient magnetic devices for storage, sensing, processing, and transmission of information [1]. Many of the existing and proposed devices rely on spin torques, which are used to control the magnetization dynamics and to manipulate the magnetic state of a nanoscale device [2]. The prominent examples are magnetic switching devices (such as spin torque memory [3, 4]) and spin-torque oscillators (STO) [5, 6]. STOs can be used to detect sensitive microwave signals and create local microwave fields, which, e.g., can be employed to assist the magnetic writing in hard drives [7]. STO can transmit information by emitting spin waves into a magnonic waveguide [8, 9, 10]. STOs also exhibit a nonlinear phenomenon that makes them particularly attractive device candidates within the emerging paradigm of neuromorphic computing [11, 12, 13].

The central prerequisite for the design and realization of spin-torque devices is

the energy-efficient generation of customized spin torques. Spin torques are exerted by spin currents injected into a magnetic device element, e.g., into a ferromagnetic layer. Over the last decades, the focus has been shifting from the generation of spin currents by spin-polarized electrical currents towards pure spin currents, since the latter does not directly involve mass/charge transport, reducing the detrimental effects of energy losses and electromigration in nanoscale devices [1, 14].

One of the most hopeful techniques of producing and utilizing tailored spin currents is thermal spin current due to the spin Seebeck effect. Spintronic devices built to utilize thermal spin currents will be often based on magnetic insulators, that lack sufficient spin-charge effects, and magnetoresistance present in ferromagnetic metals. On the other hand, employing novel spintronic materials, such as magnetic van der Waals (vdW) 2D layers can present a challenge to well-established methods in spintronics. This work proposes a new concept – the two-magnet paradigm. A combination of properties – the virtues of each material – can be harnessed by combining two magnetic systems in a multilayer structure. Such a combination of materials, however, has long been considered a severe complication for studying spin transport and spin dynamics. Here, several examples and potential concepts for spintronics applications will be presented to show how to circumvent the difficulties of heterogeneous magnetic systems and extract benefits from them.

1.2 Outline

This dissertation is structured as follows:

Chapter 2 introduces the significant theoretical aspects needed to understand

the data presented in the dissertation. Various sources of magnetoresistance and pure spin currents are discussed. This chapter includes the formulation of a theoretical framework, which is necessary since some of the presented results yet lack a well-established theoretical basis.

Chapter 3 introduces experimental methods used to obtain the results presented in this dissertation. This includes broadband ferromagnetic resonance (FMR), spin-torque FMR, magnetoresistance, microwave emission spectroscopy, and micromagnetic simulation. This chapter does not only present well-established methods, but also shows the developments in the experiment, data processing, and simulation, that were developed in the course of this work.

Chapter 4 discussed the two-magnet nano-oscillator, developed and realized in this work. Experimental data and theoretical concepts are presented and followed by a discussion on the prospects of heterogeneous magnetic systems for spintronics.

Chapter 5 presents an observation of auto-oscillatory solitonic excitation in the two-magnet nanowires.

Chapter 6 introduces the magnetic properties of a single micrometer-sized YIG/FGT heterostructure revealed by ferromagnetic resonance. The results shed light on spin phenomena at YIG/FGT interface and present an experimental approach for studies of microscale magnetic insulator/2D heterostructure.

Chapter 7 presents a summary of the dissertation.

Chapter 2

Background and Formulation of Theoretical Framework

2.1 Magnetization dynamics

The motion of the magnetization vector $\vec{M}$, is generally described by the Landau–Lifshitz (LL) equation [15, 16]. This differential equation which, in general, results in solutions describing the precessional motion of magnetization. With time, the LL equation has received many modifications to account for different damping mechanisms [16] and torques acting on the magnetization. First, the original equation shall be discussed [15]:

$$\frac{\mathrm{d}\vec{M}}{\mathrm{d}t} = -\gamma\vec{M} \times \vec{H}_{eff} - \frac{\lambda}{M^2}\vec{M} \times (\vec{M} \times \vec{H}_{eff}) \tag{2.1}$$

where γ is the gyromagnetic ratio, $\vec{H}_{eff}$ is the effective magnetic field which is a combination of the demagnetizing field, the external magnetic fields, and magnetic anisotropy fields, and

$\lambda \sim \alpha\gamma M_s$ is a phenomenological damping parameter, where α is the Gilbert damping factor [16] and M_s is the saturation magnetization (see figure 2.1).

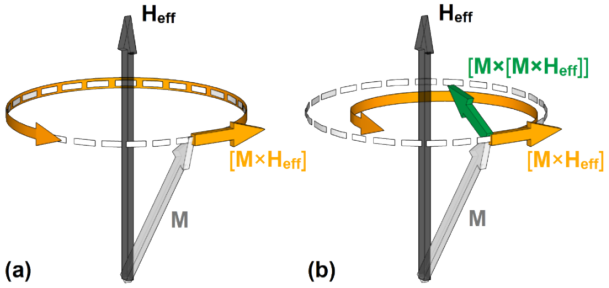

Figure 2.1: Schematic of the magnetization $\vec{M}$ undergoes a damped precession motion around $\vec{H}_{eff}$, (a) undamped motion and (b) motion with damping. Adapted from Ref. [17]

The modification of the LL equation by Gilbert [16] implements a more realistic damping term within the Landau-Lifshitz-Gilbert (LLG) equation:

$$\frac{\mathrm{d}\vec{M}}{\mathrm{d}t} = -\gamma\, \vec{M} \times \vec{H}_{eff} + \frac{\alpha}{M}\vec{M} \times \frac{\mathrm{d}\vec{M}}{\mathrm{d}t} \tag{2.2}$$

The first torque is the conservative field torque (precession) that causes the magnetization to precess around the effective field direction. The second torque is the non-conservative damping torque that tends to align magnetization with the effective field direction in the absence of a drive. While the Gilbert damping describes the motion of magnetization better than the LL damping term, the LLG differential equation is typically more complicated to solve. In particular micromagnetic methods (described further below) typically rely on the LL equation. Moreover, the introduction of further torques acting on the magnetization is mathematically and phenomenologically simpler within the LL equation. Recalculation between the LL and LLG equation requires, strictly speaking, a renormalization of the gyromagnetic ratio and the damping parameter. However, such renormalization can typically

be omitted since it is of the order of α^2 and very small.

2.1.1 Spin torque

Flows of angular momentum into, through, and within magnetic systems can generally be referred to as spin currents. Spin currents may interact with the magnetic system in a rather complicated manner. To discuss this interaction, first, a magnetic system shall be considered into which a spin current is deposited. For simplicity, the carrier of the spin current shall be a spin-polarized electron current. The action of an injected spin current onto the magnetization can be accounted for by the introduction of two terms [18]:

$$\frac{\mathrm{d}\vec{M}}{\mathrm{d}t} = -\gamma\vec{M}\times\vec{H}_{eff} - \frac{\lambda}{M^2}\vec{M}\times\vec{M}\times\vec{H}_{eff} + \beta\ \vec{M}\times\vec{M}\times\widehat{\sigma} + \beta^*\ \vec{M}\times\widehat{\sigma} \tag{2.3}$$

where β and β^* are two independent transverse interface conductances, and $\widehat{\sigma}$ is the spin current polarization.

The symmetry of the torques indicated that the first term, referred to as Slonczewski torque, has the same symmetry as the LL damping torque with spin polarization components in the direction of the effective field. It is thus often called damping-like torque. The second term has the equivalent symmetry as the precessional term and thus often referred to as field-like torque. The prefactors of the torques is a complicated function of the multiple parameters that depend on the nature of the spin currents and magnet interfaces. However, both scales linearly with the magnitude of the injected spin current.

When the spin current polarization $\widehat{\sigma}$ has a non-zero component in the direction of the effective field, the damping-like torque renormalizes the damping acting on the magne-

tization. When the spin current polarization (the associated magnetic moment) is parallel (anti-parallel) to the effective field, it decreases (increases) the effective damping. The field-like torque, on the other hand, renormalizes the effective field (see figure 2.2). While some spintronic devices rely on large field-like torques, the damping-like torque bears the most potential for future spintronics applications. In the devices studied here, the field-like torques are typically rather small, not important for the observed phenomena, and will often be omitted in the discussion.

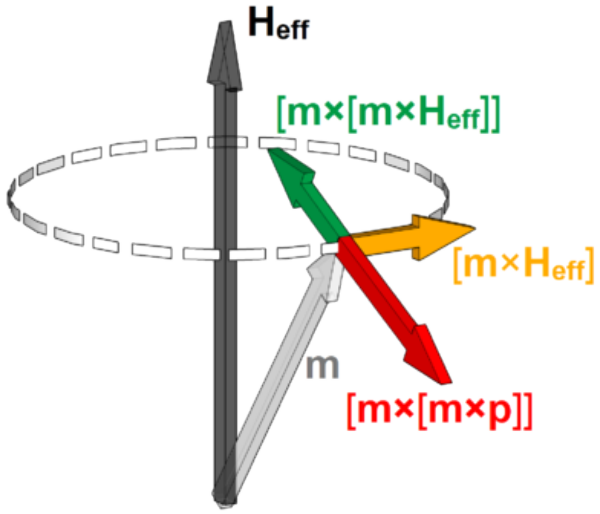

Figure 2.2: Schematic of spin-transfer torque (STT) directions. Adapted from Ref. [17].

As shown in figure 2.3, when electric current flows within ferromagnetic multilayers, the electron flow becomes partially spin-polarized. The consideration of the balance of angular momentum in each layer and the electron flow serves a starting point to derive the torques described above. A necessary consequence is that action (torque) on one of the layers implies a back-action (also a torque) on another layer. Moreover, electron flows in metallic ferromagnets with nonuniform magnetization may lead to spin currents within a single layer and a corresponding action on the magnetization described by the Zhang-Li

torque [19]. While these aspects are not directly applicable to the systems studied in these works, they have to be considered in developing the theoretical framework for the novel phenomena observed.

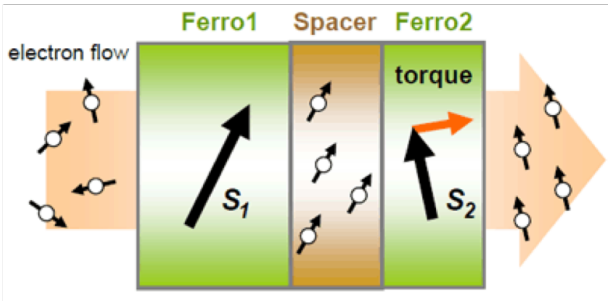

Figure 2.3: Schematic of spin transfer torque in a GMR (Giant Magnetoresistance) spin-valve. The electron flow become partially polarized when passing through ferromagnets. The interaction of the electron flow with the magnetic moment residing in the ferromagnet lead to an interaction of magnetizations of adjacent magnetic layers. Generally, the magnetization is pushed towards the direction of magnetic moments of the injected spin current. Adapted from Ref. [20],

2.1.2 Spin torque oscillators

The spin torque oscillators are magnetic systems that undergo a steady-state oscillation/precession of the order parameter (magnetization) in the absence of a high-frequency external drive [21, 22]. Such oscillation is often referred to as auto-oscillations in analogy with oscillators used in conventional electronics. As indicated in the previous section, the damping-like spin torque can decrease the effective damping (dissipation rate), which presents three possible scenarios for the magnetization precession.

First to stay within the paradigm of spin-polarized electric currents through magnetic multilayers, as shown in figure 2.4, the free layer magnetization, M (red arrow), precesses around the direction of an applied magnetic field (H_0) when magnetic damping torque (blue arrow) is partially compensated by the damping-like spin torque (yellow ar-

row). This presumes the appropriate magnetization orientation of the fixed layer and the direction of the electron flow.

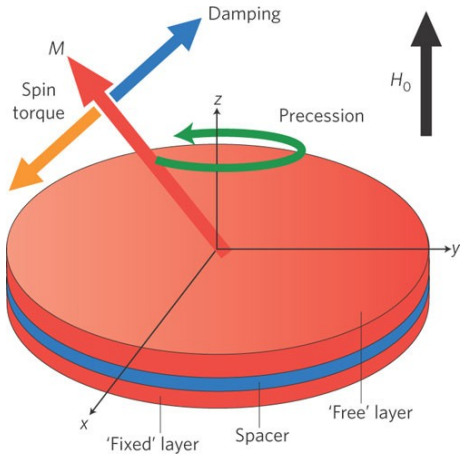

Figure 2.4: Geometry of a spin-torque oscillator consisting of a 'fixed' magnetic layer, a non-magnetic spacer and a 'free' magnetic layer. Adapted from Ref.[6].

The negative damping contribution due to the damping-like torque renormalizes the total effective damping such that three distinct scenarios need to be discussed. As shown in figure 2.5, these scenarios are distinguished by the magnitude of the spin current that is deposited in the magnet. At low currents, the damping is only partially compensated, and the magnetization once tipped away from its equilibrium direction, undergoes a damped precession at the renormalized damping rate. At higher current values, the damping is further reduced and, eventually, fully compensated/negated at the critical current. With zero dampings, the magnetization undergoes a steady-state precession. It is important to mention, that strictly speaking, zero effective dampings would result in a steadily increasing precession angle. However, the presence of nonlinear damping, which is generally inherent to (ferro)magnetic systems – acts as a stabilizing agent and limits the precession cone angle. The frequency of such auto-oscillations is given by the natural frequency of the magnetic

system (typically the lowest-energy spin-wave mode with some nonlinear corrections. In the third scenario, a current pulse of very high magnitude excites, via the damping-like torque, magnetization oscillations that are not sufficiently stabilized by the nonlinear effects and thus result in a full reversal of the magnetization. Once the magnetization passed through the equator onto the lower hemisphere, the damping-like torque changes its sign. Instead of reducing the damping, it increases the damping and thus stabilizes the full reversal of the magnetization.

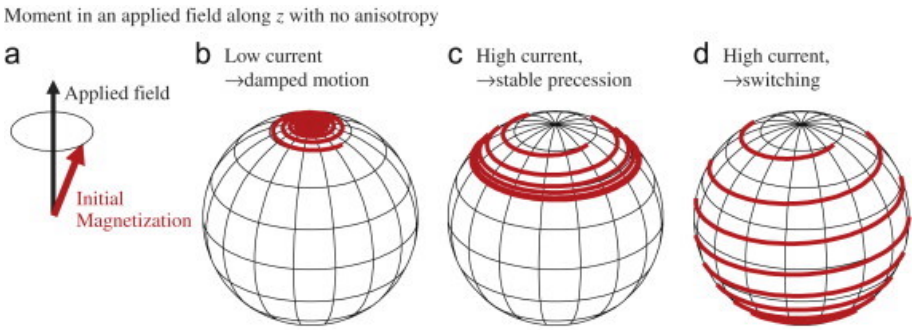

Figure 2.5: (a) Initial magnetic configuration. (b) Trajectory of spin-torque- at low current (damping). (c) Trajectory of spin-torque- at high current (stable precession - auto-oscillation). (d) Trajectory of spin-torque- at high current (switching). Adapted from Ref. [23].

The damping-like torque can be measured through its effect manifesting in one of the three presented scenarios. In this work, two scenarios will be discussed. Via measuring the response of magnetization for an external high-frequency drive at sub-critical spin current values, the damping will be evaluated (see Ferromagnetic Resonance in the next chapter). At and above the critical spin currents, on the other hand, the auto-oscillations can be measured via Emission Spectroscopy (described in the next chapter). The value of the critical values can be extracted in such experiments, and it gives information on the damping-like torque if the intrinsic damping is known. If the intrinsic damping can-

not be precisely evaluated, the critical current value can be mapped as a function of some experiment parameters and give qualitative information on the spin current mechanisms.

2.2 Spin-orbit based spin-charge effects

The magnetic auto-oscillations of a spin torque oscillator can be converted into electrical signals. This requires spin-charge effects – physical phenomena which couple spin and charge degree of freedom. There are generally two types of spin-charge effects allowing for the conversion of spin information into electrical signals: magnetoresistance effects and spin-current to voltage conversion. The effects allowing for spin-to-charge conversion generally have their counter-parts that allow for charge-to-spin conversion and thus offer means for the generation of spin currents. The microscopic mechanisms of these phenomena are based on the spin-orbit interaction. In this section, the relevant aspects of spin-orbit effects leading to magnetoresistance shall be discussed. The magnetoresistances arising in multilayer systems with electrical currents perpendicular to the plane will not play a role in the devices studied here. Instead, the focus shall lie on magnetoresistance arising in systems with electrical currents flowing within the sample plane.

2.2.1 Anomalous Hall effect

In a ferromagnetic conductor, e.g., thin film, the Hall resistance $R_{Hall} = \frac{\rho_{xy}}{d}$ carries an extra contribution, identified as the anomalous Hall effect (AHE) as a result of spin-orbit interaction, which is observed to be directly proportional on the magnetization

of the material [24]:

$$R_{Hall} = R_0\ B + R_s\ M_z \tag{2.4}$$

where B is the applied magnetic field, M_z is the magnetization projection perpendicular to the thin film, and R_0 and R_s are the ordinary and anomalous Hall coefficients respectively. The charge carriers with the majority and minority spin due to spontaneous magnetization M_z becoming opposite "anomalous velocity" due to spin-orbit interaction, which creates unbalanced charge density at the surfaces and causes transverse voltage V_y (see figure 2.6).

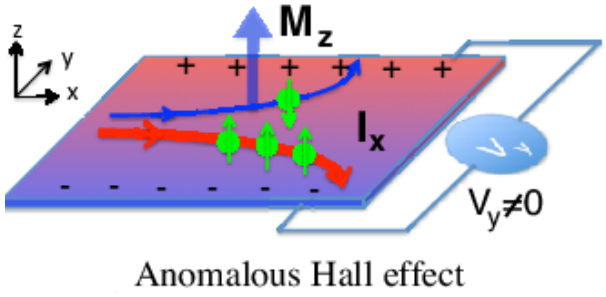

Figure 2.6: Schematic of anomalous Hall effect. Adapted from Ref. [25].

The Anomalous Hall Effect is frequently considered more significant than the ordinary Hall effect. e.g., the anomalous Hall coefficient of nickel is about 100 times larger than the ordinary Hall coefficient near the Curie temperature [26]. Although it is a long-known phenomenon, there still are debates concerning the microscopic mechanisms of AHE in the many materials. Extrinsic mechanisms can cause the anomalous Hall effect due to spin-dependent scattering (skew scattering from disorder) of the charge carriers. Alternatively, AHE can be caused by an intrinsic mechanism due to the Berry phase accumulation in the electron bandstructure – which establishes a connection between the AHE and the topology of the bandstructure [27, 28].

2.2.2 Anisotropic magnetoresistance

William Thomson discovered anisotropic magnetoresistance (AMR) in ferromagnetic metals in 1857 [29]. This property determines the dependence of electrical resistance on the angle between the orientation of magnetization and the direction of electric current in the material. AMR effect originates from the spin-orbit interaction and involves further effects like the $s-d$ scattering of electrons. Generally, the longitudinal resistance is lowest (highest) for the electric current direction perpendicular (parallel) to the magnetization in the case of positive AMR and vice versa in the case of the negative AMR.

In ferromagnetic metals, the AMR can be described as function of the angle $\varphi = \psi - \theta$ between the orientation of magnetization and the electrical current direction as:

$$\rho_{xx}(\varphi) = \rho_{\perp} + (\rho_{\parallel} - \rho_{\perp}) \cos^2 \varphi \tag{2.5}$$

where the variation of the longitudinal resistivity ρ_{xx} is called the anisotropic magnetoresistance (AMR) as a function of the angle φ. The $\rho_{\parallel}$, $\rho_{\perp}$ are the resistivities for $\varphi = 0°$ and $90°$ with respect to the current, respectively. The longitudinal resistivity of the AMR ρ_{xx} has a counterpart of an additional transverse resistivity ρ_{xy} that is referred to as the planar Hall effect (PHE), described in the next section. The AMR ratio is represented by [30]:

$$\frac{\Delta\rho}{\rho} = \frac{\rho_{\parallel} - \rho_{\perp}}{\rho_{\perp}} = \frac{R_{\parallel} - R_{\perp}}{R_{\perp}} = \frac{\Delta R}{R_0} \tag{2.6}$$

As shown in figure 2.7 (adapted from Ref. [31]), the magnetoresistance is typically estimated in magnetotransport measurements, where the resistance is measured as a function

of the external magnetic field applied along some symmetry axes of the magnetic system, or as a function of magnetic field angle, providing that for any angle the value of the magnetic field is sufficient to saturate the sample magnetically. The resistance can be estimated utilizing the pseudo-four-point probes method [31], as shown in figure 2.7; however, resistance offsets due to contact resistances in the two-point method would typically not affect the magnetoresistance value, but only the AMR ratio.

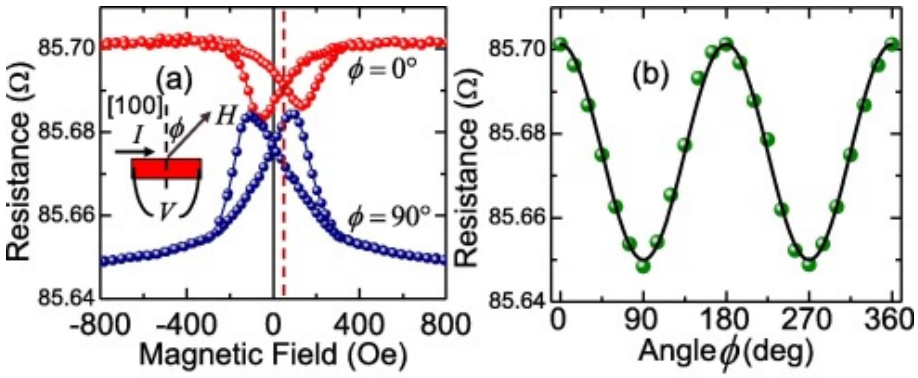

Figure 2.7: (a) The AMR resistance when it's parallel ($\varphi = 0°$) and perpendicular ($\varphi = 90°$). (b) Angular variation of the resistance with magnetic field $H = 800$ Oe. Adapted from Ref. [31].

2.2.3 Planar Hall effect

The planar Hall effect (PHE) is closely related to the anisotropic magnetoresistance (AMR). The transverse resistivity ρ_{xy} of PHE depends on the angle between the magnetization orientation in the ferromagnetic conductor and the direction of the electrical current that passes within the material and is described via

$$\rho_{xy}(\varphi) = \frac{1}{2}\left(\rho_{\parallel} - \rho_{\perp}\right)\sin 2\varphi \tag{2.7}$$

where the variation of ρ_{xy} is called the planar Hall resistance. Figure 2.8a presents the design of a typical device pattern employed for measuring the variation of ρ_{xx} (AMR) and ρ_{xy} (PHE). Figure 2.8b shows the relationship of the longitudinal and transverse resistance with the angle φ between the current I and the magnetization M demonstrating AMR (in blue) and PHE (in red), respectively.

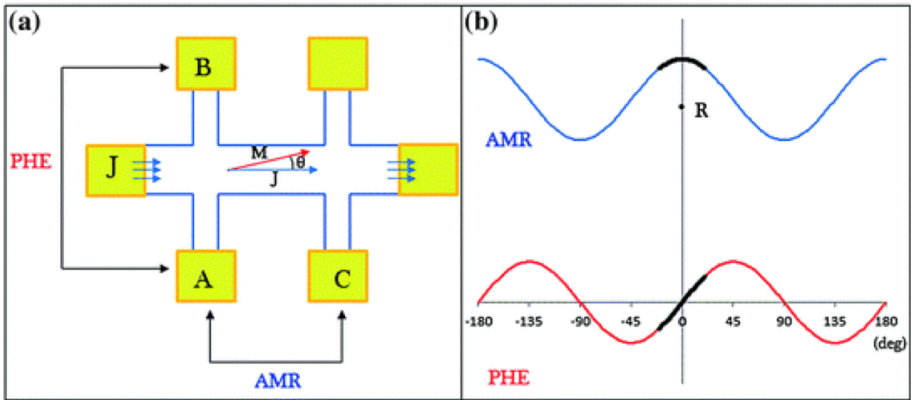

Figure 2.8: (a) The typical way to measure AMR and PHE. (b) The dependence of the longitudinal and transverse resistance on the angle φ. Adapted from Ref. [32].

2.3 Pure spin currents

The magnetoresistance phenomena described above have only recently been shown to be related to spin-orbit spin current and spin torques originating from the same mechanisms. Before introducing the AHE, AMR/PHE spin currents, though, it is more conducive first to introduce the spin Hall effect (SHE) and the related phenomenon of the spin Hall magnetoresistance. The AHE, AMR/PHE spin currents can then be simpler explained by analogy.

Generally, electric currents within the plane of the multilayer can lead to a plethora of spin-orbit related effects, resulting in magnetoresistance and spin torque. Resorting to the

significant phenomena, a multilayer consisting of a ferromagnetic layer (can be insulator) and non-magnetic metal will first be considered. The Spin-orbit torque (SOT) occurs due to the spin accumulation at the ferromagnetic and non-magnetic conductor (FM/NM) interface [33]. The two principal spin-orbit interaction phenomena that are associated with generating the spin accumulation are spin Hall effect (SHE) and interfacial Rashba effect (see figure 2.9).

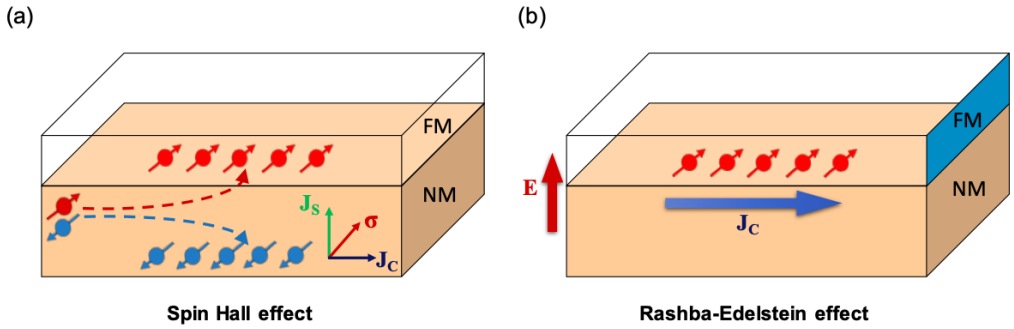

Figure 2.9: (a) Schematic of the bulk spin Hall effect in a NM. (b) Schematic of Rashba effect at the FM/NM interface. Adapted from Ref. [34].

The role of the interfacial Rashba effect has recently been controversy debated. In most cases here, where the exact origin and mechanism of the SHE/Rashba spin current is irrelevant, both spin currents will be viewed as one effective SHE-like spin current and for simplicity referred to as SHE. The spin currents discussed in what follows can be referred to as pure spin currents, i.e., spin currents without the associated charge transport in the direction of the spin flow.

2.3.1 Spin Hall effect

The SHE is a transport phenomenon that utilizes the spin-orbit interaction in the NM to transform the charge current into a pure spin current and vise versa. The origin lies either in the band structure (intrinsic) and the addition of spin-orbit interaction impurities (extrinsic). It leads to an effective spin-dependent asymmetric scattering of the conduction electrons, which in turn leads to an effective spin-dependent asymmetric scattering of the conduction electrons to spins of opposite sign accumulating at the surfaces of the NM. When the NM is adjacent to an FM, the spin accumulation creates a transverse spin current when the unpolarized charge current flows in the NM [34, 35, 36]. There is no requirement for the magnetic field to generate SHE, and instead, the transverse resistivity, it is the transverse flow of spin current that is generated by the SHE. The injected charge current $\vec{J_c}$ can produce spin current $\vec{J_s}$ due to SHE, which is described by:

$$\vec{J_s} = \frac{\hbar}{2e}\,\theta_{SH}\,(\vec{J_c}\,\times\widehat{\sigma}) \tag{2.8}$$

where θ_{SH} is the spin Hall angle of the NM, which represents the spin current generation efficiency.

The magnitude of θ_{SH} defines the size of the spin current density an NM can generate for a given charge current density, and the sign of θ_{SH} establishes the direction of the spin polarization at the NM/FM interface.

In a simple phenomenological picture, the spin current generated by the SHE can be seen as partially reflected from the NM/FM interface. The reflection depends on the spin current susceptibility of the FM spin system and thus depends on the angle between the

magnetization and the spin polarization of the spin accumulation at the NM/FM interface. The spin current reflected into the NM is converted into an electrical signal (voltage) via the inverse spin Hall effect. This results in a variation of the effective longitudinal resistance of the NM. The variation of the longitudinal resistance is a function of the magnetization direction and thus a magnetoresistance effect. It is referred to as spin Hall magnetoresistance and is described by [37]:

$$\rho = \rho_0 + \Delta\rho \, [1 - \cos^2(\frac{\vec{M} \cdot \hat{\sigma}}{M})] \tag{2.9}$$

where $\Delta\rho$ is the effective spin Hall magnetoresistance value.

2.3.2 Spin Seebeck effect (SSE)

Thermal gradients can generate pure spin currents. Here, the case shall explicitly not be discussed in which a thermal gradient causes a charge flow. Such charge flow can itself be spin-polarized and thus result in the spin current. Instead, a pure spin current shall be considered. At an FM/NM interface, the magnons in the FM can be coupled to the electrons in the NM and result in the transfer of angular momentum (spin current) between these subsystems. The spin current is nonzero if the magnon and the electron subsystems are not in thermal equilibrium. For example, this can be achieved by applying a thermal gradient across the FM/NM interface.

Considering the case of the FM temperature and thus the magnons' temperature higher than the NM and its electrons, the following scenario occurs. The magnons are annihilated at the FM/NM interface, and their angular momentum is transferred to the spins of the NM's conduction electrons. This spin-transfer established a spin current $\vec{J}_s$.

The current is converted into a voltage by the inverse spin Hall effect in the NM [38]:

$$\vec{E}_{ISHE} = \frac{\theta_{SH}\,\rho}{A}\,(\frac{2e}{\hbar})\,\vec{J}_s \times \vec{\hat{\sigma}} \tag{2.10}$$

where θ_{SH} is the spin Hall angle of the NM metallic layer, ρ its electric resistivity, and A is the contact area between the ferromagnetic layer and the NM layer.

If the temperature gradient direction at the FM/NM interface is reversed, the magnons at the interface are not annihilated but instead created. The polarization of the interfacial spin current thus changes the sign. The voltage induced due to the inverse SHE changes the sign as well.

2.3.3 Longitudinal spin Seebeck effect

The longitudinal configuration of the SSE, i.e., when the spin current flow in the same direction as the thermal gradient is considered, can be used to probe the magnetization of the FM, which makes the SSE adequately a spin-to-charge conversion effect – similar to a magnetoresistive phenomenon. The typical experimental setup is sketched in figure 2.10).

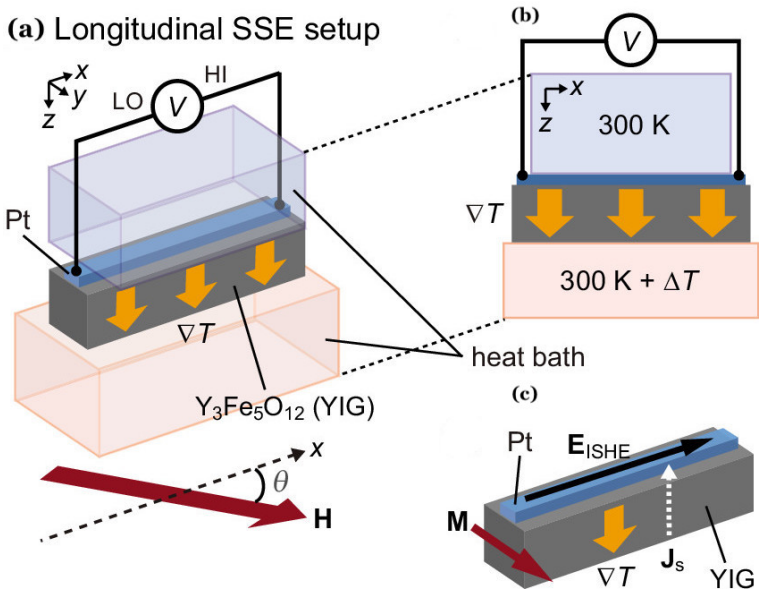

Figure 2.10: (a) and (b) A schematic of the longitudinal SSE in an YIG/Pt sample. (c) The simple design of the longitudinal SEE setup. Adapted from Ref. [39].

The interfacial spin current detected in the NM via inverse SHE also affects the magnetization of the FM layer. The thermal pure spin current, which corresponds to the annihilation of magnons, creates an effective anti-damping spin torque. The spin current, which corresponds to the creation of the magnon, exerts an anti-damping spin-torque effectively. The created magnons redistribute across the magnonic band and thus increase magnons' effective lifetime. The processes leading to a redistribution of magnons due to the SSE spin current injection are not fully understood, but have been in major parts formulated theoretically and observed experimentally. In the following section, pure spin currents and their effect on the magnetization shall be discussed.

2.3.4 Spin-orbit and thermal pure spin currents

Today, the prevalent approach to generate pure spin currents is the spin Hall effect (SHE) [35, 36, 40, 41]. Charges are moving in a nonmagnetic (NM) metal experience spin-dependent scattering due to spin-orbit interaction via extrinsic scattering processes or intrinsically via Berry curvature of the electronic band structure [42]. The spin Hall effect results in a transverse pure spin current, achieved in a variety of metals [42, 43]. Magnetic switching via SHE has been realized in FM/NM bilayer systems and three-terminal magnetic tunnel junctions [44]. Magnetic auto-oscillations driven by SHE has been shown in metallic [45, 46] and insulating ferromagnets [47]. The SHE, however, presents a major constraint [42, 48, 49] illustrated in Figure 2.11, the polarization $\vec{\sigma}$ of the spin current is always perpendicular to the direction of the electrical current $\vec{I}_e$ and spin current $\vec{I}_s$:

$$\vec{\sigma} \sim \vec{I}_e \times \vec{I}_s \tag{2.11}$$

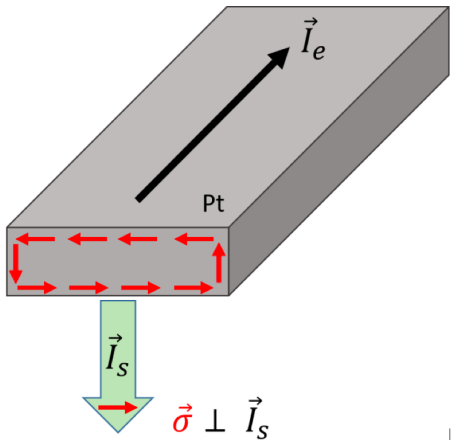

Figure 2.11: Pure spin current emitted from a Platinum layer via spin Hall effect is polarized perpendicular to the directions of electrical and spin currents.

This fixed spin current polarization presents a significant limitation to the performance of spintronic applications [50]. For instance, it has been long established that magnetic switching is more energy-efficient in systems with perpendicular-to-plane (PTP) [1, 10] magnetization $\vec{M}$. The Slonczewski term describes the damping-like spin torque [8, 18, 23, 51, 52, 53] exerted on the magnetization:

$$\frac{\partial \vec{M}}{\partial t} \propto \vec{I}_s \left(\vec{M}(t) \times \vec{M}(t) \times \vec{\sigma}\right) \tag{2.12}$$

For the collinear orientation of the equilibrium magnetization and spin current polarization, this term has the same symmetry as magnetic damping. Such anti-damping torque is sufficient for magnetization switching [18, 23, 50, 51, 52, 53]. In the case of the PTP devices, however, the spin current polarization and magnetization direction are perpendiculars, and the anti-damping torque is thus zero. Perpendicular configurations are also favorable for magnonic waveguides and auto-oscillators because of the higher frequencies of operation and significant suppression of detrimental nonlinear magnon scattering [45] limiting device performance. The fixed polarization of the SHE spin currents limits their implementation in existing device paradigms and impedes the development of novel device applications. For example, the emerging concept of spin superfluids [54, 55, 56] requires the injection of perpendicular-to-plane pure spin currents into an easy-plane magnetic structure that is not available today.

Recently, Tanaguchi et al. [57] have theoretically established that spin currents with tunable spin polarization can be created using anomalous Hall effect (AHE) and planar Hall effect (PHE) [58, 59, 60]. Experimental confirmation of the feasibility of such currents

has been provided by magnetoresistive measurements, second harmonic magneto-optical measurements [61, 62], and evaluation of rectified voltage [63, 64]. Generally, the spin currents originating from AHE and PHE can be viewed as follows.

The anomalous Hall effect is observed in ferromagnetic metals. Similar to the spin Hall effect in non-magnetic metals, the AHE [28] originates from the spin-orbit interaction. In contrast to the SHE, however, the AHE can generate spin currents with the polarization that is determined by the magnetization orientation [57]. With an electric field, $\vec{E}$ applied to the ferromagnet, the majority, and minority electrons are affected by different potentials due to the spin-orbit interaction, which gives rise to spin current as well as charge current in the direction $\vec{M} \times \vec{E}$ with the polarization $\vec{M}$. The spin current tensor assumes the form:

$$Q^{AHE} = \frac{-\hbar}{2eM^2} \, \zeta \, \vec{\sigma}_{AHE} \, (\vec{M} \otimes \vec{M} \times \vec{E}) \tag{2.13}$$

where $\vec{\sigma}_{AHE}$ is the anomalous Hall conductivity, and ζ is the associated polarization factor (different from spin polarization for conventional spin-polarized electrical currents).

The planar Hall effect [60] is a part of the anisotropic magnetoresistance phenomenon, which is also a consequence of the spin-orbit interaction. Besides the resistivity variations, the polarization of the charge current varies too. As a result, there is spin and charge current in the $\vec{M}\,(\vec{M} \cdot \vec{E})$ direction with the polarization $\vec{M}$. The spin current tensor assumes the form:

$$Q^{AMR} = \frac{-\hbar}{2eM^3} \, \eta \, \vec{\sigma}_{AHE} \, (\vec{M} \otimes \vec{M}(\vec{M} \cdot \vec{E})) \tag{2.14}$$

where $\vec{\sigma}_{AMR}$ describes the AMR conductivity and η is the associated polarization factor

[57].

The AHE/PHE spin currents are suitable for the generation of pure spin currents from a ferromagnetic injector, with the polarization determined by its magnetization vector. That allows proposing a simple device architecture consisting of two ferromagnetic layers, with one layer acting as a spin injector (FM2 in figure 2.12) and another as spin acceptor (FM1 in figure 2.12). Customization of the spin torque necessary to switch the FM1 magnetization or to drive magnetic auto-oscillations can be done by optimizing AHE/PHE spin-charge transducer efficiency and by engineering the appropriate magnetization orientation of the spin injector FM2.

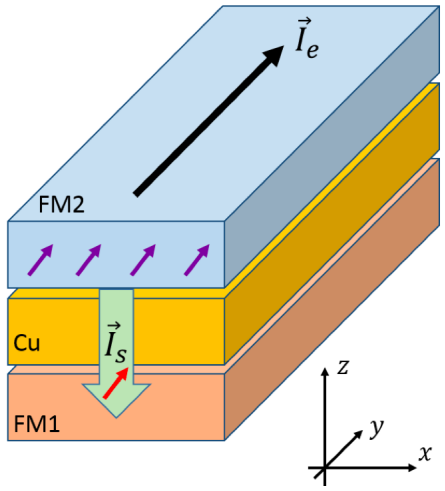

Figure 2.12: A ferromagnetic layer FM2 acts as an injector of pure spin current with polarization collinear with its magnetization. The spin current is injected into another ferromagnetic layer FM1 through an (optional) nonmagnetic layer.

Spin-charge transducers, such as AHE/PHE spin injectors, will inevitably generate Ohmic heating – a common problem to all electronic applications [1]. In AHE/PHE devices, Ohmic heating would create a temperature gradient across the layers. A temperature gradient in two-ferromagnet systems has been theoretically predicted to generate spin Seebeck

spin-torque [65]. Therefore, this effect must be taken into account in all studies of magnetization dynamics in multilayer systems. This complication, however, bears a tremendous potential for spintronics considering the SSE itself is a highly efficient means for creating tunable spin currents [49, 66].

Spin-charge transducers, such as AHE/PHE spin injectors, will inevitably generate Ohmic heating – a common problem to all electronic applications [1]. In AHE/PHE devices, Ohmic heating would create a temperature gradient across the layers. A temperature gradient in two-ferromagnet systems has been theoretically predicted to generate spin Seebeck spin-torque [65]. Consequently, this effect requirement is taken into account in all studies of magnetization dynamics in multilayer systems. This complication, however, bears a tremendous potential for spintronics considering the SSE itself is a highly efficient means for creating tunable spin currents [49, 66].

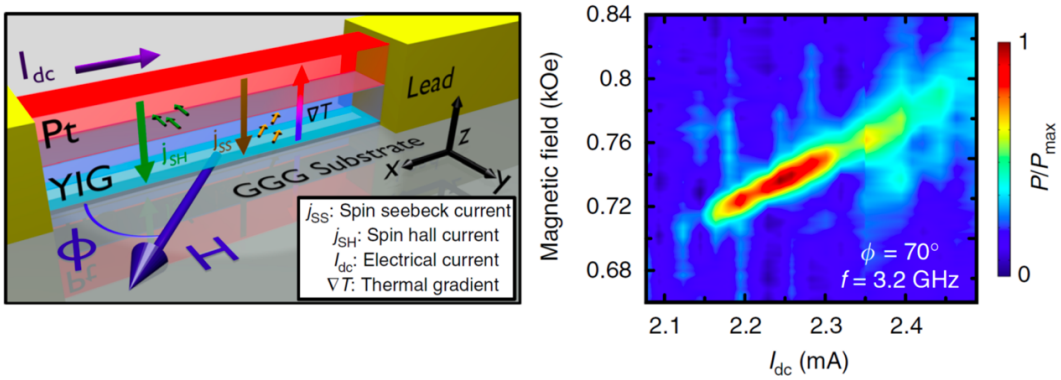

Figure 2.13: (left) Schematic view of a magnetic insulator (YIG)/Pt spin-torque nano-oscillator device. Arrows indicate magnetic field direction, bias current, temperature gradient, and spin currents, including their respective polarizations. (right) Microwave emission signal from the nanodevice due to auto-oscillations of magnetization. The results from Ref.[66].

Recent theoretical works by Tserkovnyak et al. [65] and by Wang et al. [67] show

that in two-ferromagnet systems subject to a temperature gradient, large spin Seebeck torques can be achieved. As shown in figure 2.14a, a pure spin current of magnons flows between (insulating) ferromagnetic layers and causes a spin accumulation in the spacer layer. The spin accumulation constitutes a spin current that can exert an anti-damping spin torque on the free layer. The change in damping is:

$$\Delta\alpha_{SEE} = -\eta_{SEE}\,\frac{\delta T}{\hbar\Omega} \tag{2.15}$$

where η_{SEE} is a parameter defined by interfacial magnon conductivities and spin Seebeck coefficients, and $\hbar\Omega$ is a magnonic bandgap. The anti-damping spin-torque results in auto-oscillation of magnetization when $\Delta\alpha_{SEE}$ overcomes the intrinsic damping of the free layer (plus spin losses [68]). Figure 2.14b shows a phase diagram for two ferromagnetic layers with easy-axis magnetic anisotropy. It reveals that the thermal current drives the free layer into the auto-oscillatory state and establishes a spin torque oscillator (STO, Figure 2.14(c)). The SSE in two-ferromagnet systems has been theoretically predicted to create large spin torques, but it has not yet been experimentally realized. The results, introduced in this dissertation, demonstrate that the SSE driven reduction of damping can be achieved in two-ferromagnet systems and sufficiently large to drive magnetic auto-oscillations. Therefore, the SSE may be considered a potentially efficient means for generating tailored spin currents, even in two-magnet systems.

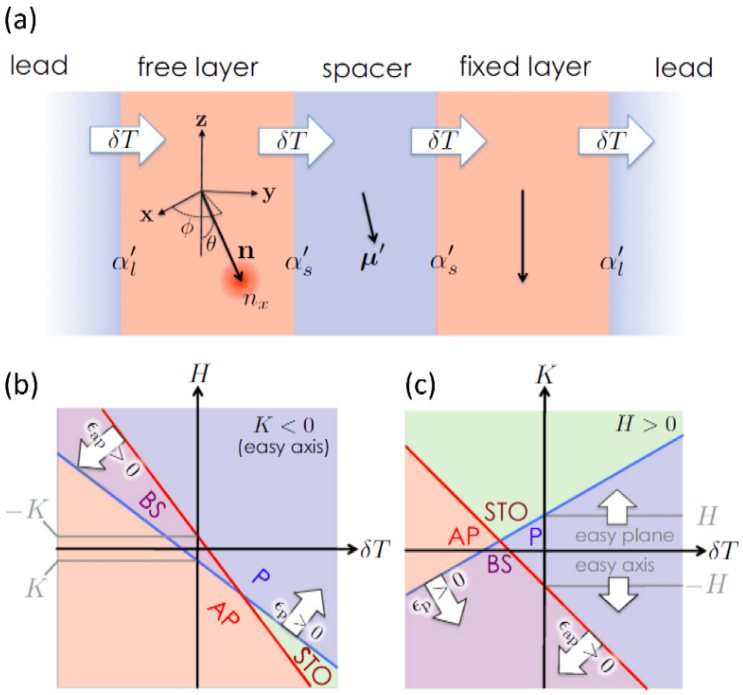

Figure 2.14: (a) Concept of a SSE device with two ferromagnetic layers. (b) Field–temperature gradient phase diagram for easy-axis magnets revealing: BS bi-stable, P parallel, AP anti-parallel states, and STO spin torque oscillator. (c) Magnetic anisotropy–temperature gradient phase diagram. Source: Ref. [65].

Chapter 3

Development of Experimental Methods

In this chapter, experimental methods will be presented that were used in the course of the Ph.D. work. Some of the experimental techniques already existed when the work began (see figure 3.1). However, many experimental techniques and data processing methods were developed or advanced in the course of the work.

Figure 3.1: Working at the FMR spectrometer in the early stages of the Barsukov lab.

3.1 Microwave spectroscopy

3.1.1 Broadband Ferromagnetic Resonance spectroscopy

Ferromagnetic resonance (FMR) spectroscopy is a powerful technique for examining the static and dynamic magnetic properties of ferromagnetic systems and investigating the fundamental physics aspects of spin excitations. In 1935 Lev Landau and Evgeny Lifshitz predicted the ferromagnetic resonance as a Larmor precession of the magnetic moments in ferromagnetic materials [69], which was then independently confirmed in experiments by Zavoisky and Griffiths [70, 71].

Traditionally, ferromagnetic resonance is measured by applying a quasi-static magnetic field to the sample and additionally subjecting it to a high-frequency field in the GHz frequency range. The direction of the high-frequency magnetic field is perpendicular to the static field. The FMR setup is shown in figure 3.2. It involves a Coplanar Waveguide (CPW), an electromagnet (GMW Dipole Electromagnets, 76mm, 5403 (see figure 3.3)),

field modulation coils, microwave signal generator (E8257D PSG Analog Signal Generator (see figure 3.4)), and other elements.

The CPW used in this work were developed based on previous designs to provide a broad-frequency coverage up to 45 GHz with minimal nearly linear transmission coefficient. An RF detector (703BK DETECTOR 100 MHz-40 GHz (see figure 3.5)) is located at the end of the CPW to detect the microwave signal passing through the coplanar waveguide. The signal is sent to the lock-in amplifier (7265 Dual-Phase DSP Lock-in Amplifier (see figure 3.6)) for demodulation at the frequency of an additional low-frequency magnetic field supplied by the modulation coils in the direction parallel to the static field.

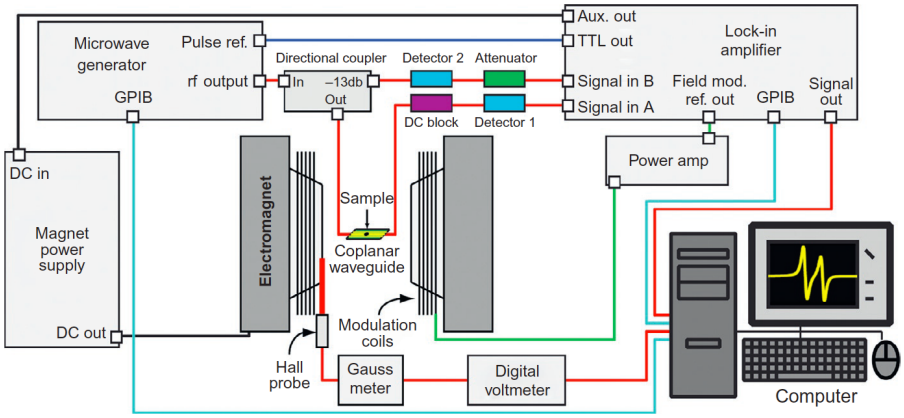

Figure 3.2: Schematic of the FMR spectrometer for a coplanar waveguide (CPW) with field modulation. Adapted from Ref. [72]. In the course of the work, the setup was further advanced to increase the data acquisition rate using an external digital-analog-converter (DAQ).

Figure 3.3: GMW Dipole Electromagnet, 76mm, 5403 with water cooling.

Figure 3.4: E8257D PSG Analog Signal Generator.

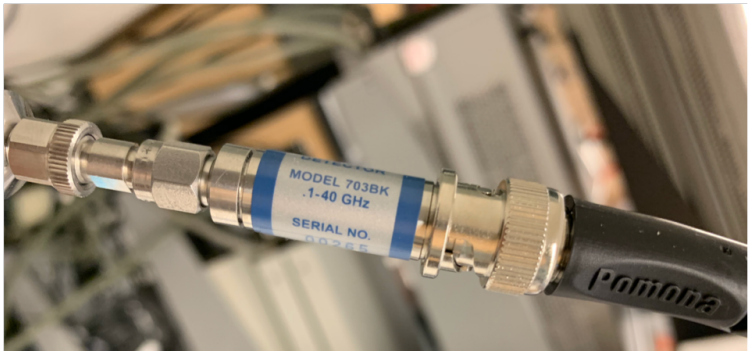

Figure 3.5: 703BK DETECTOR 100 MHz-40 GHz.

Figure 3.6: 7265 Dual Phase DSP Lock-in Amplifier.

The sample (e.g., ferromagnetic thin film) is placed onto the CPW transmission line (flip-chip or facedown: the top surface of the film is directly touching the transmission line). The CPW with the sample is placed between the electromagnet poles in the area of the highest field uniformity. When the magnetic field is swept (field-domain), the magnetization absorbs microwave power in resonance and reduces the microwave transmission through the CPW.

The resonance frequency of a ferromagnetic thin film with external magnetic field $\vec{H}$ applied within the film plane is well approximated by the Kittel formula (for in-plane orientation) [73]:

$$f = \frac{\gamma}{2\pi}\sqrt{(H + H_a)(H + H_b + 4\pi M_{eff})} \tag{3.1}$$

where H_a and H_b are effective anisotropy fields (or reduced stiffness field, typically these

are due to magnetocrystalline anisotropy and very small), M is the magnetization of the sample, and γ is the gyromagnetic ratio [74]. $4\pi M_{eff}$ is the magnetization of the sample representing the shape anisotropy, augmented, or reduced by any other first-order uniaxial magnetic anisotropy with perpendicular-to-plane symmetry axis.

Figure 3.7 shows the typical frequency-field relation for a standard YIG thin film with a thickness of 20 nm. The experimental data is fitted well by the Kittel formula for in-plane configuration. The extracted parameters such as g-factor, the effective magnetization $4\pi M_{eff}$, and the anisotropy field $H_b \approx H_a$ agree resonably well the literature values for YIG thin films.

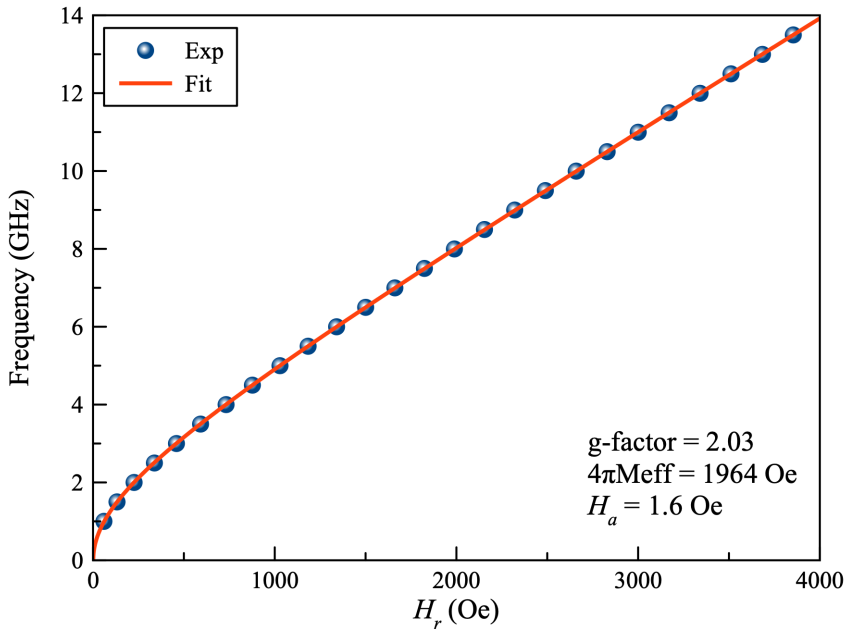

Figure 3.7: The resonant frequency versus the magnetic field of a YIG thin film.

With magnetic field applied perpendicular to the film plane, the frequency-field

relation changes such that it can be described by the out-of-plane Kittel formula:

$$f = \frac{\gamma}{2\pi}(H + H_b - 4\pi M_{eff}) \tag{3.2}$$

In magnetic films with positive $4\pi M_{eff}$, a frequent limitation to the FMR experiment is the magnetic field. In films with negative $4\pi M_{eff}$, the limiting factor is often the frequency range. Moreover, FMR measurements in out-of-plane geometry typically require an exact alignment of the film's normal vector to be parallel with the external field and may necessitate the usage of a goniometer.

Field-domain FMR spectra

The FMR experiment can be carried out while sweeping either the field or the frequency. The more common approach is to use the field sweep while the microwave frequency is kept constant. The field-domain spectra obtained in such experiments are more simple to evaluate and process.

The spectra are field-derivatives of the original response of the magnetic system due to the field modulation and lock-in technique. A sum of field derivatives of the symmetric and anti-symmetric Lorentzian functions is used to analyze the FMR spectra. In inductive FMR (such as CPW measurements used here), the anti-symmetric Lorentzian function must be taken into account due to non-uniformities of the high-frequency magnetic field. Moreover, the presence of several overlapping signals may require a fitting procedure with multiple pairs of symmetric and anti-symmetric functions. It should also be noted that the field derivative of a symmetric Lorentzian is an anti-symmetric function, which may be

confusing when discussing the FMR data (see C.1).

The field-sweep FMR technique measures dV/dH as a function of H, and it can be described by the following equation (see C.1 and ref. [75]):

$$\begin{aligned}\frac{\mathrm{d}V}{\mathrm{d}H} = & \frac{2\,Va}{[(1+4\,(\frac{H_{ext}-H_r}{2\,\Delta H})^2)\,(2\,\Delta H)]} \\ & -\frac{8\,Vs\,(H_{ext}-H_r)}{[[(1+4\,(\frac{H_{ext}-H_r}{2\,\Delta H})^2)]^2\,(2\,\Delta H)^2]} \\ & -\frac{16\,Va\,(H_{ext}-H_r)^2}{[[(1+4\,(\frac{H_{ext}-H_r}{2\,\Delta H})^2)]^2\,(2\,\Delta H)^3]}\end{aligned} \tag{3.3}$$

where V_s and V_a are the symmetric and anti-symmetric Lorentzian amplitudes, H_{ext} the external magnetic field, H_r the resonant field of a ferromagnetic sample, and ΔH is the half-width at half maximum (HWHM). It must be regarded that both symmetric and anti-symmetric Lorentzians, must be fitted with the same resonance field and linewidth.

Figure 3.8 shows that the FMR signal, which is the first derivative of the voltage signal with respect to the magnetic field for standard YIG thin film with a thickness of 20 nm. The measurement is done at a fixed frequency of about 6.0 GHz with sweeping the magnetic field. The FMR signal is fitted to the Eq. 3.3 [75] (see C.1) to obtain the resonance field H_r and the linewidth ΔH.

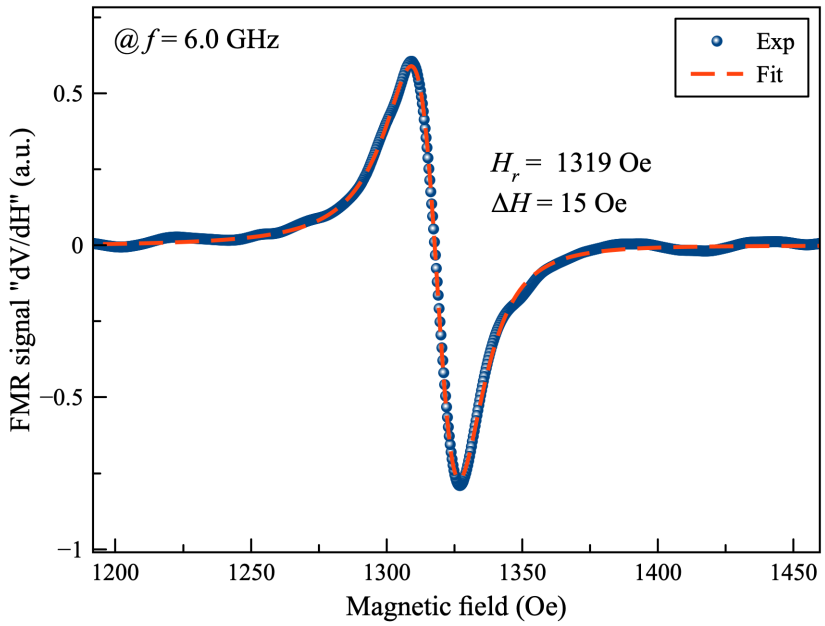

Figure 3.8: The FMR signal at 6.0 GHz of YIG thin film.

FMR Linewidth

The FMR linewidth is, in the most simple case, linearly dependent on the microwave frequency. Adopting the half-width at half-maximum (HWHM) of absorbed microwave power [76] can be related to the Gilbert damping constant α via:

$$\Delta H(f) = \Delta H_0 + \alpha \frac{2\,\pi f}{\gamma} \tag{3.4}$$

where ΔH_0 defines the inhomogeneous broadening, which overlaps the responses of various areas of the sample, in a sample with negligible inhomogeneity, this value approaches zero.

Figure 3.9 shows that the linewidth ΔH as a function of the resonant frequency of a YIG thin film with a thickness of 30 nm. The YIG film has a small value of the inho-

mogeneous broadening ΔH_0= 1.97 Oe, which indicates a good quality (low inhomogeneity over macroscopic length scales) of the film.

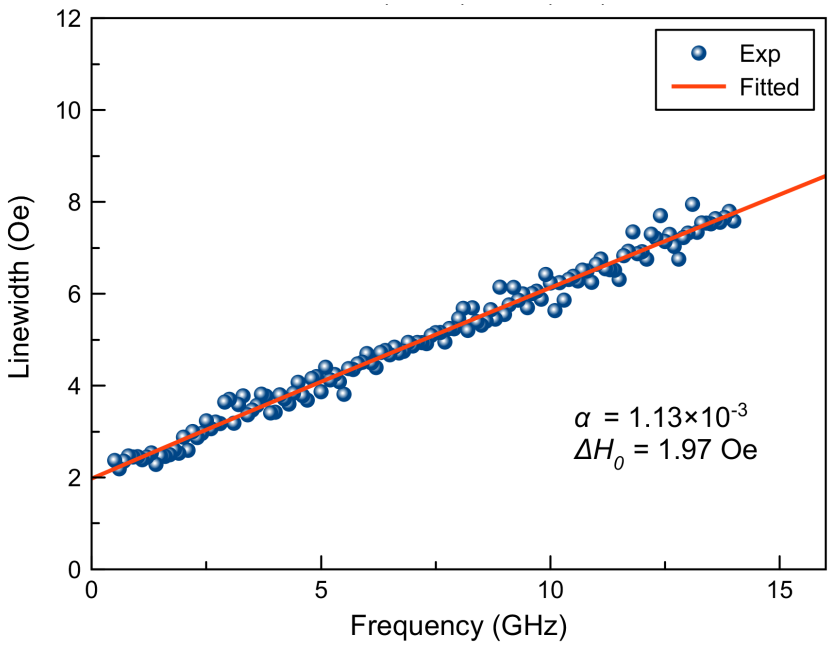

Figure 3.9: The linewidth at 6.0 GHz of YIG thin film.

Two-Magnon Scattering

Even in the case of negligible inhomogeneity, the FMR linewidth does not necessarily represent the Gilbert damping. Although an effective magnetic damping α_{eff} is often introduced, it is meant to represent both the Gilbert damping and any additional dissipation channels inherent to the magnetic system studied. The linear frequency dependence of the Gilbert damping may be adequate for many magnon-phonons, magnon-electron, some magnon-magnon processes, and radiative damping. However, in this film, another dissipation mechanism of two-magnon scattering mus be taken into account.

Sparks et al. [77] introduced the theory of two-magnon scattering to solve the FMR

linewidth broadening in the magnetic insulator (YIG). A magnon of the uniform spin-wave mode transmutes into a magnon of nonuniform mode with the same energy in a two-magnon scattering process. The processes require the presence of such degenerate magnon states within the magnon band. Moreover, this process violates the conservation of translational momentum and is thus only possible in the presence of defects within the sample. The two-magnon scattering mediating defects (at the surface or in the volume of the film) is often found in the samples with increased inhomogeneity. However, this correlation is not necessarily causal and thus not universal.

When the magnetization is tilted out of the film plane by more than $\sim$45 deg, no degenerate nonuniform magnon states exist, and the two-magnon scattering is inoperative [78, 79]. For the in-plane configuration, when the magnetization typically lies within the sample plane, the two-magnon scattering can regularly be found. To study the two-magnon scattering, most typically, the FMR linewidth has to be examined as a function of frequency. However, studies on the anisotropy of the linewidth regarding the angle between the magnetization $M(H)$ and the sample plane can provide more detailed information.

The two magnon scattering contributes to the FMR linewidth via the following term [80]:

$$\Delta H_{2M} = \Gamma \ \sin^{-1} \sqrt{\frac{\sqrt{2\pi f + (\frac{\gamma\, 4\pi M_{eff}}{2})^2} - \frac{\gamma\, 4\pi M_{eff}}{2}}{\sqrt{2\pi f + (\frac{\gamma\, 4\pi M_{eff}}{2})^2} + \frac{\gamma\, 4\pi M_{eff}}{2}}} \tag{3.5}$$

where the prefactor Γ is the anisotropic two-magnon scattering magnitude. The frequency dependence of the two-magnon scattering is nonlinear, distinguishing it from the linear Gilbert damping possible.

Figure 3.10 shows that the linewidth ΔH as a function of the resonance frequency

for YIG (20nm)/Pt (5nm) thin film. The linewidth shows an inhomogeneous broadening, indicating increased structural inhomogeneity or defects. The Eq. (3.4) describes the inhomogeneous broadening ΔH_0 is the horizontal (dashed black line), the Gilbert linewidth ΔH_0, moreover, revel a linear increment of the linewidth (solid red line), the two-magnon linewidth ΔH_{2M} is characterized by Eq. (3.5) (solid green line), and the dashed red line is the sum of all contributions. The prefactor $\Gamma = 7.46$ Oe is relatively high, suggesting the presence of defects within the sample.

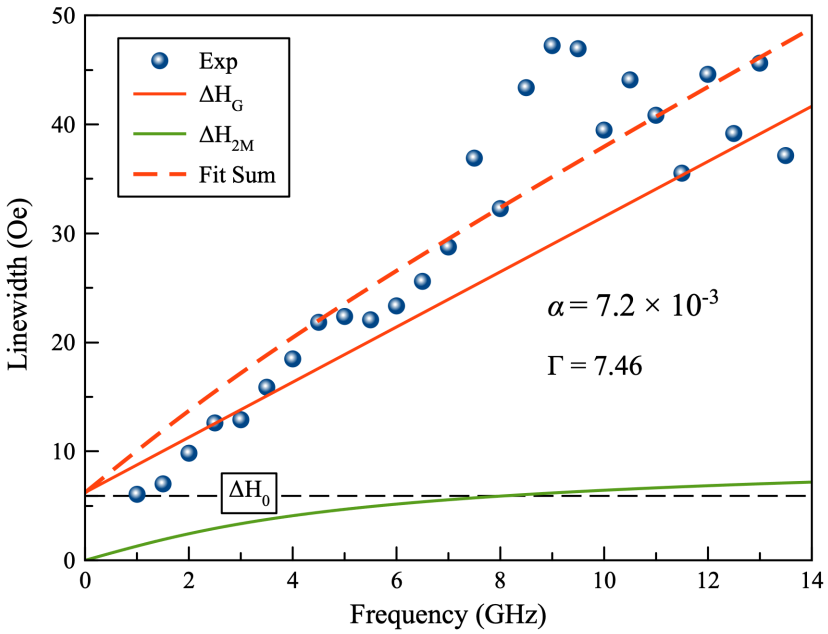

Figure 3.10: Schematic diagram of the frequency dependence of the various linewidth contributions.

Coplanar Waveguide (CPW) Design

The coplanar waveguides (CPW) used in this work have been designed based on the concept shown in figure 3.11.

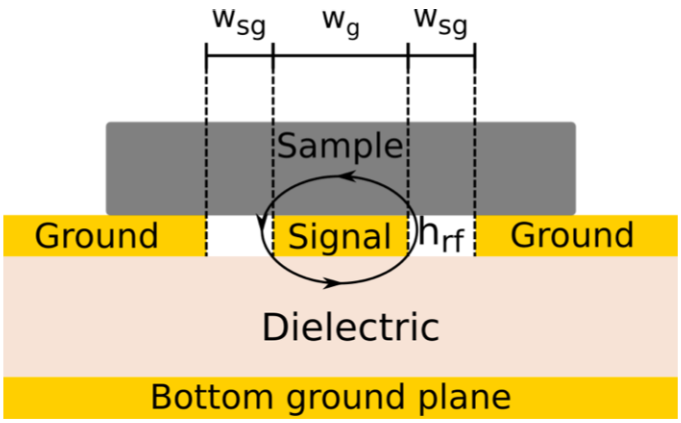

Figure 3.11: Illustration of a coplanar wave guide with a sample placed over the central line. Adapted from Ref. [81].

It consists of the bottom ground plate and the top central line that is accompanied by two top ground plates. Line arrays of conductive vias are placed along the signal line, to connect the top and the bottom ground plates. The central line's width is relatively large (>1 mm) to create a more uniform high-frequency field above the signal line within the sample, which is important for inductive FMR measurements. Several types of CPWs were used in this work, including the examples shown in figures 3.12 and 3.13.

Figure 3.12: A U-shaped transmission line for inductive measurements.

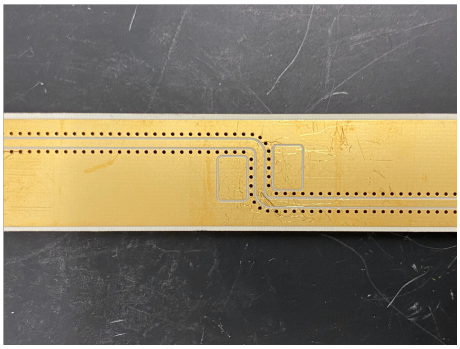

Figure 3.13: An S-shaped transmission line for inductive measurement, with additional contact pads.

For electrical measurements (to be discussed further below), similar but smaller parts of the CPWs have been employed. The devices are typically connected via wirebonding to the CPW, as shown in figure 3.14 for a two-port sample holder. The entire sample holder has been developed during this work, with the help of David Nelson and Erik Hagen, and based on preliminary designs of Chris Safranski and Dr. Barsukov.

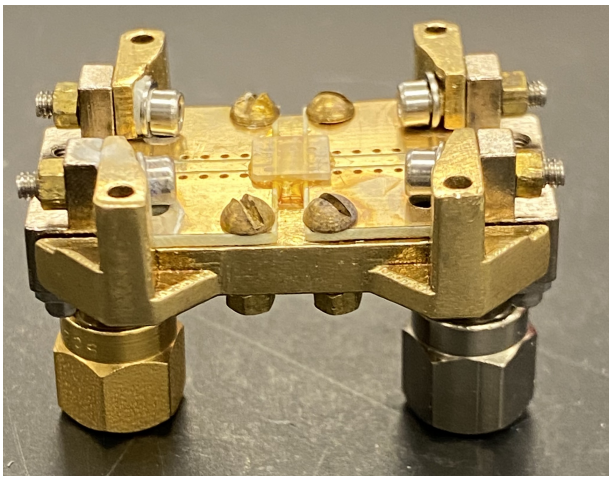

Figure 3.14: A two port sample holder for electrical measurements.

Field Modulation Coils

The field-modulated FMR technique used in this work primarily relies on field modulation coils placed on the poles of the electromagnet (as opposed to e.g., local field modulation). The coils create a low-frequency (1 kHz) magnetic field in the direction parallel to the static field, with sufficient uniformity.

The coils have been fabricated in this work by winding copper wire onto a custom-designed and 3D-printed plastic holder. The AC current is supplied to the coils from a high-power (up to 4 kW) amplifier with a high-power impedance matching. The electrical signal supplied to the amplifier is the reference-out signal from the lock-in, set to be a sinusoidal wave. Typical AC currents used in this work are in the range of few Amperes. Typical modulation field amplitudes range from sub-Oersted to a few tens of Oersted, depending on the magnetic system under investigation.

To obtain the intrinsic linewidth from the magnetic system, the modulation field must be much smaller than the linewidth. Otherwise, overmodulation artifacts, such as

linewidth broadening and even amplitude reduction, may occur. In this work, protocols have been implemented to ensure a sufficient modulation field magnitude at all times. For the rare cases, where overmodulation is needed, a modulation calibration and data processing routine has been developed. It has been used to obtain the intrinsic linewidth from a series of FMR measurements with varying modulation field magnitude B_{mod}.

Figure 3.15 shows the arrangement of modulation coils on an electromagnet during an FMR experiment. The modulation field calibration procedure relies on the linearity of the modulation coils, as expected from the standard relation:

$$B_{mod} = \left(\frac{4}{5}\right)^{3/2} \frac{\mu_0 \, N \, I}{R} = c \, \cdot \, I \tag{3.6}$$

where μ_0 is the permeability of free space ($4\pi \times 10^{-7}$ T$\cdot$m/A), R is the radius of the coils, N the number of turns in each coil and I is the current through the coils. Effects of magnetic hysteresis in magnetic poles and eddy current effects have been omitted, which has been experimentally shown to be a good model.

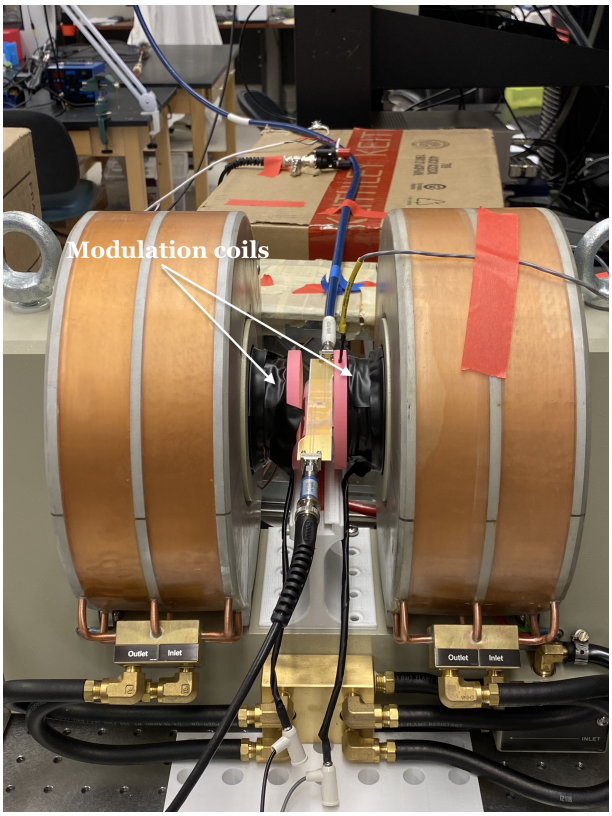

Figure 3.15: The modulation coils after installation on the electromagnet poles.

3.1.2 Spin-torque Ferromagnetic Resonance

The spin-torque ferromagnetic resonance (ST-FMR) is the broadband technique, in which a microwave current is supplied directly into a conductive sample. The microwave current is supplied through a bias-tee. The measurements are carried out using field modulation and lock-in techniques. The microwave current excites (via potentially complex high-frequency spin torques as well as Oersted fields) magnetic oscillations – spin waves. The magnetization oscillations are converted in resistance oscillations due to magnetoresistance effects (whichever present in the magnetic sample). The resistance oscillations at the same frequency as the microwave current mix with the current and create a rectified voltage

that is detected at the lock-in. If, in addition, a DC current is supplied to the sample via the low-frequency port of the bias-tee, resistance oscillation may create a nonzero time-average component that results in a DC resistance variation, changing as a function of the sweeping parameter (e.g., magnetic field). Such a signal, referred to as photoresistance, is detected at the lock-in as well. Using the ST-FMR technique, it is possible to detect FMR signals from nanoscale devices while modifying their magnetic properties (such as damping) by electric current and thermal gradients [82]. The ST-FMR data can be evaluated using the same formalism presented in the previous sections (Eq.(3.3)). The schematic for the ST-FMR measurement is shown in figure 3.16.

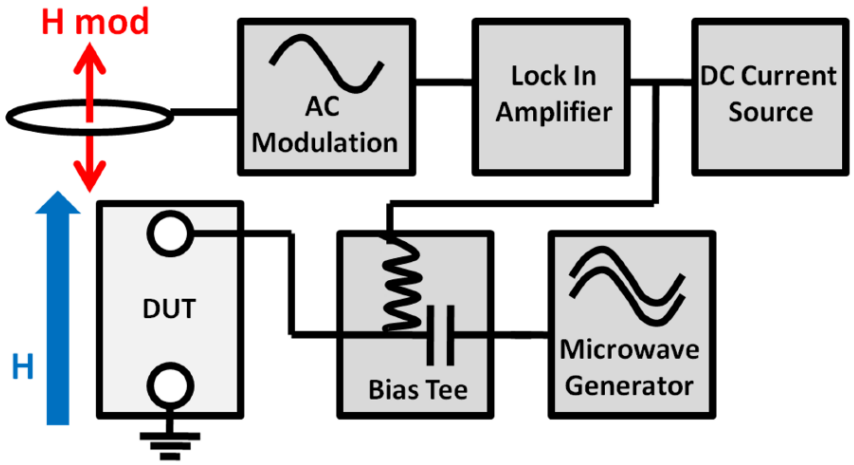

Figure 3.16: The Spin-torque Ferromagnetic resonance (ST-FMR) setup. Adapted from Ref. [83].

Figure 3.17 shows that the ST-FMR spectrum of a YIG/Py nanowire at and I_{dc}=1 μA and T =77K. The data taken at several frequencies are collected into a single three-dimensional plot (with the magnitude of the signal represented by color code, in arbitrary units).

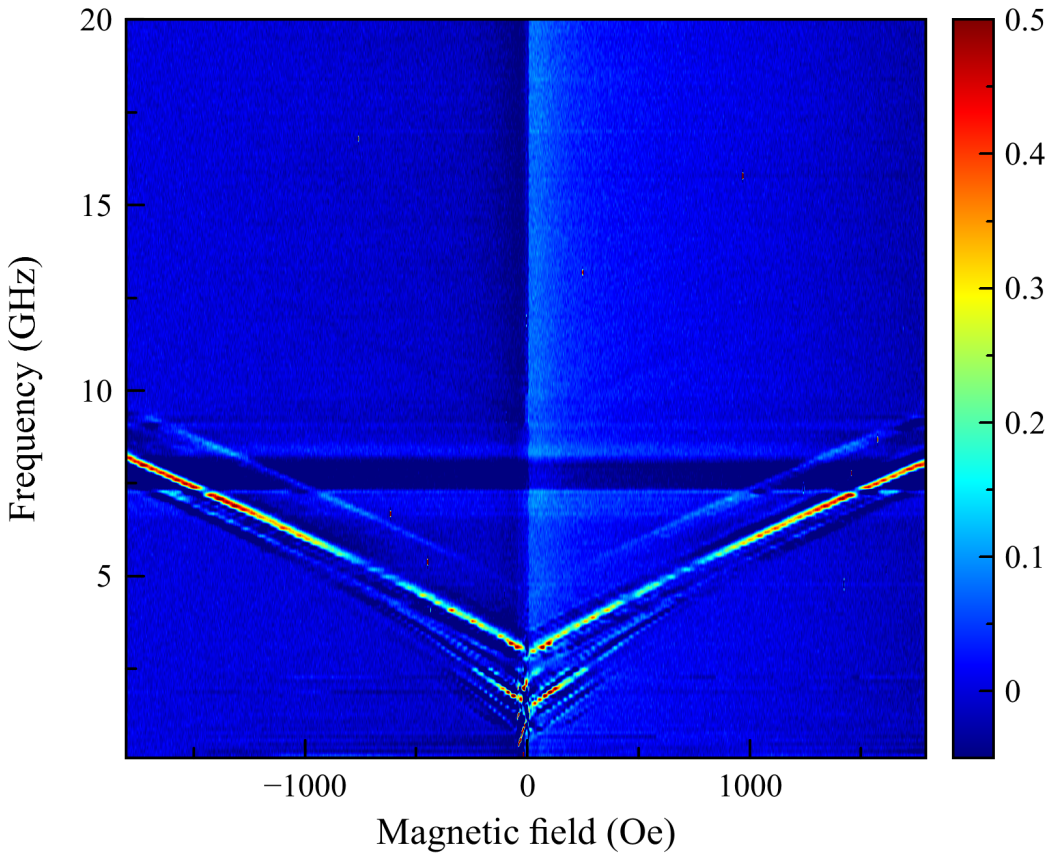

Figure 3.17: The ST-FMR spectrum of a YIG/Py nanowire.

The frequency-field spectrum shows multiple excitations and is comprised of individual ST-FMR spectra, such as shown in figure 3.18. The figure 3.18a shows that the ST-FMR signal of YIG/Py nanowire along the easy-axis at f= 3.0 GHz and I_{dc}=5 μA, and figure 3.18b along the hard-axis at f= 2.5 GHz and I_{dc}=1.75 μA. The YIG spin-wave modes (i.e., the first and second FMR signals) that can be excited in a YIG/Py nanowire is due to the interfacial exchange coupling, which appears in strong hybridization.

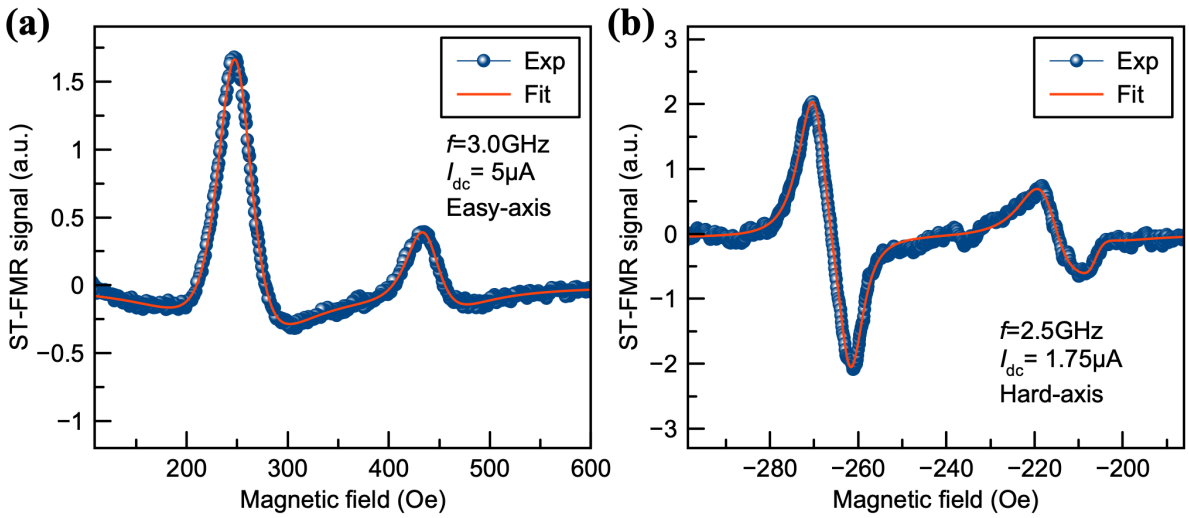

Figure 3.18: The ST-FMR signal of YIG/Py nanowire, (a) easy-axis orientation, and (b) hard-axis orientation.

3.1.3 Field-modulated microwave emission

The microwave signals created by spin-torque oscillators can be minimal, sometimes going to a fraction of femto-Watt. The microwave signals generated in the samples are typically the result of a DC current supplied to the device and microwave frequency resistance oscillations. The resistance oscillations originate from magnetoresistance and spin waves excited in the device. To detect such small signals, the field-modulated microwave emission spectroscopy can be used. It was built in the lab in the course of this work. To detect magnetization oscillations, a spectrum analyzer (see figure 3.19) is employed. However, the setup is significantly modified from the standard operations. Instead of sweeping the frequency at the spectrum analyzer, it is used as a notch filter.

Figure 3.19: E4407B ESA-E Spectrum Analyzer, 9 kHz to 26.5 GHz.

The signal from the sample is first pre-amplified by an ultra-low noise microwave amplifier, such as shown in figure 3.20. The signal is further sent into the spectrum analyzer, where is again pre-amplified. The spectrum analyzer's filters and mixers are set to detect a single frequency. The signal at this frequency is sent to the lock-in amplifier. The microwave signal emitted from the sample is modulated using field modulation. This technique allows us to detect a low population of magnons down to thermal regimes. The setup overview is shown in figure 3.21.

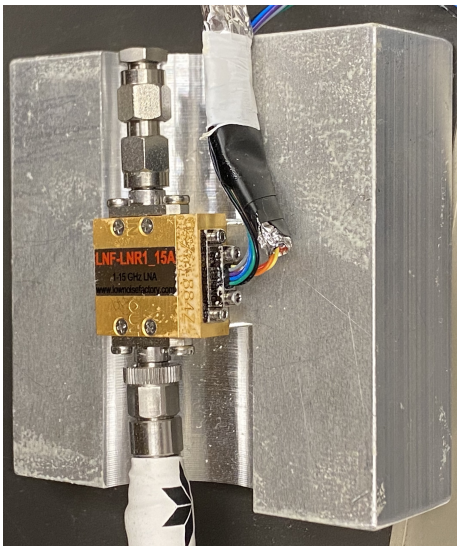

Figure 3.20: LNF-LNR1 15A is an ultra-low noise amplifier operating in the 1-15 GHz frequency range.

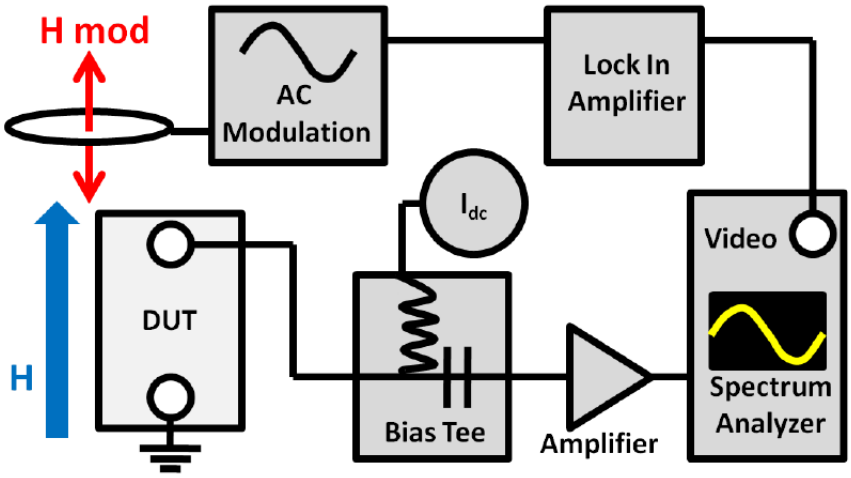

Figure 3.21: Block diagram for the field modulated microwave emission measurement. Adapted from Ref. [83].

In a typical experiment, the magnetic field is swept. The notch frequency of the detection is adjusted for each spectrum using a GPIB interface and a Python script (see the appendix B.1). Due to the field modulation, the detected spectra are field derivatives of the

original spectral response. The overmodulation protocol, discussed above, is applied where necessary. Figure 3.22 shows that the microwave signal of a YIG/Py nanowire along the easy-axis at f= 3.2 GHz and T=77 K. Again the signal magnitude is shown as a function of two parameters: the magnetic field and the DC current. The color plot is comprised of single spectra that are typically measured in the field domain. Figure 3.23 reveals the microwave signal peak amplitude and its integrated value as a function of the DC current. The dramatic increase of the emitted microwave power indicates the onset of magnetic auto-oscillations at the critical current I_{dc} ~1.63 mA.

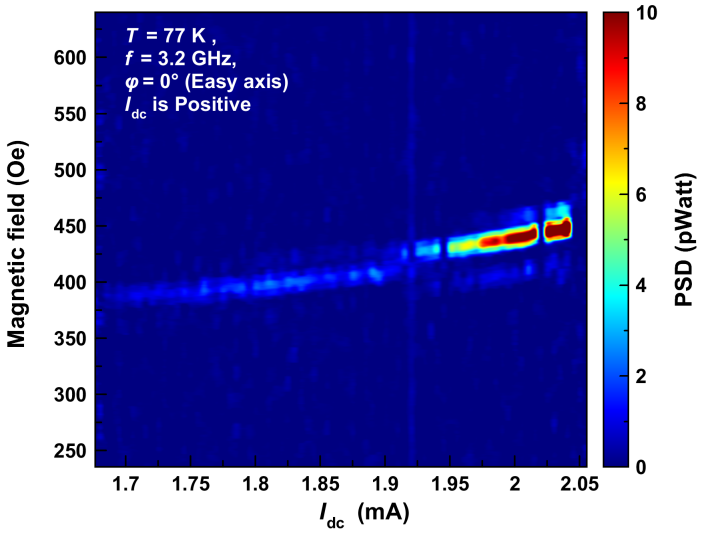

Figure 3.22: The microwave emission of YIG/Py nanowire along easy-axis orientation, at f= 3.2 GHz and T=77K.

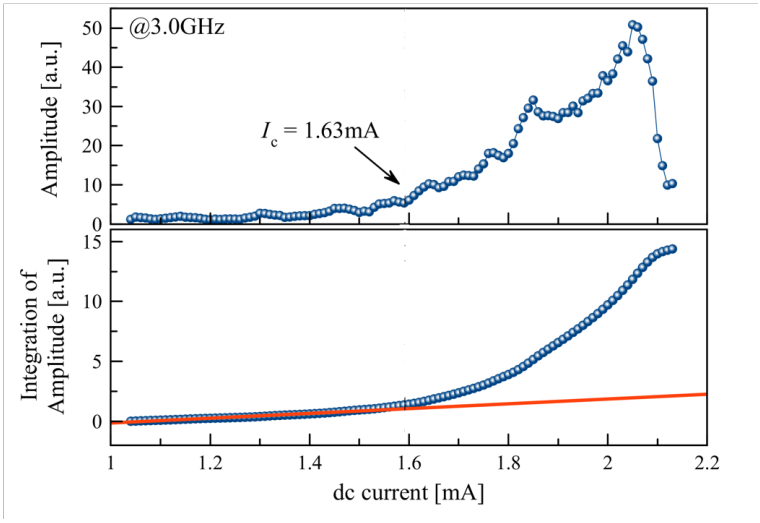

Figure 3.23: The microwave emission amplitude of a YIG/Py nanowire along easy-axis orientation, at f= 3.0 GHz and I_{dc} ∼1.63 mA.

3.2 Magneto-transport characterization

The magneto-transport characterization used in this work is mostly comprised of measurements of longitudinal resistance in the presence of magnetic fields, electric currents, and thermal gradients. Magneto-transport measurements rely on spin-charge effects described in previous sections. In many of the devices studied here, the exact nature of the magnetoresistance (although AMR is typically dominant [30, 84]) or spin current to voltage conversion is not known. However, the magneto-transport experiments contribute significantly to understanding the spin physics of multilayer devices.

Typically in this work, the measurements are carried out with a DC electric field supplied to the sample from an automated low-noise DC source. The voltage is detected using a nano-voltmeter or, in the case of field modulation, using the lock-in amplifier. Figure 3.24 shows resistance measurement of a YIG/Py nanowire as a function of the magnetic

field applied in two different directions with respect to the nanowire axis.

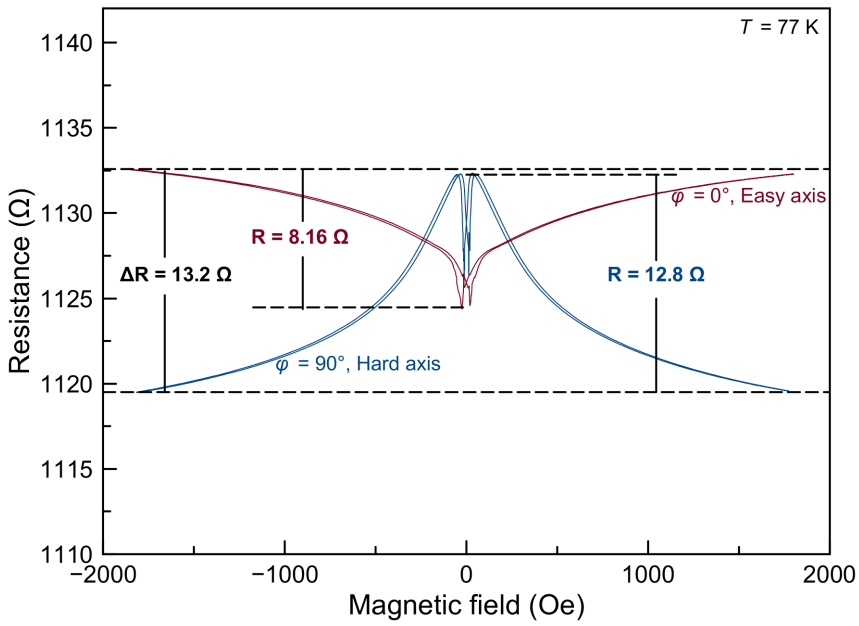

Figure 3.24: Resistance of a YIG/Py nanowire as a function of the magnetic field.

3.3 Cryogenic measurements

The capability to vary the temperatures during the characterization of the devices studied here places an exceptional role. The advantages of cryogenic measurements are as follows: first, measurements at cryogenic temperatures are subject to less thermal fluctuations and noise, which increases the signal to noise ratio and allow for observation of phenomena not detectable otherwise. Second, it allows us to reach high thermal gradients and electric current densities that would otherwise destroy the device. Third, many of the observed phenomena (in particular magnetic phase transitions) are inherently temperature-dependent. In this work, measurements have been carried out using two cryostats: the

vacuum flask and the Helium flow cryostat.

The vacuum flask

The vacuum flask consists of a double-sided wall with a vacuum between the walls, providing thermal insulation. The flask is made of really weak magnetic steel, which allows for placing it in the magnetic field of an electromagnet (see figure 3.25). The flask is filled with liquid Nitrogen. The cap of the flask has custom-designed and 3D-printed in the course of this work to host ports for microwave and low-frequency cables, as well as to allow for venting of the Nitrogen and reducing formation of ice (see figure 3.26). The Nitrogen within the flask undergoes a slow-boiling process, and its temperature is there maintained at the constant boiling point (77 K) at atmospheric pressure. Measurements of up to 12 hours duration can be carried out without refilling the cryostat. For angle-dependent measurements, either the whole flask can be rotated or more frequently used, the electromagnet underneath the flask is rotated (shown further below).

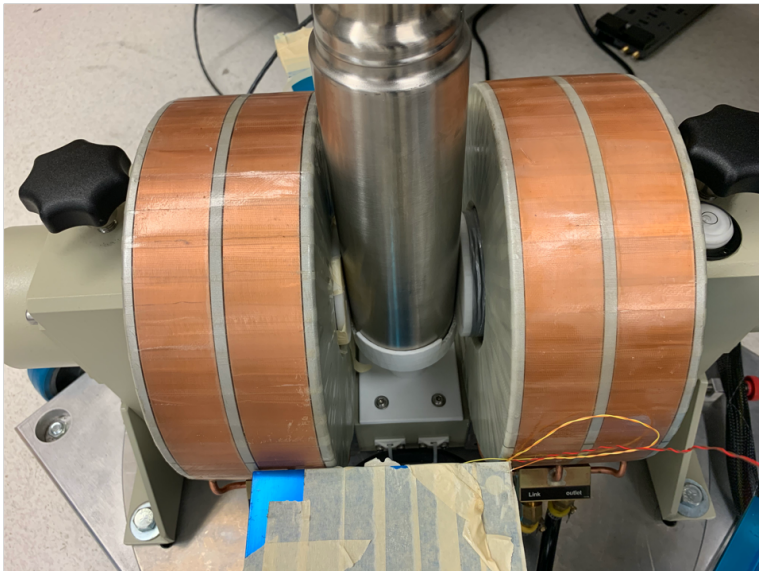

Figure 3.25: The vacuum flask positioned between the poles of the electromagnet.

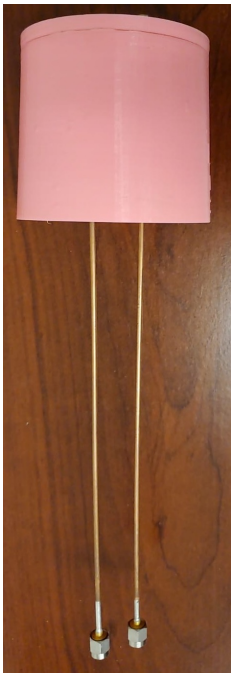

Figure 3.26: The semi-rigid microwave cables build in the 3D-printed cap.

Liquid helium cryostat

In this work, a commercial Helium-flow cryostat (Model 8CN variable temperature cryostat from Cryo Industries of America, Inc.) has been augmented to allow for microwave spectroscopy and magneto-transport measurements. The cryostat temperature range is from 1.4 K to 300 K (see figure 3.27).

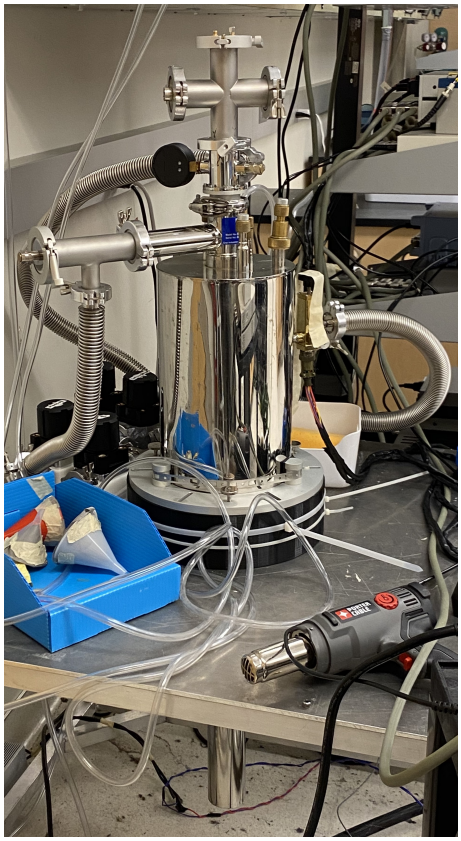

Figure 3.27: Model 8CN variable temperature cryostat.

The cryostat consists of three primary chambers, the sample space, nitrogen space, and helium space. The sample-set in a vacuum, the nitrogen space, is where the liquid nitrogen (LN) is stored, and finally, the helium space is where the liquid helium (LH) is stored. The capillary valve enables the flow of liquid helium to be vaporized into the sample

space, and there is a vent valve on the sample space that passes for the vapor to escape to the lab atmosphere.

In the course of this work, the following adjustments have been made: a table with an appropriate window for cryostat has been constructed, a rotating base for the electromagnet (to be operated with the cryostat, see figure 3.28) has been designed and build, a valve system has been designing and builds to streamline pumping and venting procedures.

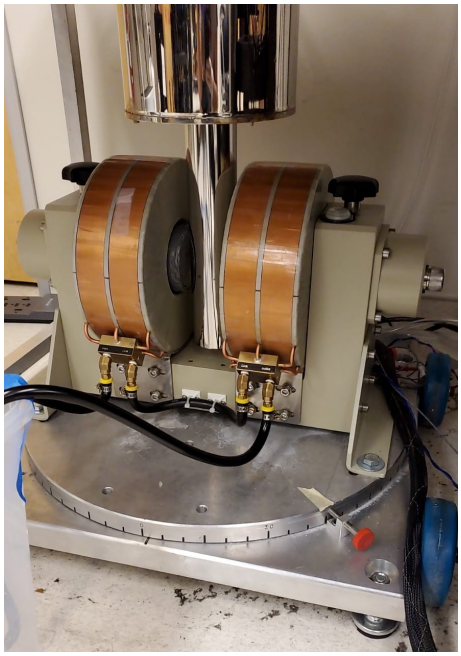

Figure 3.28: The rotating base for the electromagnet.

For expelling moisture from the cryostat, venting protocols with nitrogen and helium gases has been established. For refilling the liquid helium, a flexible transfer line with a valve has been purchased and a transfer protocol established (see figure 3.29). To conduct measurements, the temperature is controlled by adjusting the capillary valve and the heater (see figure 3.30). The temperature reading is coming from the temperature sensor

close to the sample location. The best temperature stability can be achieved by cooling the cryostat down to the lowest temperature and a subsequent slow warm-up with heated helium vapor. A Python script for controlling the temperature controller has been written.

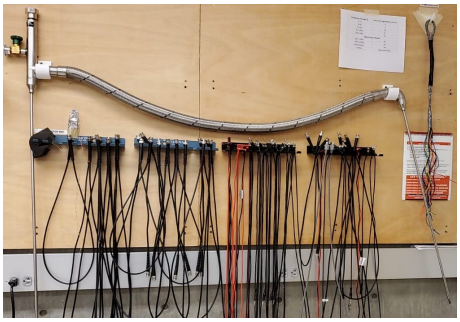

Figure 3.29: The transfer line of liquid Helium.

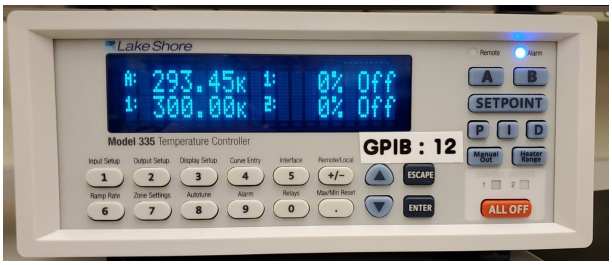

Figure 3.30: The LakeShore temperature controller Model 335.

3.4 Computational modeling

3.4.1 Micromagnetics simulation via MuMax^3

This work was supported by micromagnetic calculations based on a finite-element approach. The calculations were carried out using MuMax^3 software package [85], running on high-performance GPUs on computers in the Barsukov lab and at the Helmholtz Research Center in Dresden-Rossendorf.

In these simulations, the time-dependent solution of the magnetization vector field

is calculated. A model of a magnetic device is first created and divided into cells (meshing procedure). For each cell, the Landau-Lifshitz equation is solved. The effective field for each cell is:

$$\vec{H}_{eff} = -\frac{\delta E}{\mu_0 \, \delta \vec{M}} = \vec{H}_{exch} + \vec{H}_{dipole} + \vec{H}_{ext} + \vec{H}_{anis} + \vec{H}_{therm} \tag{3.7}$$

with exchange field $\vec{H}_{exch}$, dipole field $\vec{H}_{dipole}$, externally applied field $\vec{H}_{ext}$, magnetic anisotropy field $\vec{H}_{anis}$, and a field due to thermal excitations $\vec{H}_{therm}$. The dipole field and the exchange field in one cell depend on the magnetization orientation of other cells, and thus couple the Landau-Lifshitz equations for all cells.

Calculations for YIG/Py nanowires have been carried out to first simulate the experimentally observed spectra by adjusting the standard parameters of the materials involved. Then, spin-wave amplitudes have been mapped out as a function of space. This allows us to understand the nature of the observed modes in the experimental spectra. In particular, the localization of the spin-wave modes can be studied. Examples of MuMax^3 simulations codes are listed in the appendices A.1 and A.2.

3.4.2 Finite element modeling via COMSOL Multiphysics

This work was supported by finite-element simulation using COMSOL Multiphysics, carried out on a high-performance computer in the Barsukov lab. Preliminary studies have been started to investigate and simulate microwave field patterns of planar resonator and waveguides presented in the next section. Furthermore, ohmic heating in nanoscale devices has been calculated.

The device is first modeled using standard material parameters and meshed. Electrical current flowing in one part of the nanodevice is simulated to result in ohmic heating. The heat diffusion is then calculated using the standard heat diffusion equation for all cells of the model. After a steady-state regime (constant local temperature) is reached, the data is mapped in a color plot, and the spatial temperature profiles are evaluated (see figure 4.5). Such simulations are necessary for most of the used devices since, in the nanoscale geometry, even small currents can result in significant local temperature increases and, consequently, in exorbitant temperature gradients. While such effect are common in micro-electronics and usually considered a severe problem, this work will demonstrate how such effects can be used to the benefit of spintronics applications.

3.5 Micro and Nanofabrication

3.5.1 YIG/Py Nanowires

YIG film growth

Most of the Yttrium Iron Garnet (YIG) thin films were provided for this study by Dr. Jing Shi's group. The growth of films (with a typical thickness of 20 nm) was carried out on single-crystal substrates of $Gd_3Ga_5O_{12}$ (GGG, typically in (111) surface orientation) using pulsed laser deposition.

Some of the films were fabricated using radio-frequency sputtering. The GGG substrate was flushed back-to-back with acetone, isopropyl alcohol, and deionized water, before being placed inside the sputtering chamber. The YIG films were deposited and annealed at $\sim$ 820 C°. More details about the YIG film growth processes can be found in

Ref. [86].

Py deposition

The Py thin films were deposited on top of the YIG films at about 5 nm thickness at room temperature using magnetron sputtering with 3×10^{-3} Torr of argon gas in a magnetron sputtering system with a base pressure of $\sim 1\times 10^{-8}$ Torr. The growth rate of Py was $\sim$ 1Å/s. To prevent oxidation of the Py surface, $\sim$ 2 nm Al_2O_3 capping layer is deposited in-situ. The aluminum oxide Al_2O_3 is deposited by reactive sputtering of an aluminum target in an atmosphere of the argon-oxygen gas mixture.

Wire and leads definition

In this work, both electron-beam and UV lithography was employed. The fabrication of nanodevices was carried using e-beam lithography. The YIG/FM bilayer films described above were first coated with the negative resist MAN-2401 of $\sim$100 nm thickness after brief sonication in acetone and, then, isopropyl alcohol. Spin coating the MAN-2401 at 3500 rpm was used for 45 sec. The resist was baked out on a hotplate for 60 sec at 90C°C.

Since MAN-2401 is sensitive ultraviolet (UV) light, its exposure to ambient light was constantly avoided. The resist was patterned into nanowires and leads utilizing e-beam lithography with dosage ranges from 250 - 300 in the Nanometer Pattern Generation System (NPGS) software (see figure 3.31). The typical write current was 13 pA and an area dose of 270 μC/m^2. The center to center distance and line spacing set were to 1 nm. For the leads, the current was raised to 3.2 nA. After the E-Beam Lithography (EBL) writing, the developer (maD-525) was applied for 60 sec, and the sample was rinsed with HPLC water

for 3 min.

After defining the patterns, the sample was ion-milled at an incident angle of 65 ◦ for several minutes (according to calibration such that YIG/FM material is etched down to the substrate: YIG etching rate is 3.7 nm/min). Duty-cycling and water cooling of the sample was used during the ion milling to prevent the sample from overheating. The remaining resist was removed using sonication in acetone.

The subtractive nanopatterning described here has several advantages: first, it produces very smooth edges of the nanostructures, as opposed to side-walls that would occur in a lift-off process and then oxidize and become antiferromagnetic [87]. Second, YIG requires annealing at high temperature, at which the resist would thermally deteriorate. Therefore, lithography procedure involving lift-off would require multiple lengthy fabrication steps.

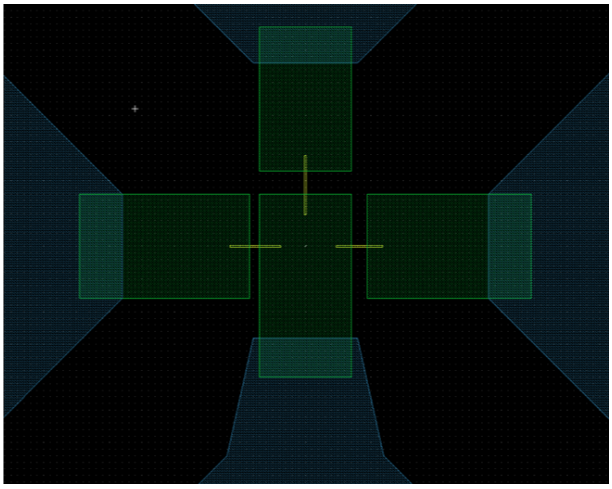

Figure 3.31: The drawing of a typical nanowire array (yellow) and leads.

The resulting nanowire devices are shown in figure 3.32. It is contacted to the coplanar wave guide using wirebonding.

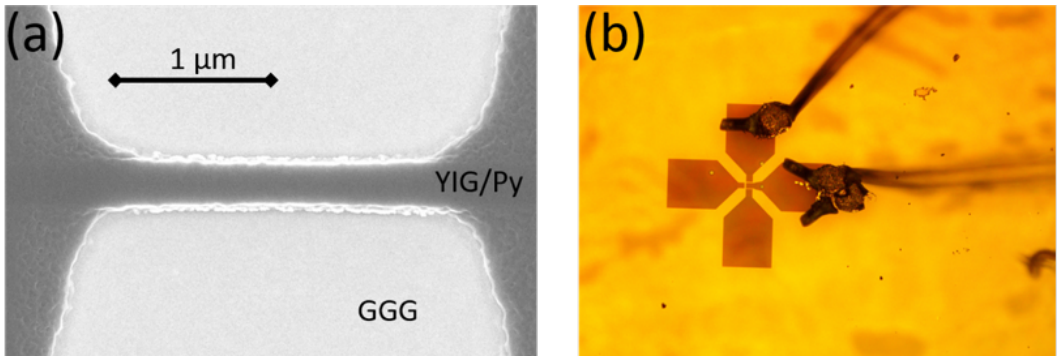

Figure 3.32: (a) The YIG/PY nanowire after finishing all steps of the nanofabrication. (b) The YIG/Py device and the wire-bonds.

3.5.2 Ω - shaped planar microresonator

Several projects carried out in this work relied on the high sensitivity of ferromagnetic resonance and local measurements, that cannot be achieved using conventional CPW or cavity-based FMR. Some of the magnetic systems could also not (or at least not directly) be measured in an ST-FMR experiment. In this work, therefore, planar microwave microscale resonators were developed based on concepts of Refs. [88, 89].

These microresonators were then proven (as discussed in chapter 6) to provide a significant increase of FMR sensitivity to investigate YIG based thin-film microstructure at low temperatures, which represents a significant advancement to measurement capabilities and allowed for studies of YIG based systems that would not be possible otherwise. Moreover, the planar microresonators (PMRs) reduce the radiative damping in magnetic systems and can potentially be used for calibration of extrinsic damping contributions in various magnetic systems.

Photomask

As shown in figure 3.33, the planar microresonator consists of a stripline microwave element with two sidearms providing impedance matching for the Ω-shaped active part, shown in figure 3.34. The active element is inductive – a micro-coil with a single winding – that creates strong localized microwave magnetic fields. A microscale or even nanoscale sample places into the active area is excited by these fields. In resonance, the microwave is partially absorbed in the sample, and thus the microwave reflection coefficient from the microresonator changes.

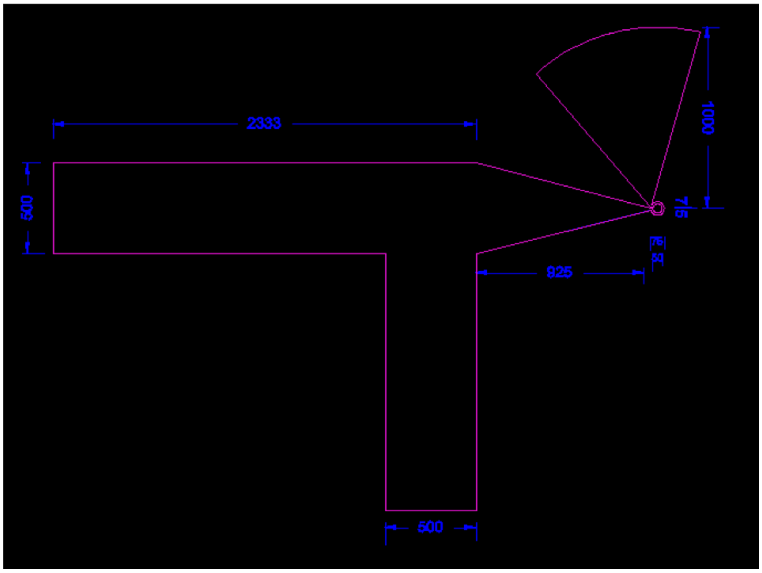

Figure 3.33: The Ω - shaped planar microresonator design.

The resonators are despite the fact that their micro-scale size is too large to be cost-effectively fabricated using e-beam lithography. Optical lithography is used instead. The microresonators must possess high electrical conductivity to achieve high-quality factors. The substrate onto which the microresonators are deposited must, for the same reason, have small dielectric losses. On the other hand, the high thermal conductivity of the substrate

is preferred to avoid local heating of the microwave elements. Sapphire substrate seems, therefore, a suitable candidate for the design of the microresonator. In this work, however, several substrates (sapphire, GGG, Si/SiOx) were used for other technical reasons.

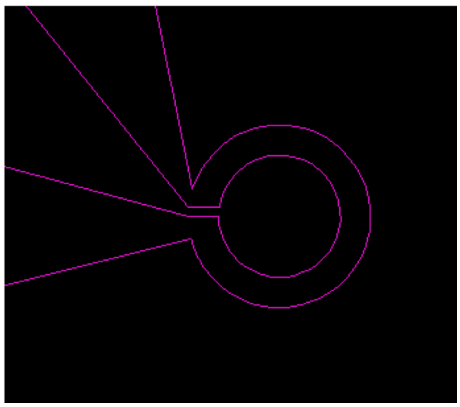

Figure 3.34: The active region of the planar microresonator. Here, the inner diameter of Ω - shaped micro-coil is 150μm.

Photolithography

The photolithography was performed after standard cleaning of the substrate. The substrate was pre-baked on the hotplate for 1.5 min at 180 °C to get remove any organic solvent residues. Using spin coating process at 3000 rpm for 45 sec, a S1813 positive photoresist was deposited to receive a thickness of $\sim$ 1.6 μm. The resist on the substrate was baked on a hotplate for 1 min at 115 °C.

An optical mask was designed (see the previous subsection) in the course of this work and commercially fabricated. The mask was aligned with the substrate. The patterns were exposed for 7-8 seconds with intense UV light. The S1813 resist becomes soluble in the developer after exposure, in contrast to negative photoresist, where the unexposed areas are soluble in the developer (see figure 3.35). Then the patterns were developed using MF

319 developer for 60 sec, and so made ready for the metallization process.

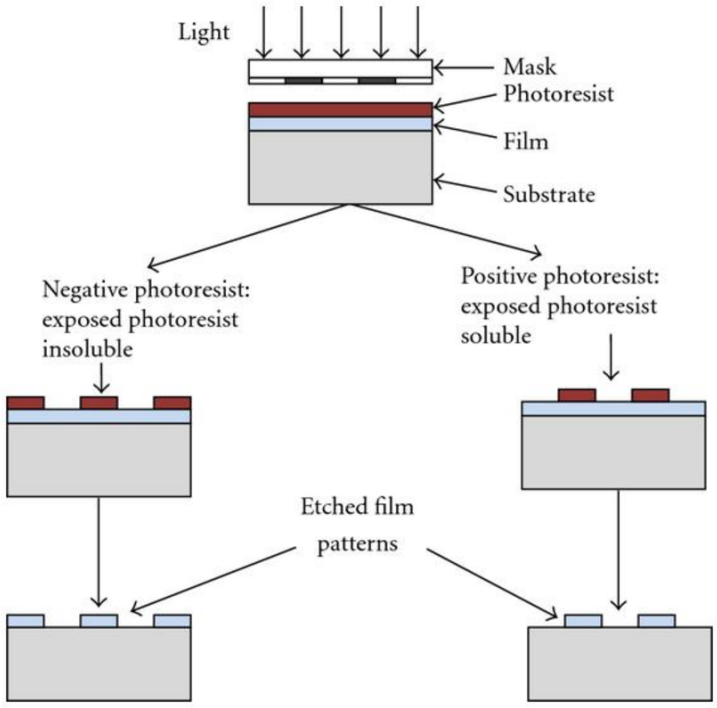

Figure 3.35: The Photolithography procedures using negative or positive photoresist. Source: Bellah M, Christensen SM, Iqbal SM. Nanostructures for medical diagnostics. Journal of Nanomaterials. 2012

PMR metallization

For the metallization of the planar microresonators, e-beam evaporators of the Temescal BJD 1800 system were used. Three layers of metal were deposited. The first layer contains Titanium (Ti) of 5 nm thickness, and acts as an adhesion/wetting layer for the next layers. The bulk of the metallization consists of a copper (Cu) layer of 400 nm thickness. The capping layer is 50 nm of Gold (Au), to prevent the underlying layers from oxidation. An optical micrograph of the active region of a planar microresonator is shown in figure 3.36.

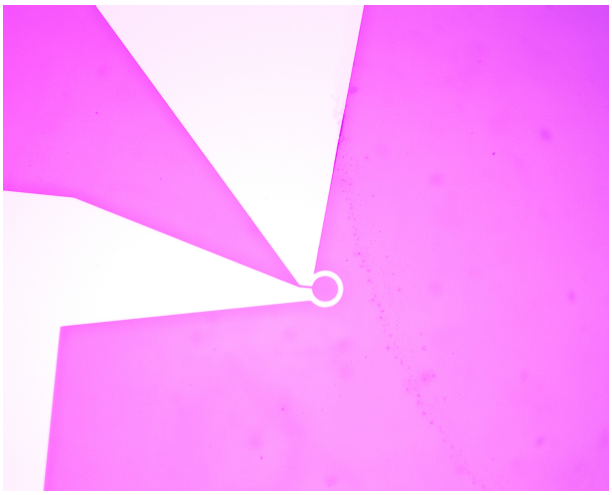

Figure 3.36: The optical image of the Ω - shaped PMR with inner diameter of 150 μm.

Chapter 4

Two-magnet nano-oscillator with enhanced spin-charge conversion and thermal spin torque

Next-generation spintronic applications require material properties that can hardly be met by one material candidate. Here we demonstrate that enhanced spin-charge conversion and energy-harvesting thermal spin currents can be realized by combining insulating and metallic magnets. We develop a nanowire device consisting of an yttrium iron garnet and permalloy bi-layer (see figure 4.1). An interfacial temperature gradient drives the nanowire magnetization into auto-oscillations at GHz frequencies. Interfacial spin coupling and magnetoresistance of the permalloy layer translate spin dynamics into sizable microwave signals. The results show prospect for energy-harvesting spintronic devices and present an experimental realization of magnon condensation in a heterogeneous magnetic system.

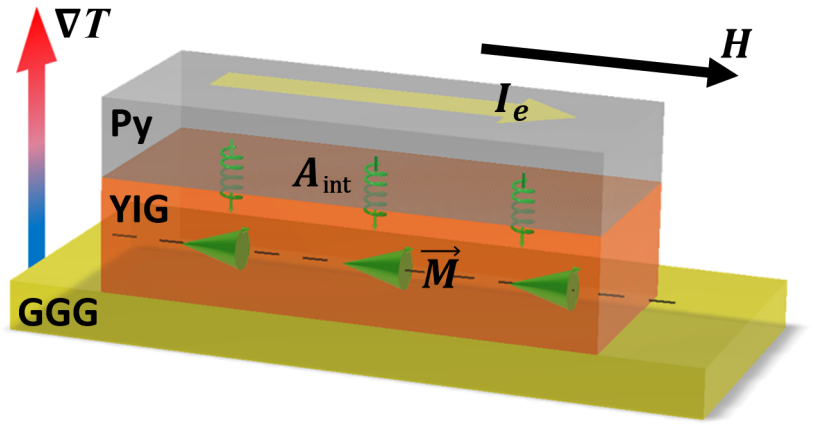

Figure 4.1: Nano-wire shaped two-magnet nano-oscillator under an interfacial temperature gradient. Magnetization dynamics is hybridized across the subsystems of YIG and Py, by virtue of interfacial exchange coupling.

4.1 Introduction

Energy-harvesting control of spin dynamics [22] and sizable spin-charge conversion[60] are central topics of spintronic research. Magnetic insulators have recently risen as promising material candidates for spintronic applications [90, 91, 92]. They possess low magnetic damping and thus reduce energy dissipation [47, 93]. Once viewed as a challenge for heat management, the low thermal conductivity of magnetic insulators bears an opportunity for spintronic devices via heat recycling. Interfacial heat flow in ultra-thin bi-layers of the ferrimagnetic insulator, yttrium iron garnet (YIG), and platinum has recently been shown to inject a spin current sufficient to induce auto-oscillations of YIG magnetization [66], creating a spin-torque oscillator driven by waste heat.

While magnetic insulators help to avoid shunting of electrical currents, they possess no intrinsic means of spin-charge conversion and rely on proximity-mediated effects [60, 94].

In YIG/Pt systems, the spin Hall magnetoresistance allows for read-out of spin information. However, it is rather small (typically 10^{-1}-10^{-2} %)[37, 66], which presents an obstacle for integration of insulators in reliable spintronic applications.

Metallic ferromagnets, on the other hand, possess intrinsic, sizable spin-charge effects based on spin-orbit interaction, which can be employed for electrical read-out of static and dynamic magnetic states [95, 96, 97]. Recently, these spin-charge effects have received much attention as tunable sources of spin currents [57, 98, 99]. Spin injection using anomalous Hall effect[61, 64, 100], planar Hall effect [101], rotational-symmetry spin-orbit effect [62] in multilayers, and spin-orbit torques in a single ferromagnetic layer [102] have been experimentally realized.

4.2 Experimental procedure

Here, we propose to exploit the virtues of insulating and metallic magnets and fabricate nanowires from thin-film bi-layers of YIG and permalloy (Py=$Ni_{80}Fe_{20}$). We find that spin coupling at the metal-insulator interface and anisotropic magnetoresistance (AMR) in Py allow for electrical read-out of spin dynamics in YIG. Furthermore, the application of the interfacial temperature gradient from ohmic heating drives the nanowire into magnetic auto-oscillations, translating into sizable microwave signals. Our findings demonstrate that nanoscale heterostructures based on a combination of metallic and insulating magnets offer both sizable spin-charge conversion and thermal spin-torques, thus enabling next-generation energy-harvesting spintronic applications. The observed auto-oscillations, moreover, show an experimental realization of magnon condensation [103] in a two-magnet system with

hybridized spin-wave modes.

Using sputtering deposition [104], we prepare multilayer thin films consisting of $Gd_3Ga_5O_{12}$ (GGG substrate)/YIG(20 nm)/Py (5 nm)/AlOx(2 nm). The top layer prevents Py from oxidation. By means of negative e-beam lithography and ion milling, we fabricate nanowire devices (180 nm width, 3.4 μm length) which fan out into sub-millimeter [66] large electric leads (Figure 4.2a).

4.3 Results and discussion

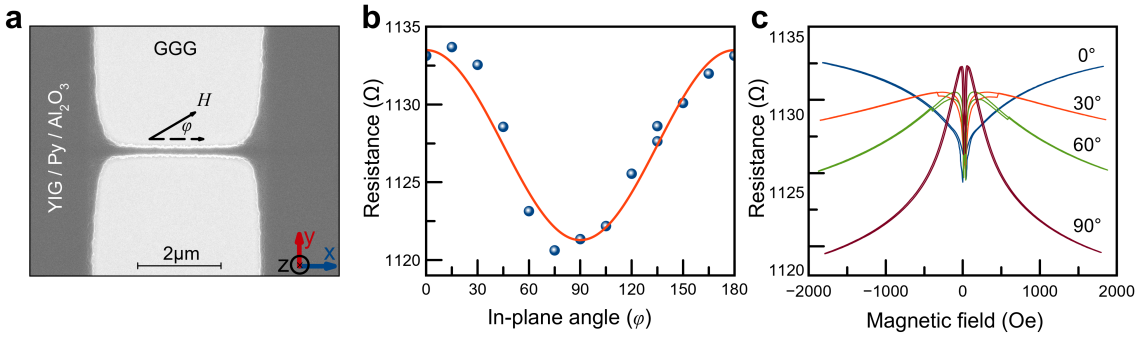

Figure 4.2: Magnetoresistance of the nanowire device. (a) Scanning electron micrograph of the nanowire. H is the external magnetic field, applied in the film plane at angle φ with respect to the nanowire axis. (b) Device resistance as a function of field angle at $H = 1.6$ kOe. (c) Device resistance as a function of the magnetic field for different in-plane angles φ. All measurements in this work are carried out at 77 K.

We apply a large magnetic field $H = 1.6$ kOe in the sample plane, and assess the device resistance as a function of field angle φ measured with respect to the nanowire axis (Figure 4.2b) within the film plane. All measurements are carried out in a cryostat at 77 K thermal bath temperature. As expected for the anisotropic magnetoresistance of Py [46], the resistance follows $R = R_0 + \Delta R \cos(2\varphi)/2$ behavior, where $R_0 = 1127\,\Omega$ and $\Delta R/R_0 = 1.24\%$ is the magnetoresistance ratio. Figure 4.2 (c) shows the device resistance

as a function of the magnetic field. Again as expected [46], in the hard axis (at $\varphi = 90°$ due to the shape anisotropy of the nanowire) the curve is bell-shaped, and in the easy axis ($\varphi = 0°$) the curve is V-shaped. However, large resistance drops near zero-field and incomplete saturation along the easy axis to interfacial exchange at the YIG/Pt interface.

The presence of interfacial spin coupling is anticipated to have an impact on the spin-wave spectrum of the device [105, 106, 107, 108, 109, 110, 111]. While zero coupling should leave individual spin-wave spectra of YIG and Py layers nearly unchanged (except for the dipolar interaction), the strong coupling should significantly hybridize and delocalize the spin waves over both, YIG and Py, layers and can lead to spin-wave modes of acoustic and optical type [105].

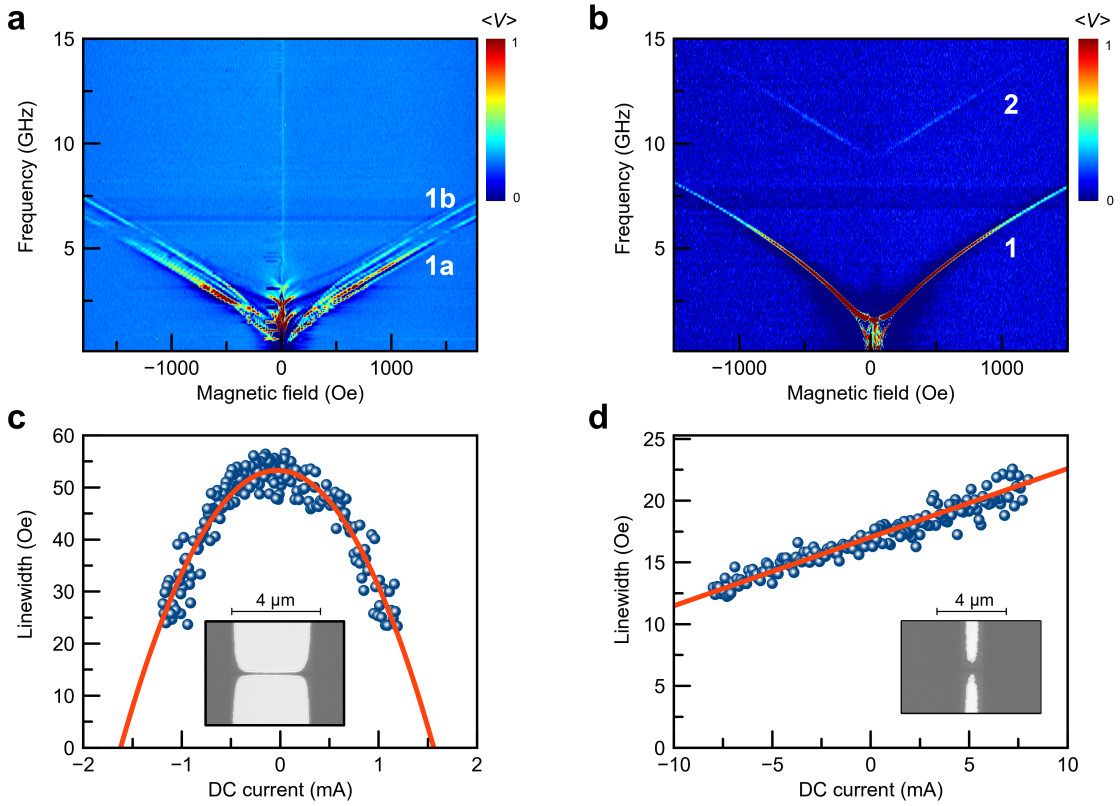

Figure 4.3: Spin-torque ferromagnetic resonance. (a) Spin wave spectrum of the long nanowire at the hard axis. The normalized ST-FMR signal $\langle V \rangle$ is color-coded. (b) Spin wave spectrum of the short nanowire (i.e., nanoconstriction) at the hard axis. (c) Linewidth of the lowest spin-wave mode for the long nanowire in the easy axis at $f = 6.8\,\mathrm{GHz}$. (d) Linewidth of the lowest spin-wave mode of the short nanowire (i.e., nanoconstriction with dimensions 750 nm by 1 μm) $\sim$20 deg off easy axis at $f = 2.5\,\mathrm{GHz}$.

To evaluate the spin-wave spectrum, we carry out spin-torque ferromagnetic resonance (ST-FMR) measurements at the hard axis with field modulation [112] on the nanowire shown in figure 4.3a presents one group of spin waves as a function of frequency and field. This group is dominated by two modes labeled '1a' and '1b'. The spin-wave spectrum is not only determined by the coupling between YIG and Py, but also by the nanowire dimensions. We thus carry out ST-FMR on a much shorter nanowire (i.e., nanoconstriction) (displayed in inset of figure 4.3 (d)). As shown in figure 4.3b, the frequency-field data presents one

spin-wave mode, labeled '1', similar to the spin waves observed in the longer nanowire. At higher frequencies, another spin-wave mode, labeled '2' is found.

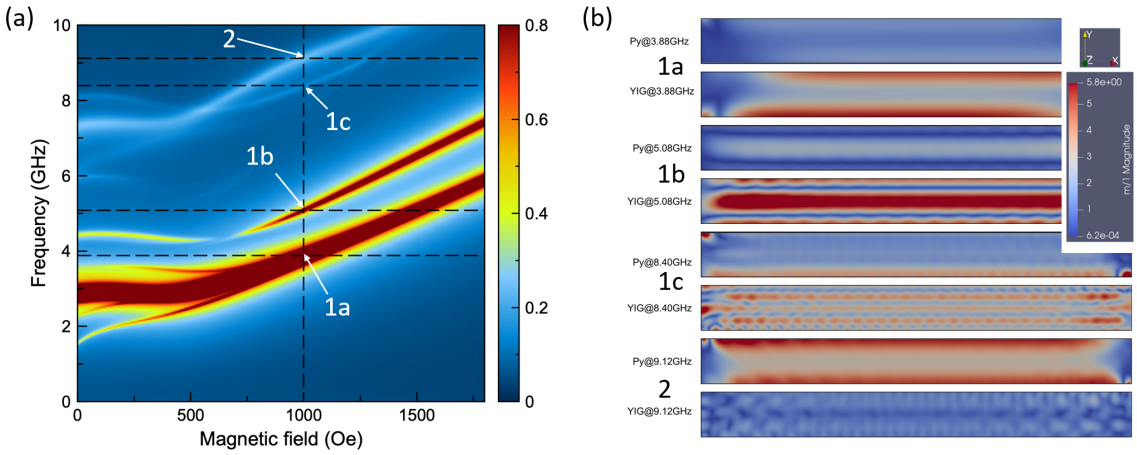

Figure 4.4: Micromagnetic simulations of YIG/Py nanowire.

To assess the nature of these spin waves, we perform micromagnetic simulations using MuMax^3 package [113] for typical material parameters of YIG and Py (figure 4.4). The device geometry: length 3.8 μm, width 190 nm, YIG thickness 20 nm, Py thickness 5 nm. Cell size: 3.7 nm×5.9 nm×5.0 nm, temperature: 0 K, excitation by a sinc-pulse with lateral symmetry of 50 Oe (in z-direction). YIG magnetization is 175 kA/m, Py magnetization is 800 kA/m, YIG exchange constant is 3.5×10^{-12} J/m, Py exchange constant is 13×10^{-12} J/m.

Figure 4.4a Shows the spatially averaged, normalized FFT of transverse components of magnetization is representative of the excitation of spin waves close to hard-axis. Excitation magnitude is color-coded in arbitrary units. Modes '1a' and '1b' are excited in the experiment; mode '1c' is not sufficiently excited in the experiment. Mode '2' is sufficiently excited in short nanowires (i.e., nanoconstriction) and some of the long nanowires

(supposedly due to symmetry-breaking defects present). Figure 4.4b Shows the lateral profile of excitations in YIG and Py layers for different frequencies at the external field of 1000 Oe. With increasing frequency, delocalization, and hybridization of spin waves increases. At low frequencies, the phase difference of magnetization precession between YIG and Py layer is nearly 0; at higher frequencies, the phase difference approaches π. We find the best agreement between experiment and micromagnetics for $A_{\mathrm{int}} = 0.4\,\mathrm{pJ/m}$ – a moderately large, ferromagnetic-type coupling at the interface. The spin waves of the lower-frequency group ('1a' and '1b') are predominantly localized in the YIG layer. They correspond to the normal spin-wave eigenmodes [46, 114] of a nanowire (see figure 4.4) – the number of nodes increases with increasing frequency. The higher-frequency mode ('2') corresponds to the nanowire's lowest-order eigenmode but is predominantly localized in the Py layer. Due to the symmetry of the excitation field in the FMR experiment (Oersted field of the Py layer), the group '2' and higher-order spin waves of the group '1' are very weakly excited [46], and thus not visible in figure 4.3a.

Micromagnetic analysis reveals that spin-wave modes at lower frequencies, while delocalized over both layers, are more strongly excited in one layer (see figure 4.4). For instance, the mode '1a' is predominantly localized in YIG, but also drags the magnetization of Py. Such delocalization allows for detecting this mode electrically via magnetoresistance of Py. While at low frequencies, the magnetizations of YIG, $\vec{M}_{\mathrm{YIG}}$, and Py, $\vec{M}_{\mathrm{Py}}$, precess nearly in-phase (acoustic modes), with increasing frequency the phase difference approaches π (optical modes). Moreover, the delocalization increases and the spin-wave mode become strongly hybridized.

To explore the possibility of manipulating the spin dynamics of the two-magnet devices, we analyze the ST-FMR linewidth, which is representative of the effective damping. The linewidth of the lowest mode '1a' of the long nanowire is shown in figure 4.3 (c) as a function of electric DC current sent through the Py layer. The linewidth decreases for both polarities of the bias current in the easy axis $\varphi = 0\,\mathrm{deg}$. The observed decrease of the damping cannot be explained by any known spin-orbit torque generated by electric current in Py[115] : (i) In particular, the spin Hall effect produces a spin current with polarization $\vec{\sigma}$ parallel to $\hat{y}$ and thus [95] does not contribute to damping-like torque ($\propto \vec{M}_{\mathrm{YIG}} \times \vec{M}_{\mathrm{YIG}} \times \vec{\sigma}$) in easy axis. (ii) The Anomalous Hall torque[61, 64, 100] is zero for parallel orientation of electric current and Py magnetization, which is the case for easy axis. (iii) The Planar Hall torque[101] is zero when magnetization lies in the film plane. (iv) The Rotational-Symmetry torque proposed in Refs. [62, 115] is zero for parallel orientation of YIG and Py magnetizations. Furthermore, spin-orbit torques are generally odd in electric current and cannot explain the symmetric behavior shown in figure 4.3 (c).

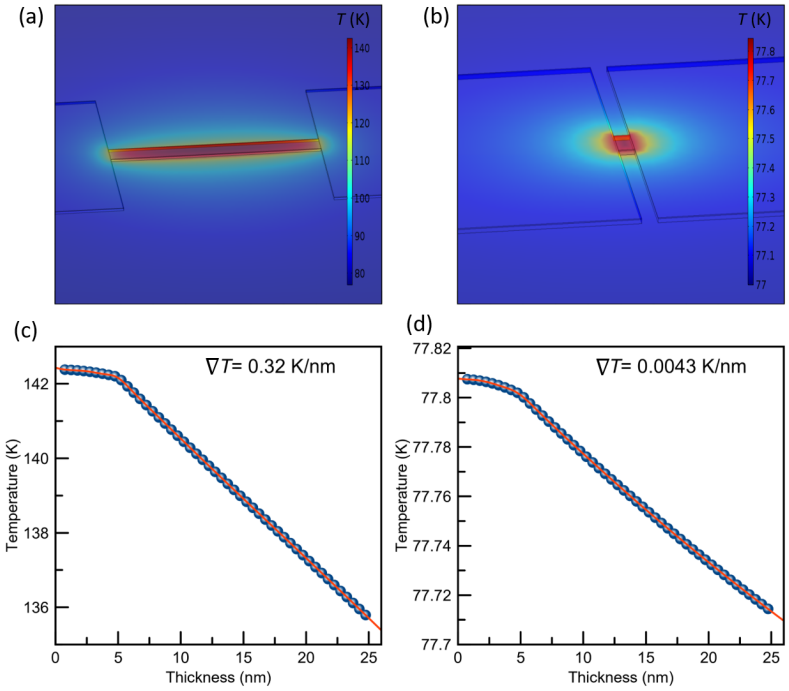

Figure 4.5: Finite-element simulation (in COMSOL Multiphysics) of temperature profile under ohmic heating of the Py layer. (a) Lateral profile of temperature of a long nanowire at I=1.87 mA. (b) Lateral profile of temperature of a short nanowire (i.e., nanoconstriction) at I=1.66 mA. (c,d) Depth profiles of the temperature, counting the thickness from the top of the Py layer.

On the other hand, ohmic heating in the Py layer is nearly quadratic in electric current. Using finite-element simulations by COMSOL Multiphysics (Figure 4.5), we estimate a notable temperature gradient across the layers of $\sim 0.3\,\mathrm{K/nm}$ at $\sim 1.8\,\mathrm{mA}$ for the long nanowire. The temperature gradient generates an anti-damping spin-torque via spin Seebeck effect [66, 116, 117, 118], that is independent of the DC current polarity, consistent with the data in figure 4.3 (c). In the short nanowire (i.e., nanoconstriction), the heat easily dissipates into the adjacent electrical leads, which reduces the temperature gradient to $\sim 0.004\,\mathrm{K/nm}$. With such a small temperature gradient, the spin Seebeck torque is negligible. The linewidth of the lowest spin-wave mode in figure 4.3 (c), therefore, depends linearly

on the electric current, which is characteristic for spin-orbit torques (described above).

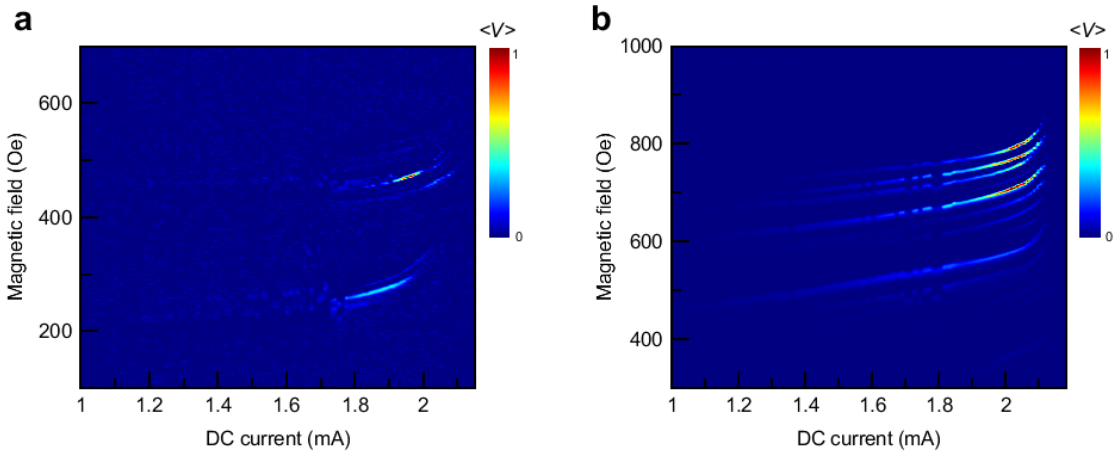

Figure 4.6: Auto-oscillations of magnetization of the long nanowire. The sample is wire-bonded to a co-planar waveguide, and the emitted microwave signal is passed through co-axial microwave cables to a bias-tee, pre-amplifier, and spectrum analyzer. The measurements are carried out using field modulation and single-frequency detection. (a) Microwave signal at 3.0 GHz emitted from the nanowire in the easy axis. Normalized detected voltage $\langle V \rangle$ is proportional to the emitted microwave power density. (b) Microwave emission in the hard axis. At low electric currents, a weak signal of thermally populated is visible. Above a current of approximately 1.8 mA, microwave emission is strongly increased, and the emission field shows a pronounced non-linear shift.

The linewidth of the long nanowire in figure 4.3 (c) can be extrapolated to zero at about approximately 1.6 mA, marking the critical current at which the intrinsic damping of the lowest spin-wave mode is fully compensated by the spin Seebeck torque. Once the intrinsic damping is compensated, the magnetization transitions into auto-oscillations in the absence of external microwave drive [6]. The auto-oscillations are translated into electric signals via the effective magnetoresistance of the nanowire [66].

We supply electric DC current to the long nanowire and measure the microwave signal emitted from the device (into a microwave circuit [66], as described in Supporting Information). In figure 4.6a, the signal detected at 3.0 GHz is shown as a function of

the magnetic field and DC current for the easy axis. We find that at low currents, the signal is nearly zero indicating only weak thermal excitation of the spin waves. Above the current of approximately 1.8 mA, a sudden onset of the microwave signal is observed, which is characteristic of auto-oscillations [6]. By comparing the frequency-field relation of spin waves from auto-oscillations and from the ST-FMR experiment, we identify the lowest modes predominantly localized in the YIG layer to participate in auto-oscillations. With increasing current (around 2 mA), the emission field shows a strong non-linear shift, which again is indicative of the auto-oscillatory regime [6, 66, 119].

The microwave emission data, shown in figure 4.6a for the easy axis and in figure 4.6b for the hard axis, present similar critical currents for the onset of auto-oscillations. Inversion of magnetic field direction (Figure 4.7) does not notably change the critical current. The isotropy of the critical current further supports our conclusion – in the long nanowire, isotropic [66] thermal spin-torque due to spin Seebeck effect is strong and drives the auto-oscillations, while spin-orbit torques are significantly smaller. For the short nanowire (i.e., nanoconstriction), nearly free of the spin Seebeck effect, the critical current can be estimated to over 10 mA, based on the ST-FMR linewidth in figure 4.3 (c). Indeed, we observe no microwave emission from this device in the experimentally accessible current range.

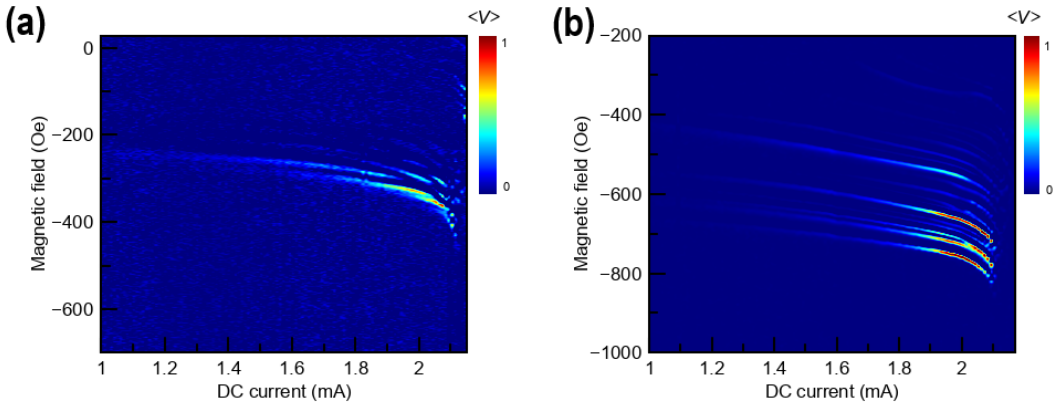

Figure 4.7: Microwave emission from the long nanowire in negative fields. (a) Easy-axis emission. (b) Hard-axis emission. The normalized detected voltage $\langle V \rangle$ is proportional to the spectral power density. Emission spectra very similar to those detected at positive external fields are observed.

The emergence of thermally driven magnetic auto-oscillations observed here can be understood as a manifestation of bosonic condensation of incoherent magnons into a coherent low-frequency magnon state. In order to reach the threshold of this instability, the thermal magnons need to be pumped to the chemical potential exceeding the natural frequency of the coherent low-frequency mode [103, 117, 120, 121]. Raising the chemical potential in one of the ferromagnets (here, YIG) by heat flow from another one (Py), in two-magnet heterostructures, presents a conceptually novel scenario for magnetic auto-oscillations.

In Ref. [65], Bender et al. proposed a theoretical model for generating thermal spin currents between two ferromagnetic layers separated by a nonmagnetic metallic spacer. A temperature gradient across the layers injects a spin flow from the warmer ferromagnet into the spacer (raising its electronic spin accumulation), which is then transmitted downstream into the colder magnet. In our bi-layer system, the spacer is missing, so that the spin

angular momentum is driven directly across the interface between the magnetic layers. Magnetic and possibly also magneto-elastic hybridization across the interface could result in an enhancement of the effective magnonic spin accumulation induced in the YIG layer, facilitating the onset of the condensation instability.

The underlying transfer of the spin angular momentum from the incoherent to the coherent spin precession can formally be understood in terms of an anti-damping torque entering the equation of motion for the latter, in proportion to the chemical potential of the incoherent magnon gas [122]. The chemical potential is zero in equilibrium but can be raised or lowered, depending on the orientation of the heat flux between the magnetic layers. We generically expect the hotter (colder) side to correspond to the decrease (increase) of the magnon chemical potential [123].

Thermal spin-torque in heterogeneous systems, such as two-magnet systems investigated here, has remained unexplored experimentally and theoretically. We consider two possible microscopic mechanisms contributions to the torque: (i) Spin waves are excitations of magnetic moments residing in the d-electrons, which are coupled by s-d exchange with conduction electrons in Py [124]. Thus, the conduction electrons possess a higher temperature than spin waves, which are delocalized over both warmer and colder layers. The conduction electrons serve as a source of energy and angular momentum and thermally generated magnons in the nanowire beyond their thermal equilibrium, thus exerting a thermal spin-torque similar to the conventional spin Seebeck in YIG/Pt. In the two-magnet system, however, the spin Seebeck effect is different in that a temperature difference between the magnonic and electronic sub-systems within one heterogeneous magnetic system

creates the anti-damping torque. (ii) Since the spin waves at higher frequencies show a higher degree of delocalization, and they are more susceptible to thermal excitations in the Py layer. The energy and angular momentum of higher-frequency magnons redistribute to the lower-frequency magnon states, creating a population beyond thermal equilibrium and exerting thermal spin-torque [103, 117, 120, 121].

While our results demonstrate that thermal spin-torque leads to damping modification and auto-oscillations, they do not allow for a quantitative comparison of contributions due to the magnon-electron and (magnon-magnon mechanisms. However, the temperature gradient needed to reach auto-oscillations in our two-magnet nanowires and YIG/Pt nanowires of Ref. [66] are similar. This allows for a conjecture that the magnon-magnon mechanism, which is only present in two-magnet systems, is unlikely more effective than the magnon-electron mechanism. The delocalized nature of spin waves offers an effective means for spin-charge conversion in applications based on magnetic insulators. We estimate the power spectral density of the emitted microwave signal from auto-oscillation to $\sim$1 pW MHz^{-1} (see figures 4.8), which is three orders of magnitude higher than electrical signals obtained on YIG/Pt systems.

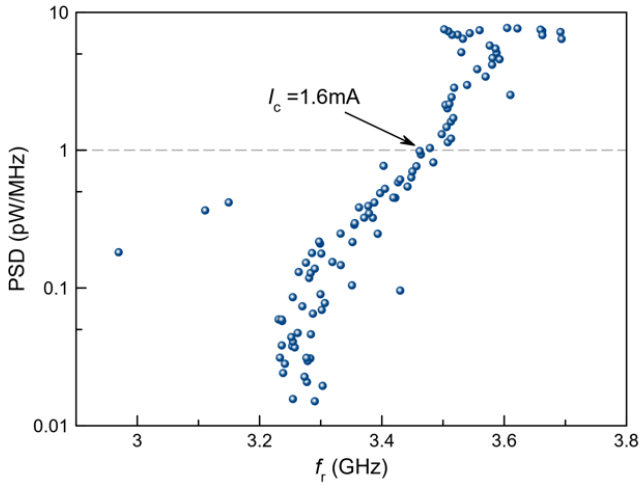

Figure 4.8: Power spectral density of the signal emitted in the frequency domain at constant field of -310 Oe in the hard-axis configuration and current range from 1.0 mA to 2.2mA.

4.4 Conclusions

We find that heterostructures based on a combination of metallic and insulating magnets bear an excellent promise for next-generation spintronic applications. Via interfacial spin coupling, magnetization dynamics in the magnetic insulator translates into magnetization precession of the ferromagnetic metal. Inherently large magnetoresistance in ferromagnetic metal allows converting this magnetization dynamics into sizable electric signals. With a moderate interfacial spin coupling, the lower-energy spin-wave modes are predominantly localized in one layer, while higher-energy modes show an increased level of hybridization and delocalization. Heat flow due to the temperature gradient across the layers leads to magnon condensation into the lower-energy modes, driving the magnetization into auto-oscillations. We demonstrate that a two-magnet system can be used to realize thermally driven spin-torque nano-oscillators. The results show a prospect for energy-

harvesting spintronic devices and advance our understanding of magnon thermodynamics in heterogeneous magnetic systems.

Chapter 5

Soliton excitations in a two-magnet nano-oscillator

As demonstrated in the previous chapter, thermal bias (gradient) in a two-magnet nanoscale heterostructure creates an effective anti-damping torque that leads to magnetic auto-oscillations of the hybridized spin-wave modes. The spin-orbit torques in the YIG/Py based nanodevices were found to be small and to play a negligible role in the observed magnetization dynamics. Despite the dominant role of the thermal spin torque, the question remains unanswered whether the potential of the spin-orbit torques for spintronic applications could be realized in the two-magnet heterostructures proposed in this work. The spin-orbit torques, originating from metallic ferromagnets, as described in Chapter 2, present with unusual symmetries and efficiencies that, despite some experimental works, remain not fully understood. Here, nanodevices based on two-magnet heterostructures are investigated in the critical and supercritical current regimes in a broad range of fields

and frequencies. In addition to spin-wave auto-oscillations, high-amplitude auto-oscillatory modes with solitonic behavior are observed. While the theoretical model for the observed modes remains to be fully formulated, the results suggest that the spin-orbit torques from the metallic ferromagnet play an important role in stabilizing the soliton excitation.

5.1 Introduction

When magnetic systems are driven by anti-damping torque supercritically in specific configurations of the magnetic energy landscape, the character of the auto-oscillations [8, 125, 126, 127] may change substantially. An example is shown in figure 5.1 from Ref. [128]. In a point-contact spin torque oscillator, electrical current is passed from one metallic ferromagnet (reference layer) into another separate metallic ferromagnet (free layer) through a nanoscale electrical connection made of a nonmagnetic metal. The electrical current is spin polarized in the reference layer and exerts an anti-damping torque on the free layer in the region of the point-contact.

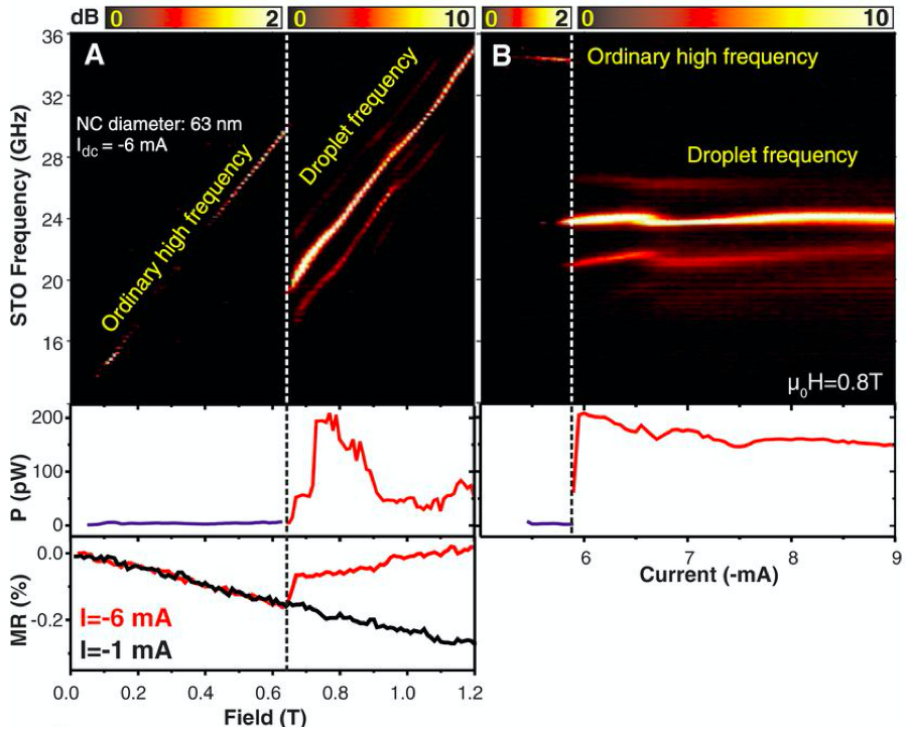

Figure 5.1: (A) Frequency of the point-contact spin torque oscillator as a function of magnetic field. The ordinary auto-oscillation and droplet soliton oscillation is observed. (B) Frequency of the auto-oscillatory modes as a function of DC electric current through the point-contact (nano-contact diameter is 63 nm). Source: Ref. [128].

When magnetic systems are driven by anti-damping torque supercritically in specific configurations of the magnetic energy landscape, the character of the auto-oscillations [8, 125, 126, 127] may change substantially. An example is shown in figure 5.1 from Ref. [128]. In a point-contact spin torque oscillator, an electrical current is passed from one metallic ferromagnet (reference layer) into another separate metallic ferromagnet (free layer) through a nanoscale electrical connection made of a nonmagnetic metal. The electrical current is spin-polarized in the reference layer and exerts an anti-damping torque on the free layer in the region of the point-contact.

With increasing current, another auto-oscillatory mode appears, as shown in fig-

ure 5.1b. This mode frequency is significantly lower than that of the ordinary spin-wave mode, which indicates a phase transition of the dynamic excitation in the system. This transition may be dependent on magnetic anisotropy or external magnetic field (as shown in figure 5.1(a, subset). The observed auto-oscillatory mode referred to as a magnetic droplet, which is one of the examples of soliton magnetic excitations. Such excitations are distinct through amplitude spin precession and self-localization – these effects lead to strongly modified energy landscape that results in an excitation frequency lower than that of the ordinary spin waves. Indeed, as the data shows, the soliton regime's signal amplitude indicates spin precession angles that must reach values of 90∘ and beyond. The observed solitonic excitation can thus be thought of as a formation of a dynamic domain wall oscillating at a low frequency.

Here, magnetization dynamics of YIG/Py two-magnet heterostructure based nano-oscillators is investigated in the critical and supercritical regimes.

5.2 Experimental procedure

The fabrication for the devices studied here follows the procedures described in the previous chapter. A 23 nm thick of YIG film was grown on Gadolinium Gallium Garnet $Gd_3Ga_5O_{12}$ (GGG) substrate by sputtering. The 5 nm thick of Py film was deposited by sputtering on top of YIG film and capped by aluminum oxide (Al_2O_3) layer of 2 nm (see figure 5.2b). The devices were fabricated by electron beam lithography into 200 nm wide and 3 μm long nanowires by ion milling. The contact leads are made from the same YIG/Py/AlOx multilayer. The magnetotransport, ST-FRM, and microwave emission mea-

surements have been carried out using the same methods as described in the previous chapter.

5.3 Results and discussion

The magnetoresistance (MR) measurements were performed for YIG/Py nanowire at 77 K with the magnetic field swept from 1800 to -1800 Oe. Figure 5.2a shows the experimental data for the hard-axis (ϕ=90°). The typical bell-shaped resistance curve is observed. The electrical resistance increased when the DC current increased from 0.7 mA to 1.2 mA. The magnetoresistance data is again consistent with the shape anisotropy of the nanowire and anisotropic magnetoresistance of Py. The nanowire geometry 5.2b (longer than the devices studied in the previous chapter) does not notably change the magnetotransport behavior of the device.

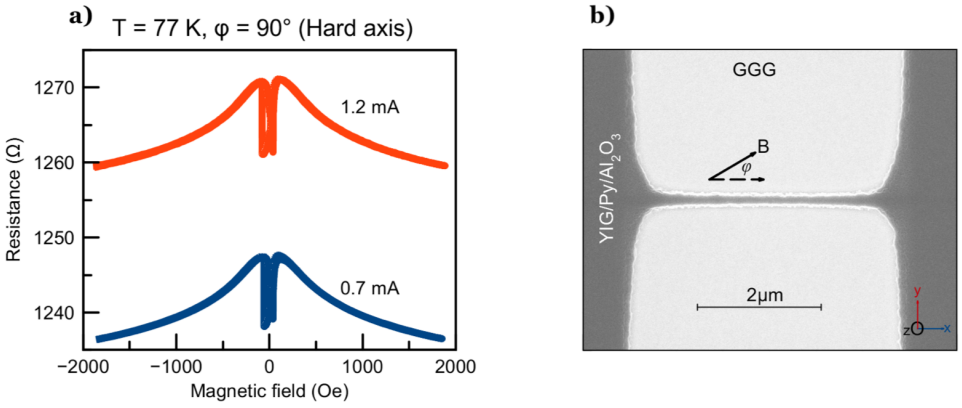

Figure 5.2: (a) The magnetoresistance in the hard-axis (ϕ=90°) configuration. (b) The scanning electron micrograph of the long YIG/Py nanowire.

In the low field regime, the magnetoresistance curve presents with a drop that, as described above, is likely to be related to an exchange coupling of the YIG layer and

Py layer, and the formation of domain walls or other magnetic texture in the device [129]. Characteristic transitions in the magnetoresistance hysteresis are observed at low fields and shown in figure 5.3. Micromagnetic simulations of field-induced magnetization reversal in a nanowire without leads do not show such sharp transitions in the hysteresis. While realistic simulations on nanowire models, which would include fanning out into multilayer leads, could not be carried out due to the large size of the model, it is reasonable to assume that the regions, where the nanowire transitions into the leads, are the main seeds for the formation of domain walls during the magnetization reversal.

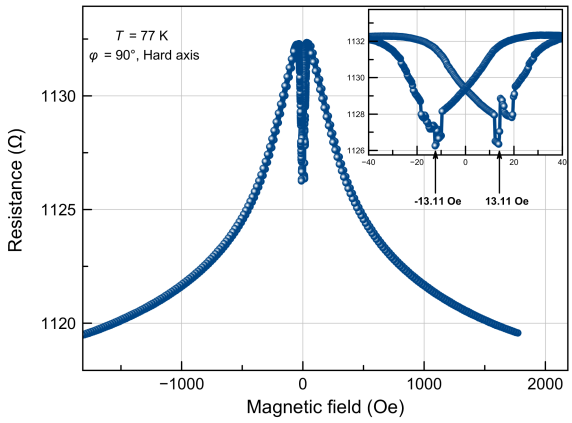

Figure 5.3: The magnetoresistance hysteresis in the hard-axis configuration (ϕ=90°) at 0.1mA. Inset: low-field region presents with characteristic transition features in the hysteresis curve.

To evaluate the spin-wave spectrum of the long nanowire, spin-torque ferromagnetic resonance measurements are carried out. Figure 5.4 shows the spin-wave spectrum presents with the lower-frequency branch, which as discussed in the Chapter 4, originates from the spin waves with predominant localization in the YIG layer. In the easy-axis configuration, the lowest-energy mode of this branch is shown in a frequency-field plot in

figure 5.4a.

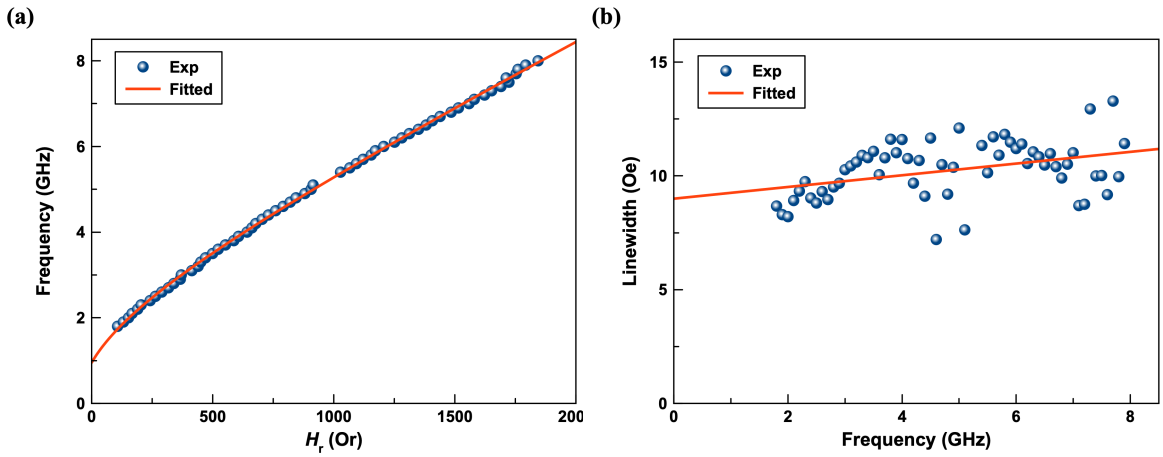

Figure 5.4: Spin torque ferromagnetic resonance on the long YIG/Py nanowire in the easy-axis configuration at 77 K. The lowest-energy mode of the YIG-like spin wave branch is evaluated. (a) The frequency-field relation. (b) Linewidth versus frequency.

The Kittel equation cannot accurately describe the spin-wave in the nanowire [130] since the latter does not include exchange coupling and confinement effects. However, in a poor approximation, the data is fitted, which returns the following fitting parameters: effective magnetization $4\pi M_{eff}$ of 2279 Oe, g-factor – 2.04, and the anisotropy field ~ -50 Oe (see figure 5.4a). The spin-wave linewidth in YIG/Py nanodevices, as described in Chapter 4 and in Ref. [66], cannot be evaluated quantitatively with sufficient accuracy. However, relative changes of the linewidth can in some cases, be assessed. For the long nanowire in the easy-axis configuration, the linewidth is shown in figure 5.4b. The Gilbert damping parameter is estimated with 7.36×10^{-4} within the expected range for the YIG damping. This indicates that the intrinsic damping of YIG may dominate the damping of the hybridized mode. However, the inhomogeneous broadening is with 8.99 Oe relatively large, which is again suggestive of the low accuracy of the linewidth evaluation methods in

the YIG-based nanodevices.

The entire spin-wave spectrum of the long nanowire at 77 K in the easy-axis configuration is shown in figure 5.5 as a function of frequency and field.

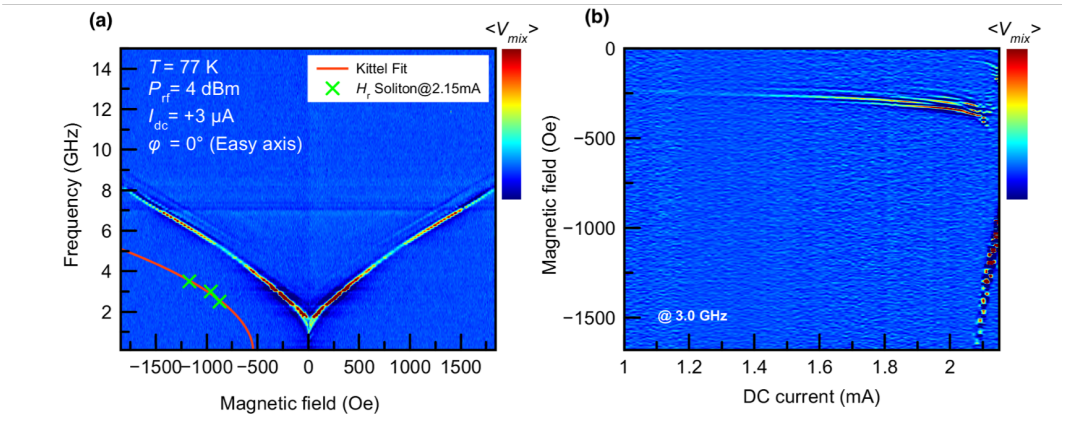

Figure 5.5: (a) The ST-FMR signal as function of frequency showing the spin wave spectrum of the long nanowire in the easy-axis configuration at 77 K. The green symbols indicate the frequency-field relation of the new auto-oscillatory mode. The red curve is guide to the eye. (b) Microwave emission signal as a function of field and DC current in the easy-axis configuration at 3 GHz at 77 K.

With the color scale chosen, the spin wave mode branch of Py-like mode is not visible, but the YIG-like modes' spectrum is very similar to that presented in Chapter 4. Upon application of DC current to the device, microwave emission spectroscopy is carried out. The results are shown in figure 5.5b for the frequency of 3 GHz at low DC currents, only a weak thermal signal is visible. Comparison with the ST-FMR data in figure 5.5a shows that the observed thermal signal originates from the YIG-like modes of the nanowire. At a critical current of approximately 1.8 mA, the thermal modes transition into auto-oscillations. The signal amplitude increases significantly. The field at which the auto-oscillations occur still corresponds to nearly that of the YIG-like modes. At a DC current of $\sim$ 2 mA, a notable nonlinear frequency shift occurs.

Surprisingly, at super-critical currents above 2 mA an additional mode is visible. In the color plot of figure 5.5b, this mode seems to originate from the auto-oscillations of the YIG-like mode. At the high current, the multiple YIG-like spin-wave modes undergo the largest nonlinear frequency shift; and the modes seem to consolidate into the new auto-oscillatory mode.

The new mode's field of auto-oscillations lies at much higher (absolute) values than that of the auto-oscillations of the YIG-like modes. This fact indicates that the new auto-oscillatory mode origin does not lie in ordinary spin-wave modes present in the nanowire. The microwave emission spectroscopy is carried out at multiple frequencies to assess the new auto-oscillatory mode's frequency-field relation. Within the figure 5.5b, the field of the new mode is evaluated at some particular current. The frequency-field relation is summarized in the figure 5.5a. The frequency increases with increasing field. The red curve is a simple guide to the eye showing that the new mode follows a similar behavior as the ordinary spin waves, but its frequency is reduced by almost a factor of two.

Moreover, the new auto-oscillatory mode shows a gigantic nonlinear frequency shift. To make a comparison with the ordinary spin-wave auto-oscillations, their nonlinear shift is estimated as follows. With increasing current in the peri-critical regime, the field of the ordinary auto-oscillations increases in absolute value. Given the slope of the ordinary spin-wave modes in the frequency-field relation of figure 5.5a, this corresponds to an effective decrease of the frequency and thus to the negative nonlinear frequency shift. For the new auto-oscillatory mode, the situation is different. With increasing DC current, the absolute value of the field decreases. Since the new auto-oscillatory mode has the same, positive,

slope in the frequency-field relation as the ordinary spin waves, the negative field change corresponds to an effective increase of the frequency and a positive nonlinear frequency shift.

Figure 5.6 shows individual spectra of microwave emission spectroscopy for 2.5 GHz in the easy-axis configuration. The significantly different behavior of emission from the ordinary spin waves and the new mode is evident. The current dependence of the new auto-oscillatory mode is evaluated and shown in figure 5.6b. Nearly linear behavior of the emission field versus DC current is found for three microwave frequencies. The slope in this, rather narrow range of frequencies, is similar.

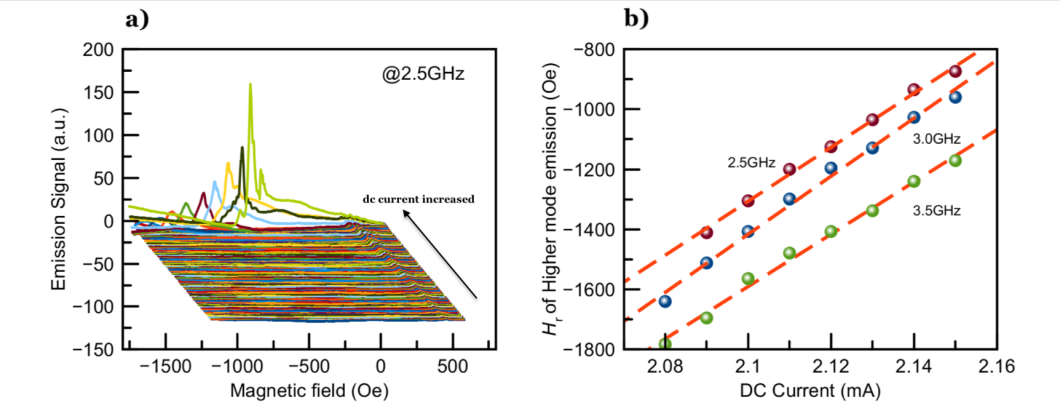

Figure 5.6: (a) The emission signal versus the magnetic field at 2.5 GHz along the easy-axis. (b) The resonant field of the emission signal versus the DC current.

Figure 5.6a also demonstrates the enormous difference of the amplitudes of the ordinary spin-wave auto-oscillations and that of the new mode. The strongest mode of the extra-ordinary auto-oscillatory branch is two to three orders of magnitude larger than the ordinary emission. Quantitative analysis of the non-integrated amplitude is shown in figure 5.7 on a logarithmic scale. A sudden jump of the amplitude is observed when

the ordinary auto-oscillatory mode transitions into a new mode. The extra-ordinary high emission amplitude likely originates from the anisotropic magnetoresistance of Py [131, 132, 133]. However, a very rough estimation of the precession angle that would lead to such high amplitudes puts the picture of the ordinary low-angle precession in question. It is reasonable to assume that the extra-ordinary emission originates from effective precession cone angles of tens of degrees. At such high misalignment of spins, it is appropriate to speak of domain walls like excitations. This, on the other hand, may also involve domain wall magnetoresistance in Py.

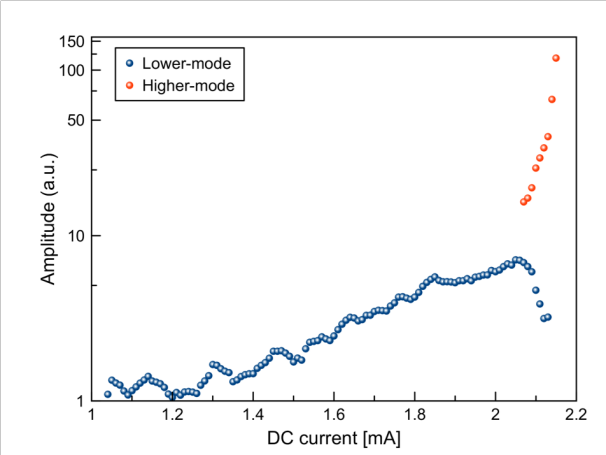

Figure 5.7: The amplitude of the emission signal along the easy-axis at 3.0 GHz.

As shown in figure 5.8, the linewidth of the emission signal is evaluated from the thermal emission regime at low currents to the super-critical regimes of the extra-ordinary mode. While, again, the absolute values of the linewidth bear substantial inaccuracy, the linewidth can be compared in relative terms. The linewidth is assessed in the field-domain. A simple recalculation into the frequency domain reveals that the emission-quality factor of the ordinary and extra-ordinary auto-oscillatory modes is very similar.

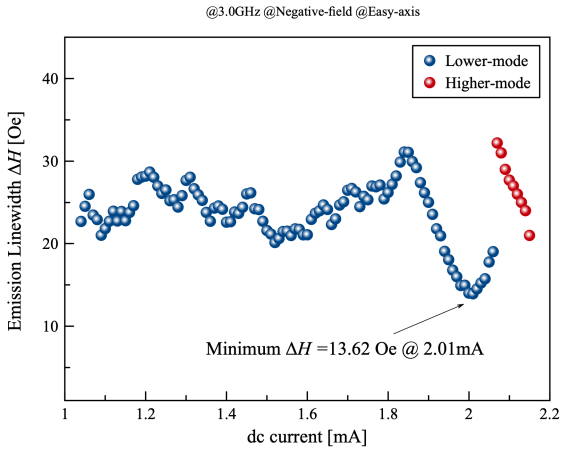

Figure 5.8: The linewidth of the emission signal in the the easy-axis configuration at 3.0 GHz.

In the following, the dependence of the extra-ordinary mode on the magnetic field direction and polarity is assessed. As shown in figure 5.9, the emission of the extra-ordinary mode is found in both easy-axis and hard-axis configuration. The general behavior in the hard-axis is comparable to that in the easy-axis: relative frequency-field, nonlinear frequency shift, and extremely high emission amplitude of the extra-ordinary mode follow the pattern discussed above.

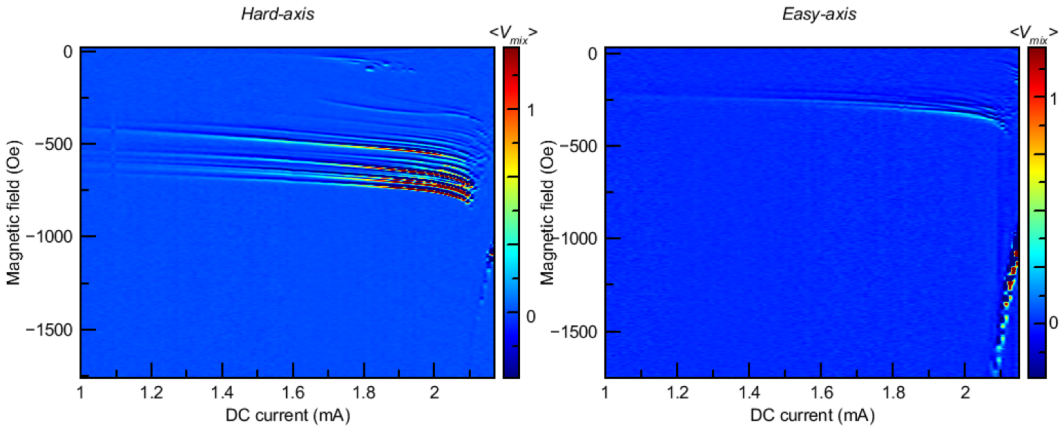

Figure 5.9: Microwave emission signal of a long YIG/Py nanowire in the easy-axis and hard-axis configuration at 3.0 GHz.

Surprisingly, as demonstrated in figure 5.10, the extra-ordinary mode's occurrence depends on the polarity of the magnetic field. In the easy-axis configuration, after reversing the magnetic field polarity, the extra-ordinary mode can be found. The amplitude of the extra-ordinary mode, however, decreases significantly. The overall signal-to-noise ratio in figure 5.10a is low – it could not be deduced whether the low quality is due to experimental difficulties or intrinsic to the nano-device upon magnetic field reversal. More detailed and repeated measurements would be necessary to answer these questions. However, the significant experimental complication is that the emission measurements in the super-critical regime are carried out at very high electrical currents and thus frequently destroy the nano-devices via electro-migration and thermal deterioration. Systematic and repeated measurements are thus very challenging.

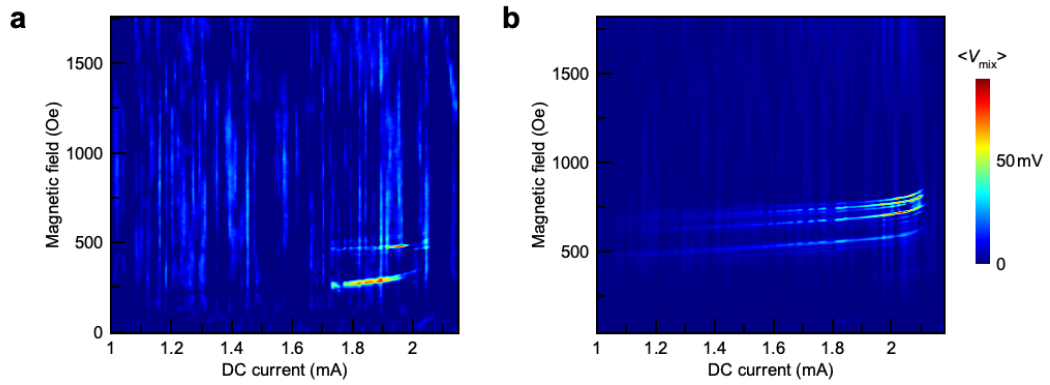

Figure 5.10: (a) The emission signal along the easy-axis and positive field at 3.0 GHz. (b) The emission signal along the hard-axis and positive field at 3.0 GHz

Even more surprising is, however, that the extra-ordinary emission mode disappears upon the reversal of the magnetic field in the hard-axis configuration. As shown in figure 5.10b, the ordinary auto-oscillatory mode follows the expected behavior, which indicates that the magnetic field reversal does not significantly alter the micromagnetic state of the nanodevice. On the other hand, the extra-ordinary mode may be absent due to the hysteretic behavior of highly non-linear modes, such as the extra-ordinary mode must be. Nonetheless, the field modulation used in the microwave emission experiments would likely (at least partially) lift the mode's hysteretic character. Based on the symmetry of the hard-axis configuration, another hypothesis must be discussed. The spin-orbit torques in the YIG/Py nanodevices, as discussed in Chapter 4, play a secondary role for the ordinary auto-oscillations, since the thermal spin-torque drives them. However, even a smaller spin-orbit torque may have a stabilizing or destabilizing effect on the formation of the extra-ordinary auto-oscillatory mode. The effective/cumulative spin-orbit torque (due to SHE, AMR/PHE, AHE) is larger in the hard-axis configuration than in the easy-axis configuration. It may thus have a crucial effect on the formation of the extra-ordinary

mode.

5.4 Conclusions

This chapter concludes that the extra-ordinary mode observed in the emission spectra is a nonlinear dynamic mode of solitonic behavior similar to the droplet modes described in the introduction section and shown in figure 5.1. The transition of the auto-oscillations from ordinany spin-wave modes into the extra-ordinary mode, the low frequency of the mode, the exceptionally high signal amplitude, and nonlinear frequency shift support the picture of a dynamic soliton forming in the nanowire. The soliton mode has been observed only in the long nanodevices. In the short nanodevices (see nanocontrictions in Chapter 4), the thermal torque is insufficient to drive any auto-oscillations. In the medium-long nanowires, the thermal spin torque is comparable to that in the long nanowires, since the critical currents for the ordinary auto-oscillations are very similar. The absence of the soliton mode in the medium-long nanowires may be related to the localization of the soliton boundaries. The dynamic "domain wall" of the soliton is likely to form in an area of spatially varying magnetic parameters, such as the area where the nanowire fans out into the leads. The size of the soliton and the size of the wire are thus interrelated. The presented results call upon efforts to formulate a theoretical model for dynamic solitons in two-magnet heterostructures. Even in the absence of such model, the results demonstrate (probably for the first time) that (i) a magnetic solitons can be realized in such heterostructures and (ii) that while the solitons may be stabilized or destabilized by spin-orbit torques, they are mainly driven by thermal spin torque. These results may thus open avenues for

energy-efficient and highly nonlinear paradigms in spintronics applications, in particular in magnonics and neuromorphic computing.

Chapter 6

Microwave spectroscopy of a single van-der-Waals based two-magnet microstructure

The two-magnet heterostructure approach presented in the previous chapters has shown an excellent promise for spintronics studies and applications for the following reasons. First, it allows for accessing static and dynamic properties of magnetic materials, that would be otherwise difficult to assess. Second, it allows for tailoring the entire device's magnetic properties in a way that would be impossible if a single magnetic material is used. This also includes tailoring of hybrid spin excitation, such as delocalized spin-wave modes. In this chapter, the idea of two-magnet heterostructures is further developed and applied on a novel exciting class of materials – van der Waals (vdW) two-dimensional (2D) magnetic systems.

6.1 Introduction

Van der Waals's magnetic systems increasingly draw the attention of spintronics research due to their extraordinary properties. The systems typically present 2D magnetism. Due to their layered structure, the exchange interaction is highly anisotropic, and the magnetic moments are usually more strongly coupled within the layers than across the layers. Moreover, the materials can be fabricated in thin films with an integer number of layers.

The van der Waals materials often have a strong intrinsic spin-orbit interaction and therefore, can present with notable magnetic anisotropies and, in the case of conducting materials, with sizeable spin-charge effects. The magnetic anisotropy has the potential to violate the Mermin-Wagner-Berezinskii theorem and thus to allow for magnetic order in these 2D magnetic systems at finite temperatures. The atomic flatness of vdW materials is very conducive to their implementation in the heterostructure. The small volume of a few-layer vdW film requires small total energies for the manipulation of its magnetic states, despite a possibly high magnetic anisotropy that stabilizes the magnetic order. The non-vanishing interaction between the layers allows for a multitude of magnetic states and structures – in a sense domains with (infinitely) sharp domain walls across the layers.

All these properties of van der Waals materials justify efforts [134, 135] to develop efficient methods for studying their magnetic properties and concepts for their implementation in spintronics applications. Here, attention will be given to Iron-Germanium-Tellurium based van der Waals compound (FGT).

FGT van der Waals magnets

The chemical composition of the compound studied here is Fe_3GeTe_2. It shows a layered van der Waals morphology, as shown in figure 6.1a. The magnetic moments carried by Fe atoms are located within layers, which are separated from each other by Te atoms. When deposited onto a substrate, the FGT structure shows an atomically flat surface (see figure 6.1b) with an integer number of layers, that may vary laterally.

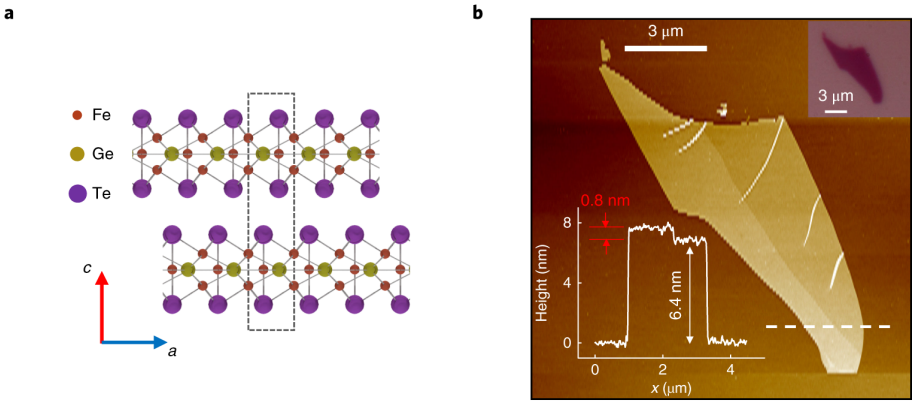

Figure 6.1: (a) Side view of the atomic lattice of FGT. Each colored ball represents iron (red), germanium (yellow), and tellurium (purple). (b) AFM (main) and optical (upper right inset) images of a representative thin FGT flake. Source: Ref. [136].

The system undergoes magnetic phase transitions with varying temperatures, as shown in figure 6.2. As reported by Fei et al. [136], three distinct phases are found: a paramagnetic phase, a single-domain ferromagnetic phase, and a phase with labyrinthine domains. The magnetic moments of iron are subject to a large perpendicular magnetic anisotropy (PMA). A single layer of FGT can be viewed as an Ising type 2D ferromagnet. The magnetic transitions temperatures depend on the number of layers of the magnetic system. The first transition can be detected via hysteresis loops, as shown in Refs. [136, 137]. Moreover, the ferromagnet to paramagnet transition temperature was shown to be tunable

by perpendicular gate voltage [138].

The FGT system is an itinerant magnet. Due to its intrinsic spin-orbit interaction, FGT presents with an anomalous Hall effect, as shown in Ref. [139]. The AHE was used to study the phase transitions; it was found that stochiometry may have a significant critical temperature.

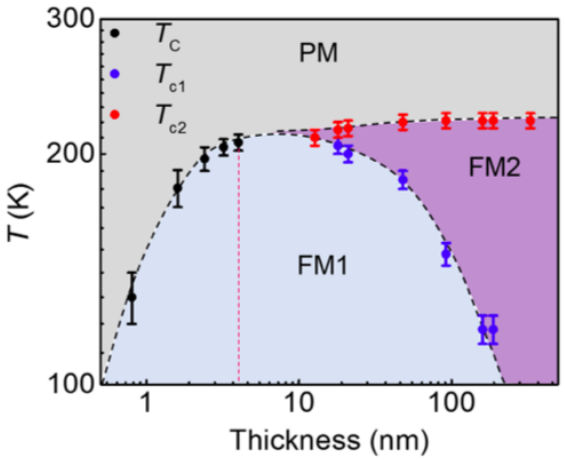

Figure 6.2: The temperature versus thickness of the FGT flake shows the phase diagram. PM expresses the paramagnetic, FM1 is ferromagnetic with a single-domain, and FM2 exhibits labyrinthine domains. Source: Ref. [136].

Wafer-level growth of FGT was shown by Liu et al. [140] with measured charge carrier concentration of 1.2×10^{19} cm^{-3}. Crystals grown by chemical vapor deposition, the carrier concentration was found at 8×10^{13} cm^{-2} [141]. For obtaining high-quality FGT structures; however, the exfoliation method from well-characterized, high-quality, bulk crystals remains the main approach. This is true for many another van der Waals 2D materials.

Therefore, it was set as a goal for this work to develop a method for studying the magnetic properties of 2D based heterostructures that are compatible with the exfoliation

method. The main challenge when exfoliating flakes of 2D material from bulk crystal is that the flake size (e.g., the flake thickness) is challenging to control. Therefore, the experiment must allow for cost-efficiently producing multiple heterostructures for testing serial testing and characterization. Moreover, the lateral size of the flake is typically limited to several tens of microns.

Magnetic heterostructures with such lateral dimensions are typically too small for inductive microwave spectroscopy using cavities and coplanar waveguides. Small lateral dimensions are not a hindrance for microwave spectroscopy using spin-torque ferromagnetic resonance; in particular, FGT is conductive, has an intrinsic spin-charge effect, and is thus well suited for such ST-FMR devices. However, a rather elaborate fabrication of such devices and inevitable variations among them do not allow for direct studies of heterostructure magnetization dynamics. While the fabrication of such devices has commenced at the end of this work, the initial experiments needed to be carried out, resorting to another technique. Such a technique was indeed developed in the course of this work. It involves high-sensitivity planar resonators and custom-designed microscale heterostructures, which can be extended to another 2D van der Waals materials beyond this work, in the future.

Integration of FGT in a two-magnet heterostructure

The approach developed in this work involves the fabrication of microscale YIG/FGT heterostructure, fabrication of planar microresonators, and their consolidation. First, FGT flakes are deposited onto a YIG microdisk. Through a (small) interfacial exchange coupling and dipolar coupling, the magnetization dynamics of YIG and FGT is supposed to hybridize. Similar to two-magnet heterostructures described in previous chapters, investiga-

tions of hybridized magnetization dynamics can allow for studying the magnetic properties of the 2D magnets as well as explore avenues for future spintronics applications. Second, the sensitivity of the planar resonators can be enhanced by increasing the quality factor and the filling factor. The microresonators were proven to perform extraordinarily well with magnetic systems with even nanoscale sizes [88, 142, 143, 144], where this approach was further developed for the studies of YIG/2D heterostructures. However, first, integration of the YIG FGT microstructures with planar microresonators must be accomplished.

6.2 Experimental procedure

YIG micro-disc growth

Since the growth YIG requires a very high annealing temperature, subtractive nano/micro-fabrication methods for patterning YIG films were used in the previous chapters. However, subtractive methods require deposition of resist onto the surface of YIG. Especially after the ion milling procedure, the resist may not entirely be removed, and its residue may contaminate the interface between YIG and FGT. In the course of this work, a lift-off approach to patterning YIG was therefore developed.

First, the GGG substrates were subject to a standard cleaning procedure and then prebaked on a hotplate for 1.5 min at 180 °C to get rid any organic contaminants. Then, using spin coating, positive resist (for electron beam lithography) PMMA was deposited at 3500 rpm for 45 sec. Thre resist was baked on a hotplate for 1.5 min at 180 °C. Then, arrays of circles with a spacing of several millimeters were written using electron beam lithography at a typical dosage of ∼300 (in the NPGS software). Circles with diameters of 150, 100,

50, 25 μm were written. To develop the PMMA resist, a 1:3 volume mix of Methyl isobutyl ketone (MIBK) was applied for approximately 45 sec.

YIG deposition was carried out in Dr. Jing Shi's lab. The substrate was loaded into the pulsed laser deposition (PLD) chamber, which has a base pressure of 4×10^{-7} Torr. The substrate was gradually heated to 450°C in high-purity oxygen with the pressure of 1.5 mTorr with 12 wt.% of ozone. The deposition rate of 1.16 A/min was achieved with a target to substrate distance of 6 cm. YIG layers of 20-30 nm thickness, were deposited. After deposition, the YIG films were soaked in acetone for at least 30 min to remove the PMMA in a lift-off procedure. The YIG micro-disks on GGG were then annealed at 850°C for 200 sec using rapid thermal annealing (RTA) with the flow of pure oxygen. High-quality structures of YIG disks were so obtained, as shown in figure 6.3. As demonstrated further below, the lift-off procedure with the post-annealing process did not deteriorate the magnetic properties of YIG and thus provided a basis for further fabrication steps.

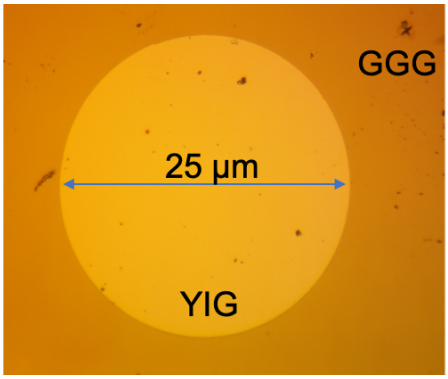

Figure 6.3: Optical image of a YIG micro-disks of thickness 20 nm.

FGT transfer on YIG

After the YIG microdisks are fabricated, FGT flakes are exfoliated onto them, which was done through the support of Dr. Jing Shi's group. The FGT flakes were exfoliated from a pre-characterized bulk crystal provided by Dr. Boniface Fokwa's group. A pickup-transfer optical microscope was used at the SMALL shared facility at MSE building; the result is shown in figure 6.4. A significant fraction of the YIG was covered by an FGT flake with a thickness of approximately 50 nm. Experimental data, shown further below, demonstrate that the proposed technique works with even smaller YIG disks. YIG/FGT microstructures with smaller lateral dimensions and full coverage of the YIG disks can, therefore, be realistically fabricated and measured.

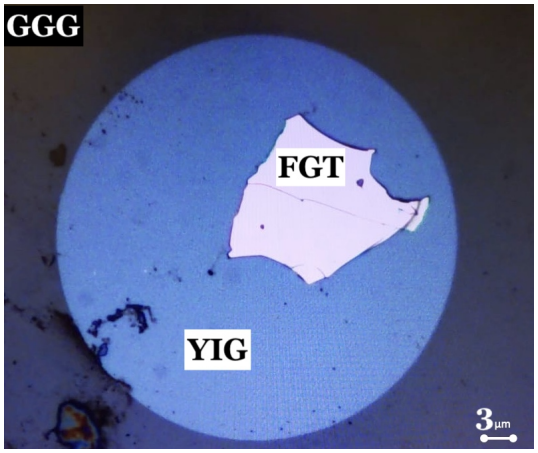

Figure 6.4: The YIG micro-disks and FGT flake.

Integration of YIG/FGT with Ω-shaped microresonators

The first approach to integrating the YIG/FGT microstructures with planar microresonators used in this work followed the pre-established procedures with other magnetic materials from the literature. It relied on fabricating the YIG disk and the microresonator

onto the same substrate. Two possible methods were considered: The first would involve the first fabrication of the YIG disk (including its annealing), then fabrication of the planar resonator around the disk, and finally exfoliation of FGT. This method was dismissed, as it would lead to contamination of the YIG surface in the resonator fabrication process.

The second method that was attempted and is described here involves the fabrication of the microresonator onto the GGG substrate. It is followed by the fabrication of the YIG disk inside the active area of the resonator, using electron beam lithography and lift-off procedure. After the annealing, the FGT deposition is be carried out.

As figure 6.5 demonstrates, these fabrication steps can be successfully carried out. However, it was found that the annealing procedure leads to the electrical deterioration of the microresonator. While structurally no significant changes occur, the metallization of the microresonator is modified in the annealing step in that it becomes resistive. The increased resistivity of the microresonator negatively impacts its qualify factor, and thus its performance. Better suitable alternatives had to be conceived, therefore.

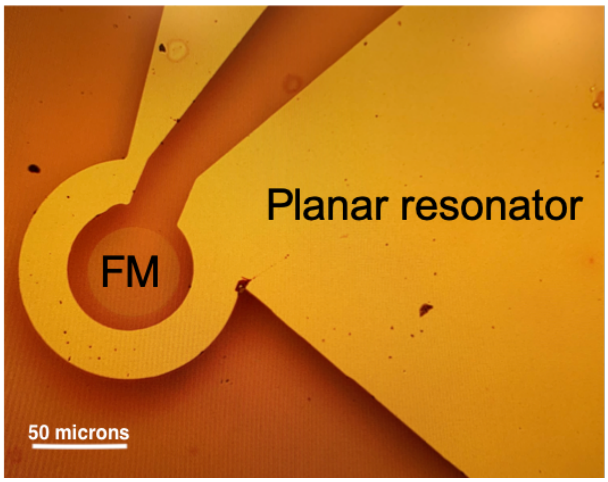

Figure 6.5: The YIG micro-disks inside the Ω-shaped planar resonator micro-coil before the thermal annealing.

The two-chip approach

The alternative was found in fabricating the YIG/FGT microstructure and the microresonator on different chips. By flipping one of the substrates over, the two chip are positioned such that the YIG/FGT microstructure is located within the plantar resonator's micro-coil, as shown in figure 6.6. This procedure is monitors using an optical microscope and has been carried out in this work manually multiple times, which is very time consuming and tedious. However, this two-chip approach has proven to be extremely effective for conducting microwave spectroscopy on a variety of magnetic systems. Although the idea is relatively straightforward, it was not (or at least not widely) considered in the research community. The two-chip approach can be supported by developing a rather simple lateral positioning system because of its benefits.

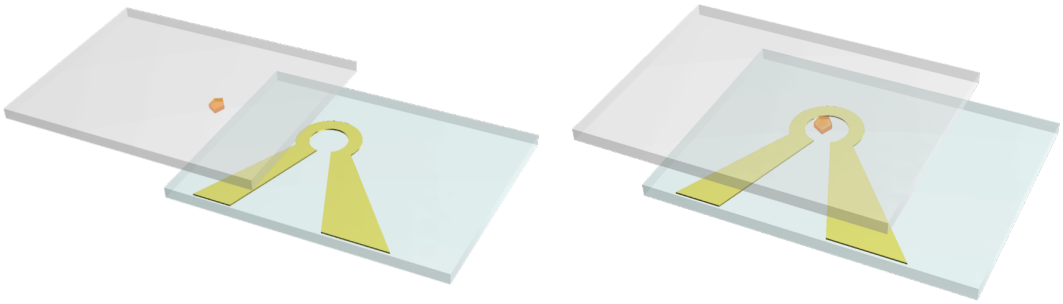

(a) Step 1 **(b)** Step 2

Figure 6.6: The flip-chip or two-chip approach

The two-chip approach allows for reusing the microresonators and therefore streamlines the serial characterization of magnetic systems. For positioning the chips above each other, one of the chips must be transparent to allow for optical monitoring of the alignment. Typically the microresonator chip is first fixed in a microwave circuit holder and connected

to a coplanar waveguide. It is possible to fabricate the microresonators on a transparent substrate and keep this on the top during the alignment procedure; however, this alternative is less time-efficient.

Instead, YIG disks can be grown on transparent substrates. The GGG material is already optically transparent; however, the two-side polished substrate must be used. The fabrication procedure of the YIG/FGT involves otherwise the same steps [145] as described above. The resulting two-ship device is shown in figure 6.7. The microresonator was fabricated on (Al_2O_3) transparent sapphire substrate using a photomask and photolithography. The resonator design, as described in chapter 3, consists of an Ω - shaped micro-coil, stripline, and two large stubs (sidearms). The YIG/FGT microstructure can be places wither in the center of the micro-coil or at its edge, which affects the symmetry of the microwave magnetic field and the detection sensitivity.

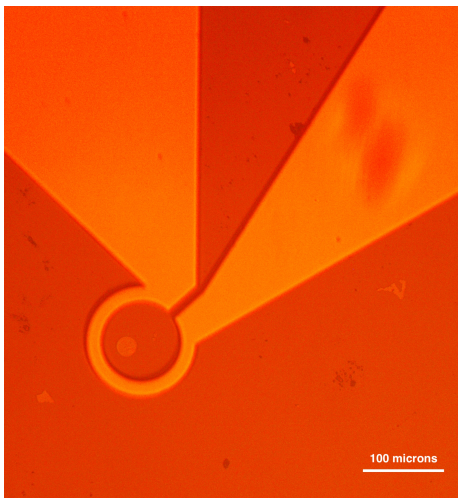

Figure 6.7: An optical image of a YIG/FGT microstructure and a microresonator that were integrated using the two-chip approach. Here, both substrates are are transparent.

Microwave spectroscopy

The microresonators fabricated in this work were characterized using the experimental setup sketched in figure 6.8. A microwave signal is sent through a directional coupler into the microresonator. The signal is partially reflected and diverted via the directional coupler into a microwave diode. The reflected signal is minimized when the microwave frequency matches the natural (eigen-)frequency of the microresonator. It was found that several eigenmodes of the resonator exist with typical frequencies of 1.8 GHz, 3.6 GHz, 7.9 GHz, and 14.1 GHz.

As shown further below, the natural frequency of 7.9 GHz has the best efficiency for FMR spectroscopy (highest FMR signal). However, the existence of other modes is rather beneficial for the experiment, because it allows for FMR measurements at various frequencies even if at reduced efficiency. According to Ref. [88], the sensitivity of the microresonator may pushed to 2.3×10^9 spins $G^{-1}Hz^{-1/2}$ at 300 K. However, the exact sensitivity and the eigenfrequency values may differ from device to device.

The two-chip device was placed into the microwave circuitry and inserted into the helium-flow cryostat. The devices have proven to be cryogen compatible and mechanically stable, no significant variations of the resonator performance of the FMR signal were observed. Ferromagnetic resonance measurements were carried out in the field-domain using field modulation. The data were obtained for various temperatures and angles of the external magnetic field with respect to the sample plane.

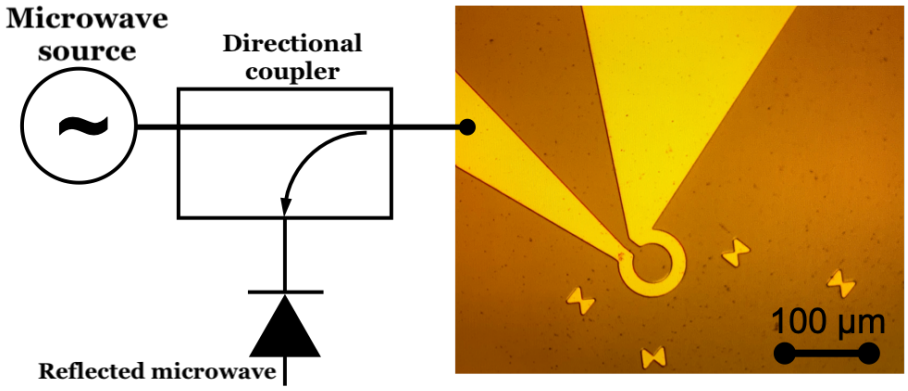

Figure 6.8: Sketch of the microwave circuitry used for characterization of the microresonators and for ferromagnetic resonance on two-chip devices.

6.3 Results and discussion

First, frequency-dependent FMR measurements were performed a bare YIG thin film at room temperature with a magnetic field applied in the sample plane. Figure 6.9a shows the demodulated signal at the microwave diode as a function of field and frequency. The signal is observed over a large range of microwave frequencies, which proves that the microresonators can be used for broad-band studies. The quantitative evaluation of the FMR amplitude is shown in figure 6.9b. The amplitude shows a dramatic enhancement in the frequency range of 7 to 9 GHz, which corresponds to the main eigenfrequency of the microresonator. Estimating the amplitudes demonstrates that FMR measurements with these microresonators can be carried out on smaller samples in a broad frequency range and on drastically smaller samples in the frequency range close to the resonator's eigenfrequency.

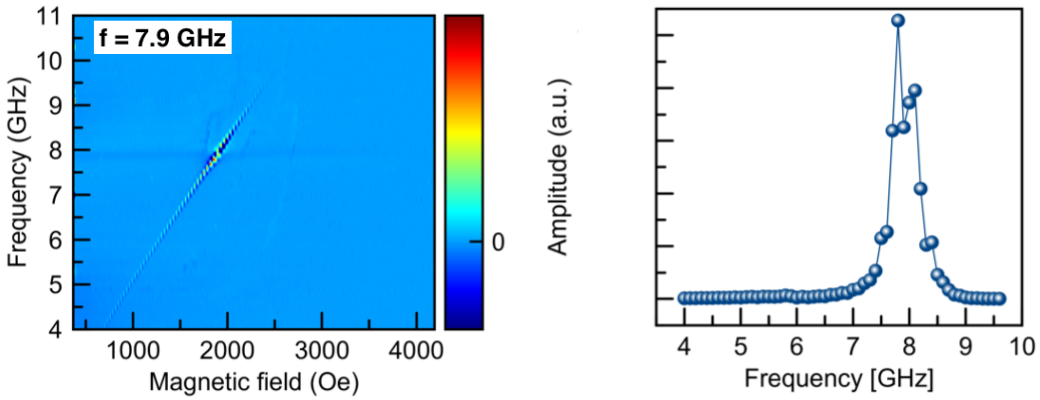

(a) Frequency vs. Magnetic field **(b)** Amplitude vs. Frequency

Figure 6.9: The FMR characterization of a YIG thin film using Ω-shaped planar microresonator.

Frequency-field FMR data were obtained at room temperature as well as at 77 K for out-of-plane configuration. The evaluation is shown in figure 6.10a. The resonance frequency as a function of field, shown in figure 6.10a, can be fitted with the Kittel equation (see chapter 3). It was confirmed that the YIG disk presents with magnetic parameters similar to the expected literature values: the g-factor is 2.01, the effective magnetization is 1903 Oe at room temperature and 2493 Oe at 77 K (see figure 6.10a).

The linewidth shows, as expected, a nearly linear dependence as a function of frequency. Its fit reveals a Gilbert damping constant of 7.8×10^{-4} and the inhomogeneous broadening of 7.812 Oe at room temperature. At 77 K, as expected, the damping and the inhomogeneous broadening increase to $2.4\times\ 10^{-3}$ and 30.7 Oe at 77 K, respectively (see figure 6.10b).

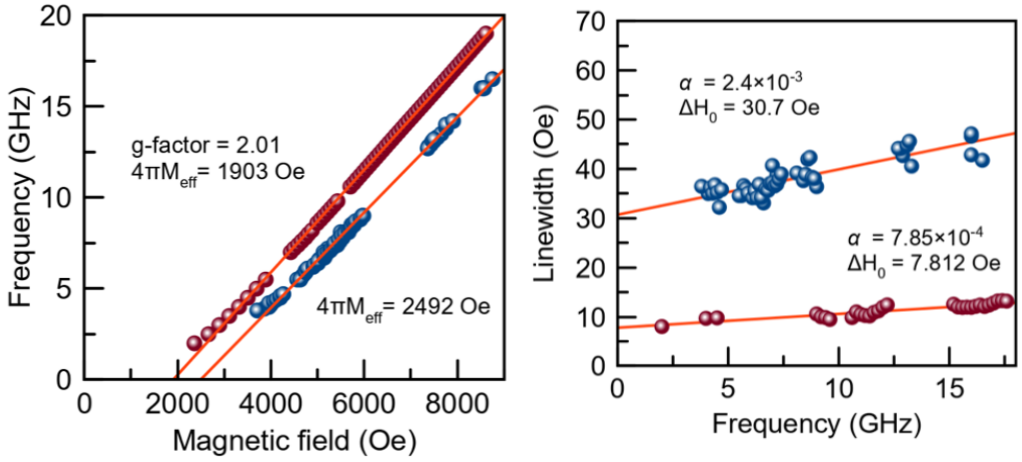

(a) Frequency vs. Magnetic field

(b) Linewidth vs. Frequency

Figure 6.10: Out-of-plane FMR characterization of a bare YIG thin film at room temperature (red) and 77K (blue).

FMR on YIG/FGT heterostructures

Ferromagnetic resonance on YIG/FGT heterostructures shows in general very similar results as those for bare YIG thin film. The spectra seem to originate from the YIG part of the heterostructure. However, significant differences become prominent upon variation of temperature and polar angle of the magnetic field (measured with respect to the film plane).

Figure 6.11 shows a series of FMR spectra on YIG thin film for different angles at 77 K. The resonance field increases with when the magnetic field is rotated from in-plane toward the out-of-plane direction starting from 0° to 65° with 5° steps, which is due to the shape anisotropy of the YIG thin film.

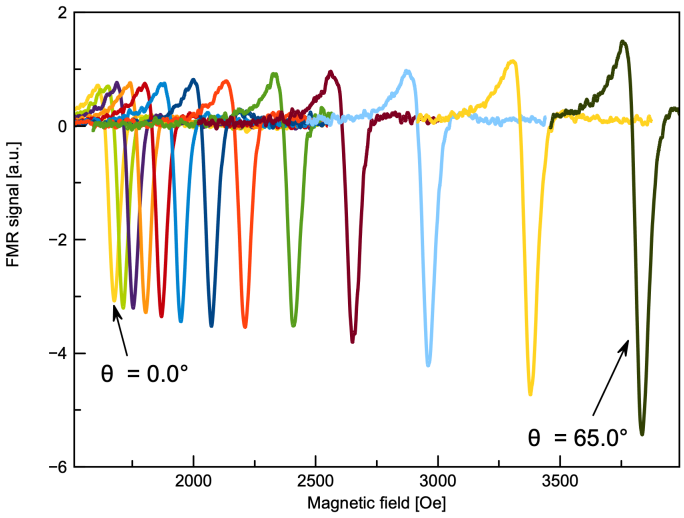

Figure 6.11: Angular dependence of FMR spectra of YIG/FGT at 8.1 GHz at 77 K with 5° steps from 0° to 65° .

The temperature dependence of the ferromagnetic resonance of a YIG thin film also follows the expected behavior. Figure 6.12 shows the spectra as a function of field and temperature, measured at 8.1 GHz at an oblique angle of 70°. The linewidth, evaluated from these spectra, presents a monotonous dependence on the temperature. As expected, the linewidth increases with decreasing temperature, since both the damping and inhomogeneous broadening increase at low temperature.

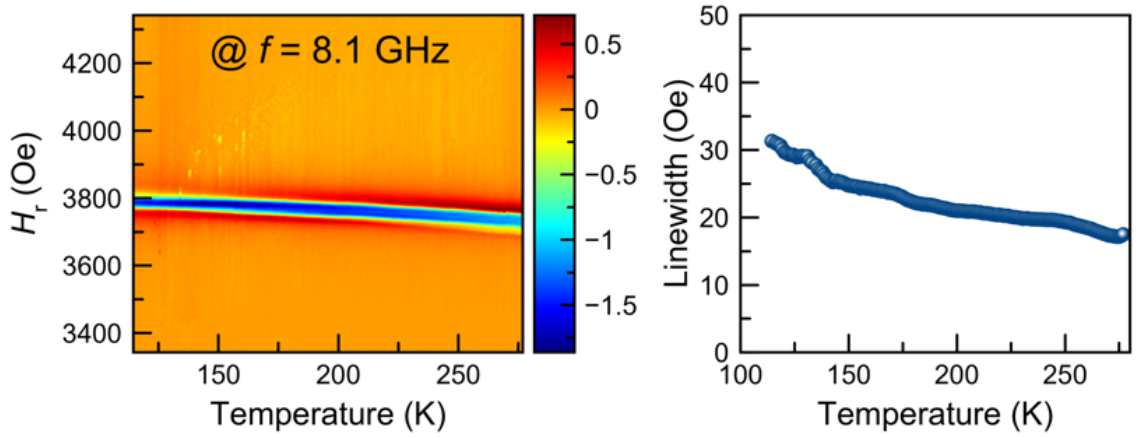

Figure 6.12: FMR on a YIG thin film, and the resonance field and linewidth as a function of temperature at a polar angle of θ=70°.

However, the spectra obtained on YIG/FGT heterostructure show notable anomalies. The resonance field is presented as a function of temperature in figure 6.13a. For the magnetic field applied in the film plane, the resonance field decreases with decreasing temperature, as expected. However, it begins to saturate notably below 130 K. For field angles closer to the out-of-plane direction, such as 75°, the resonance field first increases with decreasing temperature, which again is expected due to the shape anisotropy with temperature-dependent effective magnetization. However, at low temperature, below 100 K, the resonance field drops. These anomalies point towards an additional, temperature-dependent, uniaxial perpendicular magnetic anisotropy. This anisotropy is likely induced in YIG by FGT, which itself is known to possess large perpendicular anisotropy. This anisotropy could be induced in the YIG by proximity with FGT. This picture, however, assumes that magnetization dynamics measured in the FMR experiment originates from the YIG. An alternative interpretation based on the experiences with two-magnet systems de-

scribed in previous chapters is more reasonable: the magnetization dynamics are hybridized across the YIG and FGT layers. Although a theoretical model for such a scenario has not yet been formulated, it is reasonable to assume that the perpendicular magnetic anisotropy in FGT would affect the spectrum as presented in figure 6.13a. A more detailed analysis of the data provides further support for the hypothesis of hybridized magnetic excitations.

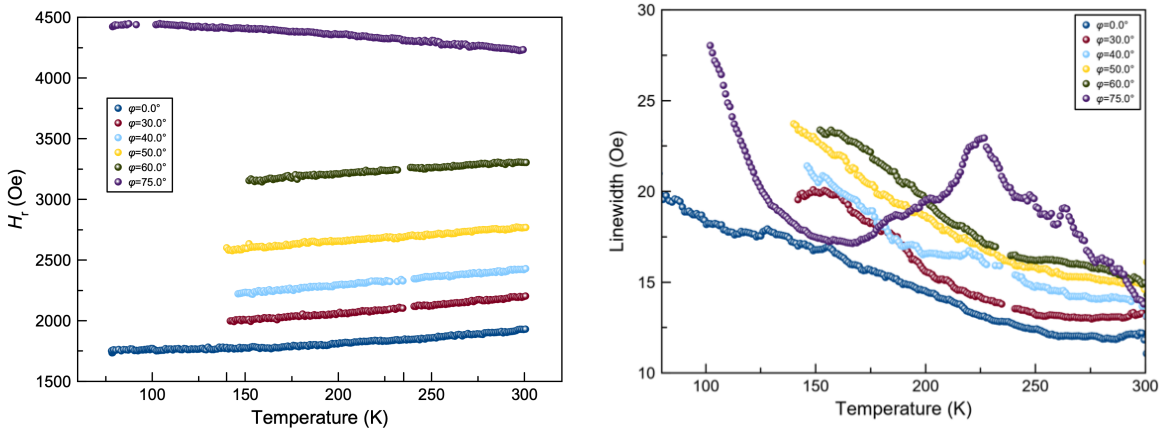

(a) H_r vs. Temperature

(b) Linewidth vs. Temperature

Figure 6.13: FMR on YIG/FGT microstructure. Temperature dependence of resonance field and linewidth for different polar angles of magnetic fields at 8.1 GHz.

In figure , the FMR linewidth is shown as a function of temperature for various polar angles of the magnetic field. Generally, the linewidth presents an increasing trend with decreasing temperature, which is similar to the expected behavior for YIG. However, again, notable anomalies are observed. For some oblique angles, the linewidth suggests non-monotonic behavior near the temperature of 150 K. For large polar angles, approaching the out-of-plane direction, a prominent peak of the linewidth near 220 K emerges. This temperature corresponds to the critical temperature of the FGT material (see figure 6.2).

A closer look at the resonance line shape, as shown in figure for an angle of 70°,

reveals that the signal is dominated by inhomogeneous broadening. As shown in the figure, for some angles, the broadening is significant and allows us to distinguish two distinct FMR contributions. It is reasonable to assume that these two contributions originate from the uncovered YIG and YIG area that is covered with FGT (see figure 6.4).

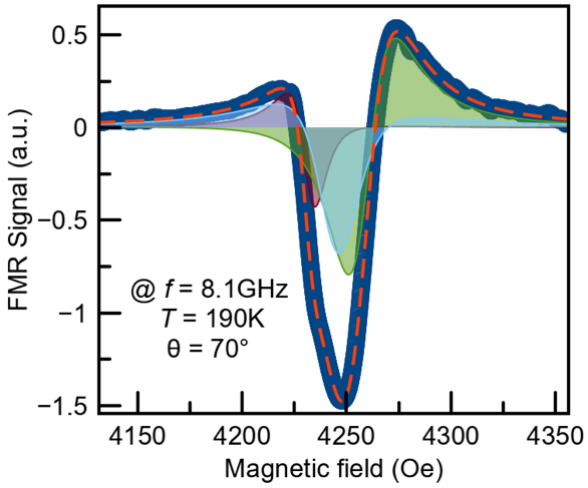

Figure 6.14: The FMR signal of YIG/FGT at 8.1 GHz, temperature of 190 K, and polar angle of 70°.

The significant increase of the linewidth near 220 K is, however, unlikely to originate from a proximity anisotropy in YIG due to FGT. At the temperature of 220 K, no particular variation of the induced anisotropy can be expected. However, spin fluctuations in FGT may increase near the transition temperatures. Indeed, Yi et al. in Ref. [146] studied low-frequency AC magnetic susceptibility of FGT. As shown in figure 6.15, the dispersive and dissipative susceptibility increase dramatically near the transition temperatures of ∼150 K, and ∼220 K. The amplitude of these spikes depends on the mutual orientation of the AC magnetic field and the 2D layer normal vector. The authors identified the temperature regions, separated by critical temperatures, as an antiferromagnetic (AFM) phase,

a mixed antiferromagnetic/ferromagnetic (AFM+FM) phase, and a paramagnetic phase (PM). This interpretation of the results is not in line with the results by Fei et al. [136], shown in figure 6.2. This contradiction may require further discussion; however, it is unambiguous that the phase transitions exist and that critical spin fluctuations occur near the transition temperatures.

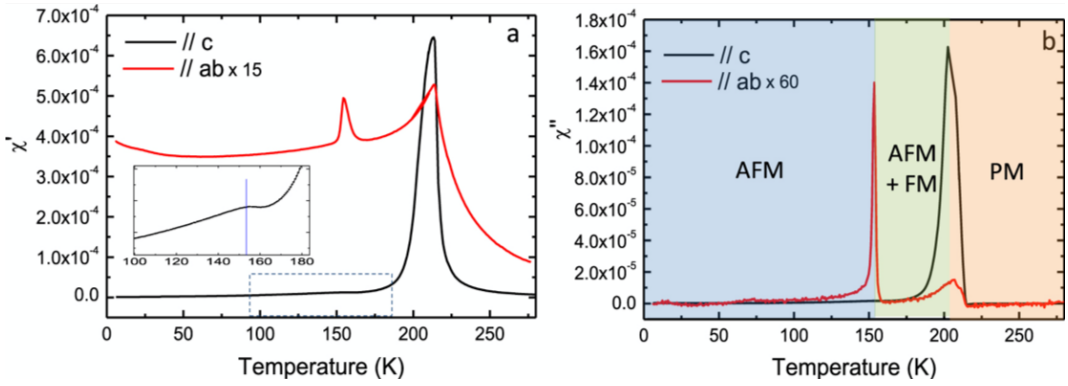

Figure 6.15: The real part (a) and the imaginary part (b) of the temperature dependent AC susceptibility of the FGT. Source: Ref. [146].

By adjusting the polar angle of the magnetic field, multiple FMR measurements were carried out, and the linewidth was evaluated by fitting the inhomogeneous line shape to a single spectroscopic response function. This procedure bears some inaccuracy because the line shape indicates two distinct contributions; however, evaluation of the data by fitting it to two spectroscopic functions would result in larger inaccuracy due to a significant overlap of the contributions. Figure 6.16 shows the linewidth as a function of temperature for two polar angles. It is evident that the linewidth spikes near the critical temperature of 220 K. Furthermore, for $\theta = 74°$ a small spike near the critical temperature of ~ 150 K is observed.

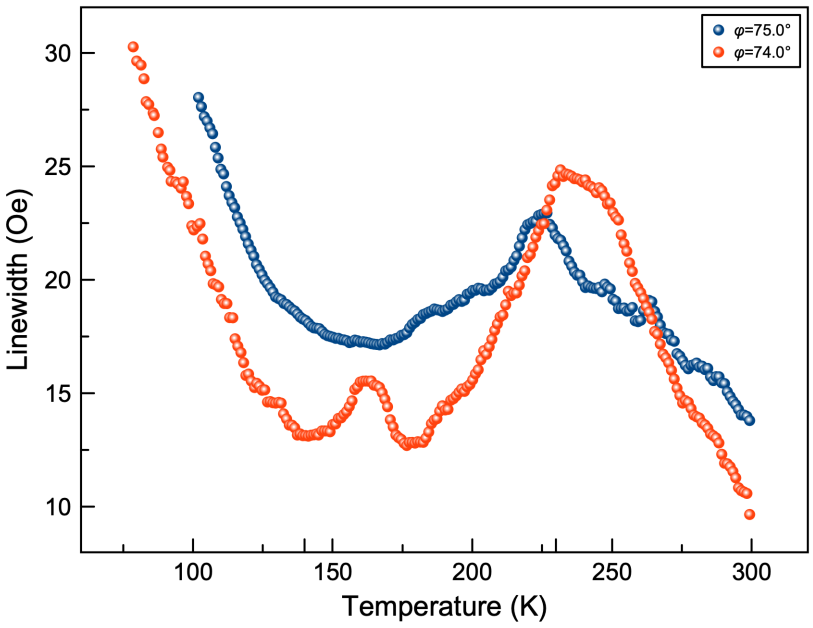

Figure 6.16: The linewidth versus temperature of YIG/FGT at angles θ=74° and θ=75°.

The data allows for an interpretation as follows: the apparent linewidth is dominated by inhomogeneity. The inhomogeneity has two major contributions originating from bare YIG and YIG/FGT heterostructure. Since the areas of covered and uncovered YIG are in the micrometer range, their spin dynamics are largely independent of each other, i.e., and there is no lateral hybridization. The apparent resonance field indicates a slight variation of the proximity induced effective anisotropy, increasing at low temperatures. The increases of the apparent linewidth indicate a more dramatic effect, occurring near the critical temperatures of FGT. The critical spin fluctuations of FGT couple to magnetization dynamics of YIG, resulting in a hybridization of the spin waves across the spin subsystems of YIG and FGT, where the latter is near a critical point. A very rough estimate of the coupling strength is 0.03 MHz at this oblique angle. The microscopic mechanisms of the

coupling cannot be deduced from the data: both dipolar coupling and interfacial exchange interaction are possible.

6.4 Conclusions and Outlook

In this chapter, an experimental technique was developed and presented to study spin excitations in microscale magnetic heterostructures. An experimental approach was developed for fabricating microscale heterostructures incorporating YIG and van der Waals materials. Ferromagnetic resonance measurements were successfully carried out, varying temperature and polar angle of the magnetic field. Indications for proximity induced low-temperature magnetic anisotropy were found. Moreover, hybridization of YIG spin waves with critical spin fluctuations in FGT near phase transition was observed.

Based on the results, following conclusions for further development of the presented research direction can be made: The measurements need to be carried out at larger polar angles, closer to the out-of-plane direction. This angle was so far limited because of the maximum field achievable in the experiment. The options are a modification of the magnet to reach higher fields or design the planar microresonators with lower natural frequencies allowing for lower FMR fields in the perpendicular geometry. Furthermore, measurements are lower temperature need to be carried out to investigate the proximity induced magnetic anisotropy. To improve the accuracy of the results, smaller YIG microdisks need to be designed and fabricated, which would allow for complete coverage of YIG with the 2D materials. The presented results indicate that the sensitivity of the spectroscopy technique is sufficient for further miniaturization. Moreover, the definition of electrical contacts on

the FGT would allow for electrical detection of spin excitations in the FGT spin subsystem, to be measured in parallel with the inductive FMR described here. Finally, the range of materials for the ferromagnet/2D-vdW heterostructures should be extended. On the one hand, the ferromagnetic materials could be chosen to be metallic, which is likely to increase the interfacial coupling between the ferromagnet and the 2D layer. On the other hand, other 2D materials could be explored, resorting to the two-magnet paradigm presented here.

Chapter 7

Summary

In the course of this work, the focus was set on exploring the novel spin physics of two-magnet heterostructures and their potential benefits for future spintronics applications. While various two-magnet heterostructures are potentially possible, here, the most pressing idea of combining a magnetic insulator with a magnetic conductor was pursued.

This work's main achievements include observation of physical phenomena that have substantial potential for spintronics applications. In YIG/Py systems, an increase in the effective spin-charge effect was reached. A spin torque oscillator that is thermally driven and thus most energy-efficient was realized in such heterostructure nano-devices. From the theoretical point of view, hybridization of spin waves across the layers of the heterostructure and their thermally driven condensation present a novel critical phenomenon in the magnon thermodynamics and will hopefully motivate further theoretical efforts. Magnetic solitons were observed in the YIG/Py nanowires, which is a highly intriguing phenomenon. First, the results may present the first realization of solitonic auto-oscillatory modes in such

systems with hybridized spin-wave spectra. On the other hand, the results may present the first realization of a dynamic soliton driven by thermal spin torque. Furthermore, the preliminary data on spin-orbit stabilization may also contribute to the novel field of spin-orbitronics and provide a useful tool for future spintronics applications. The translation of the two-magnet paradigm and the related knowledge, acquired in this work, to heterostructures with 2D magnets brings potential benefits for advancing spintronics. The two-magnet approach allows for exploring 2D magnet's spin physics via its interaction with the spin subsystem of the conventional magnet. Moreover, as the hybridization of the YIG spin-wave modes with 2D critical spin fluctuations shows, such hybridization of spin excitation in FM/2D heterostructures may provide a critical tool for engineering the spin physics in this emergent family of magnetic materials. Besides such fundamental aspects of spin physics, experimental methods of spin-wave spectroscopy were advanced and developed in this work, which will hopefully be helpful for spintronics research at UCR and beyond.

Bibliography

[1] Igor Žutić, Jaroslav Fabian, and S Das Sarma. Spintronics: Fundamentals and applications. *Reviews of modern physics*, 76(2):323, 2004.

[2] Zihui Wang, Yiyan Sun, Mingzhong Wu, Vasil Tiberkevich, and Andrei Slavin. Control of spin waves in a thin film ferromagnetic insulator through interfacial spin scattering. *Physical review letters*, 107(14):146602, 2011.

[3] Andrew D Kent and Daniel C Worledge. A new spin on magnetic memories. *Nature nanotechnology*, 10(3):187, 2015.

[4] H-S Philip Wong and Sayeef Salahuddin. Memory leads the way to better computing. *Nature nanotechnology*, 10(3):191, 2015.

[5] D Houssameddine, U Ebels, B Delaët, B Rodmacq, I Firastrau, F Ponthenier, M Brunet, C Thirion, J-P Michel, L Prejbeanu-Buda, et al. Spin-torque oscillator using a perpendicular polarizer and a planar free layer. *Nature materials*, 6(6): 447–453, 2007.

[6] Andrei Slavin and Vasil Tiberkevich. Nonlinear auto-oscillator theory of microwave generation by spin-polarized current. *IEEE Transactions on Magnetics*, 45(4):1875–1918, 2009.

[7] Ikuya Tagawa, Masato Shiimoto, Masato Matsubara, Shuya Nosaki, Yosuke Urakami, and Jun Aoyama. Advantage of mamr read-write performance. *IEEE Transactions on Magnetics*, 52(9):1–4, 2016.

[8] Vladislav E Demidov, Sergei Urazhdin, and Sergej O Demokritov. Direct observation and mapping of spin waves emitted by spin-torque nano-oscillators. *Nature materials*, 9(12):984–988, 2010.

[9] S Urazhdin, VE Demidov, H Ulrichs, T Kendziorczyk, T Kuhn, J Leuthold, G Wilde,

and SO Demokritov. Nanomagnonic devices based on the spin-transfer torque. *Nature nanotechnology*, 9(7):509, 2014.

[10] Andrii V Chumak, Vitaliy I Vasyuchka, Alexander A Serga, and Burkard Hillebrands. Magnon spintronics. *Nature Physics*, 11(6):453–461, 2015.

[11] Julie Grollier, Damien Querlioz, and Mark D Stiles. Spintronic nanodevices for bioinspired computing. *Proceedings of the IEEE*, 104(10):2024–2039, 2016.

[12] Alice Mizrahi, Nicolas Locatelli, Romain Lebrun, Vincent Cros, Akio Fukushima, Hitoshi Kubota, Shinji Yuasa, Damien Querlioz, and Julie Grollier. Controlling the phase locking of stochastic magnetic bits for ultra-low power computation. *Scientific reports*, 6(1):1–7, 2016.

[13] Nicolas Locatelli, Vincent Cros, and Julie Grollier. Spin-torque building blocks. *Nature materials*, 13(1):11–20, 2014.

[14] SSP Parkin, ZG Li, and David J Smith. Giant magnetoresistance in antiferromagnetic co/cu multilayers. *Applied Physics Letters*, 58(23):2710–2712, 1991.

[15] LALE Landau and Evgeny Lifshitz. On the theory of the dispersion of magnetic permeability in ferromagnetic bodies. In *Perspectives in Theoretical Physics*, pages 51–65. Elsevier, 1992.

[16] Thomas L Gilbert. A phenomenological theory of damping in ferromagnetic materials. *IEEE transactions on magnetics*, 40(6):3443–3449, 2004.

[17] Alexander Markov. Modeling of emerging resistive switching based memory cells. 2014.

[18] John C Slonczewski et al. Current-driven excitation of magnetic multilayers. *Journal of Magnetism and Magnetic Materials*, 159(1):L1, 1996.

[19] Z Li and Shufeng Zhang. Magnetization dynamics with a spin-transfer torque. *Physical Review B*, 68(2):024404, 2003.

[20] Mizukami Lab. *Spin transfer switching*, (accessed May 6, 2020). `https://www.wpi-aimr.tohoku.ac.jp/mizukami_lab/spintorque.htm`.

[21] M Tsoi, AGM Jansen, J Bass, W-C Chiang, V Tsoi, and P Wyder. Generation and detection of phase-coherent current-driven magnons in magnetic multilayers. *Nature*, 406(6791):46–48, 2000.

[22] S Il Kiselev, JC Sankey, IN Krivorotov, NC Emley, RJ Schoelkopf, RA Buhrman, and DC Ralph. Microwave oscillations of a nanomagnet driven by a spin-polarized current. *nature*, 425(6956):380–383, 2003.

[23] Daniel C Ralph and Mark D Stiles. Spin transfer torques. *Journal of Magnetism and Magnetic Materials*, 320(7):1190–1216, 2008.

[24] CL Chien and CR Westgate. inthe hall effect and its applications, edited by plenum press. *New York*, 1980.

[25] Hongming Weng, Xi Dai, and Zhong Fang. From anomalous hall effect to the quantum anomalous hall effect. *arXiv preprint arXiv:1509.05507*, 2015.

[26] Robert Karplus and JM Luttinger. Hall effect in ferromagnetics. *Physical Review*, 95 (5):1154, 1954.

[27] NA Sinitsyn. Semiclassical theories of the anomalous hall effect. *Journal of Physics: Condensed Matter*, 20(2):023201, 2007.

[28] Naoto Nagaosa, Jairo Sinova, Shigeki Onoda, Allan H MacDonald, and Nai Phuan Ong. Anomalous hall effect. *Reviews of modern physics*, 82(2):1539, 2010.

[29] William Thomson. Xix. on the electro-dynamic qualities of metals:—effects of magnetization on the electric conductivity of nickel and of iron. *Proceedings of the Royal Society of London*, (8):546–550, 1857.

[30] T McGuire and RL Potter. Anisotropic magnetoresistance in ferromagnetic 3d alloys. *IEEE Transactions on Magnetics*, 11(4):1018–1038, 1975.

[31] J Holanda, DS Maior, A Azevedo, and SM Rezende. Anisotropic magnetoresistance and anomalous nernst effect in exchange biased permalloy/(1 0 0) nio single-crystal. *Journal of Magnetism and Magnetic Materials*, 432:507–510, 2017.

[32] Vladislav Mor, Asaf Grosz, and Lior Klein. Planar hall effect (phe) magnetometers. In *High Sensitivity Magnetometers*, pages 201–224. Springer, 2017.

[33] A Manchon and Shufeng Zhang. Theory of nonequilibrium intrinsic spin torque in a single nanomagnet. *Physical Review B*, 78(21):212405, 2008.

[34] Rajagopalan Ramaswamy, Jong Min Lee, Kaiming Cai, and Hyunsoo Yang. Recent advances in spin-orbit torques: Moving towards device applications. *Applied Physics Reviews*, 5(3):031107, 2018.

[35] JE Hirsch. Spin hall effect. *Physical Review Letters*, 83(9):1834, 1999.

[36] Yuichiro K Kato, Roberto C Myers, Arthur C Gossard, and David D Awschalom. Observation of the spin hall effect in semiconductors. *science*, 306(5703):1910–1913, 2004.

[37] Yan-Ting Chen, Saburo Takahashi, Hiroyasu Nakayama, Matthias Althammer, Sebastian TB Goennenwein, Eiji Saitoh, and Gerrit EW Bauer. Theory of spin hall magnetoresistance. *Physical Review B*, 87(14):144411, 2013.

[38] E Saitoh, M Ueda, H Miyajima, and G Tatara. Conversion of spin current into charge current at room temperature: Inverse spin-hall effect. *Applied physics letters*, 88(18): 182509, 2006.

[39] Ken-ichi Uchida, Hiroto Adachi, Takeru Ota, Hiroyasu Nakayama, Sadamichi Maekawa, and Eiji Saitoh. Observation of longitudinal spin-seebeck effect in magnetic insulators. *Applied Physics Letters*, 97(17):172505, 2010.

[40] Mikhail I Dyakonov and VI Perel. Current-induced spin orientation of electrons in semiconductors. *Physics Letters A*, 35(6):459–460, 1971.

[41] MI D'yakonov and VI Perel. Possibility of orienting electron spins with current. *Soviet Journal of Experimental and Theoretical Physics Letters*, 13:467, 1971.

[42] Jairo Sinova, Sergio O Valenzuela, and J Wunderlich. C.? h. back, and t. jungwirth. *Rev. Mod. Phys*, 87:1213, 2015.

[43] HL Wang, CH Du, Y Pu, R Adur, Peter Christopher Hammel, and FY Yang. Scaling of spin hall angle in 3d, 4d, and 5d metals from y 3 fe 5 o 12/metal spin pumping. *Physical review letters*, 112(19):197201, 2014.

[44] Luqiao Liu, Chi-Feng Pai, Y Li, HW Tseng, DC Ralph, and RA Buhrman. Spin-

torque switching with the giant spin hall effect of tantalum. *Science*, 336(6081): 555–558, 2012.

[45] Vladislav E Demidov, Sergei Urazhdin, Henning Ulrichs, Vasyl Tiberkevich, Andrei Slavin, Dietmar Baither, Guido Schmitz, and Sergej O Demokritov. Magnetic nano-oscillator driven by pure spin current. *Nature materials*, 11(12):1028–1031, 2012.

[46] Zheng Duan, Andrew Smith, Liu Yang, Brian Youngblood, Jürgen Lindner, Vladislav E Demidov, Sergej O Demokritov, and Ilya N Krivorotov. Nanowire spin torque oscillator driven by spin orbit torques. *Nature communications*, 5(1):1–7, 2014.

[47] Martin Collet, Xavier De Milly, O d'Allivy Kelly, Vladimir V Naletov, Rozenn Bernard, Paolo Bortolotti, J Ben Youssef, VE Demidov, SO Demokritov, JL Prieto, et al. Generation of coherent spin-wave modes in yttrium iron garnet microdiscs by spin–orbit torque. *Nature communications*, 7(1):1–8, 2016.

[48] A Brataas, Yaroslav Tserkovnyak, GEW Bauer, and Paul J Kelly. Spin pumping and spin transfer. *Spin current*, 17:87–135, 2012.

[49] Gerrit E Bauer and Yaroslav Tserkovnyak. Spin-magnon transmutation. *Physics*, 4: 40, 2011.

[50] D MacNeill, GM Stiehl, MHD Guimaraes, RA Buhrman, J Park, and DC Ralph. Control of spin–orbit torques through crystal symmetry in wte 2/ferromagnet bilayers. *Nature Physics*, 13(3):300–305, 2017.

[51] Luc Berger. Emission of spin waves by a magnetic multilayer traversed by a current. *Physical Review B*, 54(13):9353, 1996.

[52] Mark D Stiles and A Zangwill. Anatomy of spin-transfer torque. *Physical Review B*, 66(1):014407, 2002.

[53] JA Katine, FJ Albert, RA Buhrman, EB Myers, and DC Ralph. Current-driven magnetization reversal and spin-wave excitations in co/cu/co pillars. *Physical review letters*, 84(14):3149, 2000.

[54] EB Sonin. Spin currents and spin superfluidity. *Advances in Physics*, 59(3):181–255, 2010.

[55] So Takei and Yaroslav Tserkovnyak. Superfluid spin transport through easy-plane ferromagnetic insulators. *Physical review letters*, 112(22):227201, 2014.

[56] So Takei, Yaroslav Tserkovnyak, and Masoud Mohseni. Spin superfluid josephson quantum devices. *Physical Review B*, 95(14):144402, 2017.

[57] Tomohiro Taniguchi, Julie Grollier, and Mark D Stiles. Spin-transfer torques generated by the anomalous hall effect and anisotropic magnetoresistance. *Physical Review Applied*, 3(4):044001, 2015.

[58] Jacob Torrejon, Mathieu Riou, Flavio Abreu Araujo, Sumito Tsunegi, Guru Khalsa, Damien Querlioz, Paolo Bortolotti, Vincent Cros, Kay Yakushiji, Akio Fukushima, et al. Neuromorphic computing with nanoscale spintronic oscillators. *Nature*, 547 (7664):428–431, 2017.

[59] Tomohiro Taniguchi. Magnetoresistance generated from charge-spin conversion by anomalous hall effect in metallic ferromagnetic/nonmagnetic bilayers. *Physical Review B*, 94(17):174440, 2016.

[60] Frances Hellman, Axel Hoffmann, Yaroslav Tserkovnyak, Geoffrey SD Beach, Eric E Fullerton, Chris Leighton, Allan H MacDonald, Daniel C Ralph, Dario A Arena, Hermann A Dürr, et al. Interface-induced phenomena in magnetism. *Reviews of modern physics*, 89(2):025006, 2017.

[61] Jonathan D Gibbons, David MacNeill, Robert A Buhrman, and Daniel C Ralph. Reorientable spin direction for spin current produced by the anomalous hall effect. *Physical Review Applied*, 9(6):064033, 2018.

[62] Alisha M Humphries, Tao Wang, Eric RJ Edwards, Shane R Allen, Justin M Shaw, Hans T Nembach, John Q Xiao, Thomas J Silva, and Xin Fan. Observation of spin-orbit effects with spin rotation symmetry. *Nature communications*, 8(1):1–7, 2017.

[63] Seung-heon C Baek, Vivek P Amin, Young-Wan Oh, Gyungchoon Go, Seung-Jae Lee, MD Stiles, Byong-Guk Park, and Kyung-Jin Lee. Spin-orbit torques induced by interface-generated spin currents. *arXiv preprint arXiv:1708.06864*, 2017.

[64] Arnab Bose, Duc Duong Lam, Swapnil Bhuktare, Sutapa Dutta, Hanuman Singh, Y Jibiki, M Goto, S Miwa, and AA Tulapurkar. Observation of anomalous spin torque generated by a ferromagnet. *Physical Review Applied*, 9(6):064026, 2018.

[65] Scott A Bender and Yaroslav Tserkovnyak. Thermally driven spin torques in layered magnetic insulators. *Physical Review B*, 93(6):064418, 2016.

[66] Chris Safranski, Igor Barsukov, Han Kyu Lee, Tobias Schneider, AA Jara, Andrew Smith, Houchen Chang, Kilian Lenz, Juergen Lindner, Yaroslav Tserkovnyak, et al. Spin caloritronic nano-oscillator. *Nature communications*, 8(1):1–7, 2017.

[67] Hui-Min Tang, Xing-Tao Jia, and Shi-Zhuo Wang. Thermal spin transfer torque in fe| ag| yig multilayers. *Frontiers of Physics*, 12(3):128501, 2017.

[68] J-C Rojas-Sánchez, N Reyren, P Laczkowski, W Savero, J-P Attané, C Deranlot, M Jamet, J-M George, Laurent Vila, and H Jaffrès. Spin pumping and inverse spin hall effect in platinum: the essential role of spin-memory loss at metallic interfaces. *Physical review letters*, 112(10):106602, 2014.

[69] L Landau and E Lifshitz. ron the theory of magnetic permeability in ferro (magnetic bodies, sphysik. *Z. Sowejtunion*, 8:153, 1935.

[70] James HE Griffiths. Anomalous high-frequency resistance of ferromagnetic metals. *Nature*, 158(4019):670–671, 1946.

[71] E Zavoisky. Spin magnetic resonance in the decimetre-wave region. *J. Phys. USSR*, 10:197–198, 1946.

[72] Eric Montoya, Thomas Sebastian, Helmut Schultheiss, Bret Heinrich, Robert E Camley, and Zbigniew Celinski. Magnetization dynamics. In *Handbook of Surface Science*, volume 5, pages 113–167. Elsevier, 2015.

[73] Charles Kittel, Paul McEuen, and Paul McEuen. *Introduction to solid state physics*, volume 8. Wiley New York, 1996.

[74] Charles Kittel. On the theory of ferromagnetic resonance absorption. *Physical review*, 73(2):155, 1948.

[75] I Barsukov, Yu Fu, AM Gonçalves, M Spasova, M Farle, LC Sampaio, RE Arias, and IN Krivorotov. Field-dependent perpendicular magnetic anisotropy in cofeb thin films. *Applied Physics Letters*, 105(15):152403, 2014.

[76] Georg Woltersdorf. *Spin-pumping and two-magnon scattering in magnetic multilayers.*

PhD thesis, Sinon Fraser University, 2004.

[77] M Sparks, R Loudon, and Ch Kittel. Ferromagnetic relaxation. i. theory of the relaxation of the uniform precession and the degenerate spectrum in insulators at low temperatures. *Physical Review*, 122(3):791, 1961.

[78] J Lindner, I Barsukov, C Raeder, C Hassel, O Posth, R Meckenstock, P Landeros, and DL Mills. Two-magnon damping in thin films in case of canted magnetization: Theory versus experiment. *Physical Review B*, 80(22):224421, 2009.

[79] P Landeros, Rodrigo E Arias, and DL Mills. Two magnon scattering in ultrathin ferromagnets: The case where the magnetization is out of plane. *Physical Review B*, 77(21):214405, 2008.

[80] K Lenz, H Wende, W Kuch, K Baberschke, Kálmán Nagy, and András Jánossy. Two-magnon scattering and viscous gilbert damping in ultrathin ferromagnets. *Physical Review B*, 73(14):144424, 2006.

[81] Samuel Holladay. Frequency-swept ferromagnetic resonance characterization of permalloy thin films. 2018.

[82] Luqiao Liu, Takahiro Moriyama, DC Ralph, and RA Buhrman. Spin-torque ferromagnetic resonance induced by the spin hall effect. *Physical review letters*, 106(3): 036601, 2011.

[83] Christopher Safranski. *Fabrication of Nanoscale Spin Torque Oscillator Based on Pt/YIG*. University of California, Irvine, 2018.

[84] IA Campbell. Hall effect and resistivity anisotropy in ni alloys. *Physical Review Letters*, 24(6):269, 1970.

[85] Arne Vansteenkiste and Ben Van de Wiele. Mumax: A new high-performance micromagnetic simulation tool. *Journal of Magnetism and Magnetic Materials*, 323(21): 2585–2591, 2011.

[86] Peng Li Houchen Chang, Wei Zhang, Tao Liu, Axel Hoffmann, Longjiang Deng, and Mingzhong Wu. Nanometer-thick yttrium iron garnet films with extremely low damping.

[87] I Barsukov, Yu Fu, C Safranski, Y-J Chen, B Youngblood, AM Gonçalves, M Spasova, M Farle, JA Katine, CC Kuo, et al. Magnetic phase transitions in ta/cofeb/mgo multilayers. *Applied Physics Letters*, 106(19):192407, 2015.

[88] R Narkowicz, D Suter, and R Stonies. Planar microresonators for epr experiments. *Journal of Magnetic Resonance*, 175(2):275–284, 2005.

[89] Ryszard Narkowicz and Dieter Suter. Tuner and radiation shield for planar electron paramagnetic resonance microresonators. *Review of Scientific Instruments*, 86(2): 024701, 2015.

[90] Can Onur Avci, Andy Quindeau, Chi-Feng Pai, Maxwell Mann, Lucas Caretta, Astera S Tang, Mehmet C Onbasli, Caroline A Ross, and Geoffrey SD Beach. Current-induced switching in a magnetic insulator. *Nature materials*, 16(3):309–314, 2017.

[91] Dmytro A Bozhko, Alexander A Serga, Peter Clausen, Vitaliy I Vasyuchka, Frank Heussner, Gennadii A Melkov, Anna Pomyalov, Victor S L'vov, and Burkard Hillebrands. Supercurrent in a room-temperature bose–einstein magnon condensate. *Nature Physics*, 12(11):1057–1062, 2016.

[92] Fengyuan Yang and P Chris Hammel. Fmr-driven spin pumping in y3fe5o12-based structures. *Journal of Physics D: Applied Physics*, 51(25):253001, 2018.

[93] Jörg Wunderlich. Spintronics: Current-switched magnetic insulator. *Nature materials*, 16(3):284–285, 2017.

[94] Han Kyu Lee, I Barsukov, AG Swartz, B Kim, L Yang, HY Hwang, and IN Krivorotov. Magnetic anisotropy, damping, and interfacial spin transport in pt/lsmo bilayers. *AIP Advances*, 6(5):055212, 2016.

[95] Jairo Sinova, Sergio O Valenzuela, J Wunderlich, CH Back, and T Jungwirth. Spin hall effects. *Reviews of Modern Physics*, 87(4):1213, 2015.

[96] AA Tulapurkar, Y Suzuki, A Fukushima, H Kubota, H Maehara, K Tsunekawa, DD Djayaprawira, N Watanabe, and S Yuasa. Spin-torque diode effect in magnetic tunnel junctions. *Nature*, 438(7066):339–342, 2005.

[97] K Baumgaertl, F Heimbach, S Maendl, D Rueffer, A Fontcuberta i Morral, and D Grundler. Magnetization reversal in individual py and cofeb nanotubes locally probed via anisotropic magnetoresistance and anomalous nernst effect. *Applied*

Physics Letters, 108(13):132408, 2016.

[98] Angie Davidson, Vivek P Amin, Wafa S Aljuaid, Paul M Haney, and Xin Fan. Perspectives of electrically generated spin currents in ferromagnetic materials. *Physics Letters A*, page 126228, 2020.

[99] Vivek P Amin, Jan Zemen, and Mark D Stiles. Interface-generated spin currents. *Physical review letters*, 121(13):136805, 2018.

[100] Kumar Sourav Das, Jing Liu, Bart J van Wees, and Ivan J Vera-Marun. Efficient injection and detection of out-of-plane spins via the anomalous spin hall effect in permalloy nanowires. *Nano letters*, 18(9):5633–5639, 2018.

[101] Christopher Safranski, Eric A Montoya, and Ilya N Krivorotov. Spin–orbit torque driven by a planar hall current. *Nature nanotechnology*, 14(1):27, 2019.

[102] Mohammad Haidar, Ahmad A Awad, Mykola Dvornik, Roman Khymyn, Afshin Houshang, and Johan Åkerman. A single layer spin-orbit torque nano-oscillator. *Nature communications*, 10(1):1–6, 2019.

[103] Sergej O Demokritov, Vladislav E Demidov, Oleksandr Dzyapko, Gennadii A Melkov, Alexandar A Serga, Burkard Hillebrands, and Andrei N Slavin. Bose–einstein condensation of quasi-equilibrium magnons at room temperature under pumping. *Nature*, 443(7110):430–433, 2006.

[104] Tao Liu, Houchen Chang, Vincent Vlaminck, Yiyan Sun, Michael Kabatek, Axel Hoffmann, Longjiang Deng, and Mingzhong Wu. Ferromagnetic resonance of sputtered yttrium iron garnet nanometer films. *Journal of Applied Physics*, 115(17):17A501, 2014.

[105] Volker Sluka, Tobias Schneider, Rodolfo A Gallardo, Attila Kákay, Markus Weigand, Tobias Warnatz, Roland Mattheis, Alejandro Roldán-Molina, Pedro Landeros, Vasil Tiberkevich, et al. Emission and propagation of 1d and 2d spin waves with nanoscale wavelengths in anisotropic spin textures. *Nature nanotechnology*, 14(4):328–333, 2019.

[106] K An, VS Bhat, M Mruczkiewicz, C Dubs, and D Grundler. Optimization of spin-wave propagation with enhanced group velocities by exchange-coupled ferrimagnet-ferromagnet bilayers. *Physical Review Applied*, 11(3):034065, 2019.

[107] Chuanpu Liu, Jilei Chen, Tao Liu, Florian Heimbach, Haiming Yu, Yang Xiao, Jun-

feng Hu, Mengchao Liu, Houchen Chang, Tobias Stueckler, et al. Long-distance propagation of short-wavelength spin waves. *Nature communications*, 9(1):1–8, 2018.

[108] JF Cochran, B Heinrich, and AS Arrott. Ferromagnetic resonance in a system composed of a ferromagnetic substrate and an exchange-coupled thin ferromagnetic overlayer. *Physical Review B*, 34(11):7788, 1986.

[109] Josep Nogués and Ivan K Schuller. Exchange bias. *Journal of Magnetism and Magnetic Materials*, 192(2):203–232, 1999.

[110] Stefan Klingler, Vivek Amin, Stephan Geprägs, Kathrin Ganzhorn, Hannes Maier-Flaig, Matthias Althammer, Hans Huebl, Rudolf Gross, Robert D McMichael, Mark D Stiles, et al. Spin-torque excitation of perpendicular standing spin waves in coupled yig/co heterostructures. *Physical review letters*, 120(12):127201, 2018.

[111] Jilei Chen, Chuanpu Liu, Tao Liu, Yang Xiao, Ke Xia, Gerrit EW Bauer, Mingzhong Wu, and Haiming Yu. Strong interlayer magnon-magnon coupling in magnetic metal-insulator hybrid nanostructures. *Physical review letters*, 120(21):217202, 2018.

[112] AM Gonçalves, I Barsukov, Y-J Chen, L Yang, JA Katine, and IN Krivorotov. Spin torque ferromagnetic resonance with magnetic field modulation. *Applied Physics Letters*, 103(17):172406, 2013.

[113] Arne Vansteenkiste, Jonathan Leliaert, Mykola Dvornik, Mathias Helsen, Felipe Garcia-Sanchez, and Bartel Van Waeyenberge. The design and verification of mumax3. *AIP advances*, 4(10):107133, 2014.

[114] Zheng Duan, Ilya N Krivorotov, Rodrigo E Arias, Nathalie Reckers, Sven Stienen, and Jürgen Lindner. Spin wave eigenmodes in transversely magnetized thin film ferromagnetic wires. *Physical Review B*, 92(10):104424, 2015.

[115] Angie Davidson, Vivek P Amin, Wafa S Aljuaid, Paul M Haney, and Xin Fan. Perspectives of electrically generated spin currents in ferromagnetic materials. *Physics Letters A*, page 126228, 2020.

[116] Yuichi Ohnuma, Hiroto Adachi, Eiji Saitoh, and Sadamichi Maekawa. Magnon instability driven by heat current in magnetic bilayers. *Physical Review B*, 92(22):224404, 2015.

[117] Scott A Bender, Rembert A Duine, Arne Brataas, and Yaroslav Tserkovnyak. Dy-

namic phase diagram of dc-pumped magnon condensates. *Physical Review B*, 90(9): 094409, 2014.

[118] Lei Lu, Yiyan Sun, Michael Jantz, and Mingzhong Wu. Control of ferromagnetic relaxation in magnetic thin films through thermally induced interfacial spin transfer. *Physical review letters*, 108(25):257202, 2012.

[119] M Evelt, C Safranski, Mohammed Aldosary, VE Demidov, I Barsukov, AP Nosov, AB Rinkevich, K Sobotkiewich, Xiaoqin Li, Jing Shi, et al. Spin hall-induced auto-oscillations in ultrathin yig grown on pt. *Scientific reports*, 8(1):1269, 2018.

[120] Chunhui Du, Toeno Van der Sar, Tony X Zhou, Pramey Upadhyaya, Francesco Casola, Huiliang Zhang, Mehmet C Onbasli, Caroline A Ross, Ronald L Walsworth, Yaroslav Tserkovnyak, et al. Control and local measurement of the spin chemical potential in a magnetic insulator. *Science*, 357(6347):195–198, 2017.

[121] VE Demidov, S Urazhdin, B Divinskiy, VD Bessonov, AB Rinkevich, VV Ustinov, and SO Demokritov. Chemical potential of quasi-equilibrium magnon gas driven by pure spin current. *Nature communications*, 8(1):1–7, 2017.

[122] Benedetta Flebus, Pramey Upadhyaya, Rembert A Duine, and Yaroslav Tserkovnyak. Local thermomagnonic torques in two-fluid spin dynamics. *Physical Review B*, 94(21): 214428, 2016.

[123] Benedetta Flebus, SA Bender, Yaroslav Tserkovnyak, and RA Duine. Two-fluid theory for spin superfluidity in magnetic insulators. *Physical review letters*, 116(11):117201, 2016.

[124] Yaroslav Tserkovnyak, Arne Brataas, and Gerrit EW Bauer. Spin pumping and magnetization dynamics in metallic multilayers. *Physical Review B*, 66(22):224403, 2002.

[125] Naoto Nagaosa and Yoshinori Tokura. Topological properties and dynamics of magnetic skyrmions. *Nature nanotechnology*, 8(12):899, 2013.

[126] David M Burn and Del Atkinson. Suppression of walker breakdown in magnetic domain wall propagation through structural control of spin wave emission. *Applied Physics Letters*, 102(24):242414, 2013.

[127] Yoko Yoshimura, Kab-Jin Kim, Takuya Taniguchi, Takayuki Tono, Kohei Ueda, Ryo Hiramatsu, Takahiro Moriyama, Keisuke Yamada, Yoshinobu Nakatani, and

Teruo Ono. Soliton-like magnetic domain wall motion induced by the interfacial dzyaloshinskii–moriya interaction. *Nature Physics*, 12(2):157–161, 2016.

[128] Seyed Majid Mohseni, SR Sani, J Persson, TN Anh Nguyen, Sunjae Chung, Ye Pogoryelov, PK Muduli, E Iacocca, A Eklund, RK Dumas, et al. Spin torque–generated magnetic droplet solitons. *Science*, 339(6125):1295–1298, 2013.

[129] M Karppinen and H Yamauchi. In frontiers in magnetic materials, edited by av narlikar, 2005.

[130] GD Fuchs, JC Sankey, VS Pribiag, L Qian, PM Braganca, AGF Garcia, EM Ryan, Zhi-Pan Li, O Ozatay, DC Ralph, et al. Spin-torque ferromagnetic resonance measurements of damping in nanomagnets. *Applied Physics Letters*, 91(6):062507, 2007.

[131] Chiara Battocchio. Advanced synchrotron radiation techniques for nanostructured materials, 2019.

[132] Maksym Sladkov. Electronic detection study of magnetization dynamics in ferromagnetic/nonmagnetic systems.

[133] IN Krivorotov, DV Berkov, NL Gorn, NC Emley, JC Sankey, DC Ralph, and RA Buhrman. Large-amplitude coherent spin waves excited by spin-polarized current in nanoscale spin valves. *Physical Review B*, 76(2):024418, 2007.

[134] M Gibertini, M Koperski, AF Morpurgo, and KS Novoselov. Magnetic 2d materials and heterostructures. *Nature nanotechnology*, 14(5):408–419, 2019.

[135] Yuan Liu, Yu Huang, and Xiangfeng Duan. Van der waals integration before and beyond two-dimensional materials. *Nature*, 567(7748):323–333, 2019.

[136] Zaiyao Fei, Bevin Huang, Paul Malinowski, Wenbo Wang, Tiancheng Song, Joshua Sanchez, Wang Yao, Di Xiao, Xiaoyang Zhu, Andrew F May, et al. Two-dimensional itinerant ferromagnetism in atomically thin fe 3 gete 2. *Nature materials*, 17(9): 778–782, 2018.

[137] Cheng Tan, Jinhwan Lee, Soon-Gil Jung, Tuson Park, Sultan Albarakati, James Partridge, Matthew R Field, Dougal G McCulloch, Lan Wang, and Changgu Lee. Hard magnetic properties in nanoflake van der waals fe 3 gete 2. *Nature communications*, 9(1):1–7, 2018.

[138] Yujun Deng, Yijun Yu, Yichen Song, Jingzhao Zhang, Nai Zhou Wang, Zeyuan Sun, Yangfan Yi, Yi Zheng Wu, Shiwei Wu, Junyi Zhu, et al. Gate-tunable room-temperature ferromagnetism in two-dimensional fe 3 gete 2. *Nature*, 563(7729):94–99, 2018.

[139] Andrew F May, Stuart Calder, Claudia Cantoni, Huibo Cao, and Michael A McGuire. Magnetic structure and phase stability of the van der waals bonded ferromagnet fe 3-x gete 2. *Physical Review B*, 93(1):014411, 2016.

[140] Shanshan Liu, Xiang Yuan, Yichao Zou, Yu Sheng, Ce Huang, Enze Zhang, Jiwei Ling, Yanwen Liu, Weiyi Wang, Cheng Zhang, et al. Wafer-scale two-dimensional ferromagnetic fe 3 gete 2 thin films grown by molecular beam epitaxy. *npj 2D Materials and Applications*, 1(1):1–7, 2017.

[141] Yihao Wang, Cong Xian, Jian Wang, Bingjie Liu, Langsheng Ling, Lei Zhang, Liang Cao, Zhe Qu, and Yimin Xiong. Anisotropic anomalous hall effect in triangular itinerant ferromagnet fe 3 gete 2. *Physical Review B*, 96(13):134428, 2017.

[142] R Narkowicz, D Suter, and I Niemeyer. Scaling of sensitivity and efficiency in planar microresonators for electron spin resonance. *Review of Scientific Instruments*, 79(8): 084702, 2008.

[143] R Narkowicz, H Ogata, E Reijerse, and D Suter. A cryogenic receiver for epr. *Journal of Magnetic Resonance*, 237:79–84, 2013.

[144] Ygal Twig, Ekaterina Suhovoy, and Aharon Blank. Sensitive surface loop-gap microresonators for electron spin resonance. *Review of Scientific Instruments*, 81(10): 104703, 2010.

[145] Mohammed Aldosary, Junxue Li, Chi Tang, Yadong Xu, Jian-Guo Zheng, Krassimir N Bozhilov, and Jing Shi. Platinum/yttrium iron garnet inverted structures for spin current transport. *Applied Physics Letters*, 108(24):242401, 2016.

[146] Jieyu Yi, Houlong Zhuang, Qiang Zou, Zhiming Wu, Guixin Cao, Siwei Tang, SA Calder, PRC Kent, David Mandrus, and Zheng Gai. Competing antiferromagnetism in a quasi-2d itinerant ferromagnet: Fe3gete2. *2D Materials*, 4(1), 2016.

Appendix A

MuMax^3 simulations codes

A.1 Py/YIG Nanowire

```
/*
*Py/YIG Nanowire simulations
*Full wire excitation with 5mT sinc pulse
*Code designed to capture information about spinwave modes
*/

/** GEOMETRY **/

length := 3.8e-6 // Sets X
Width := 190e-9 // Sets Y
thickness := 25e-9 // Sets Z

// Introduce thickness for Py and YIG layers.

t_Py := 5e-9
t_YIG := 20e-9

// Calculate relative postion in the grid since (0,0,0)
is located in the center of the world.
// Assuming  YIG is the bottom layer.
shift_up := thickness/2 - t_Py/2
shift_down := -(thickness)/2 + t_YIG/2

Nx := 1024 // Grid Size in X
Ny := 32 // Grid Size in Y
Nz := 5 // Grid Size in Z

SetGridSize(Nx, Ny, Nz) //
SetCellSize(length/Nx, width/Ny, thickness/Nz) //
```

```
// Provide variables for shape defintion.
This makes Defregion and SetGeom easier.

cuboid_py := cuboid(length, width, t_Py).transl(0,0,shift_up)
cuboid_yig := cuboid(length, width, t_YIG).transl(0,0,shift_down)

SetGeom(cuboid_py.add(cuboid_yig)) // Sets Geometry Type

// Define regions

DefRegion(0, cuboid_py)  // Py Layer
DefRegion(1, cuboid_yig)  // YIG Layer

/** END GEOMETRY **/

/** MATERIAL PARAMETERS **/

Msat.SetRegion(0, 800e3)  // Py Msat = 800,000 A/m @77K
Msat.SetRegion(1, 175e3)  // YIG Msat = 237,000 A/m @77K


Aex.SetRegion(0, 1.3e-11)
// Aex_Py = 1.3e-6 erg/cm --> 1e-6 erg/cm = 10 pJ/m
Aex.SetRegion(1, 3.5e-12)
// Aex_YIG = 3.5e-7 erg/cm --> 1e-6 erg/cm = 10 pJ/m


alphaFree := 0.01 // Used for f(H) sinc
alpha.SetRegion(0, alphaFree)
alpha.SetRegion(1, alphaFree)

Ku1.setregion(1, 5200)
anisU.setRegion(1, vector(0, 0, 1))

g_fct := 2.05 // Used average for Py and YIG
mu_B := 9.2740091523E-24
h_bar := 1.05457173E-34
GammaLL = (mu_B/h_bar)*g_fct

ext_scaleExchange(0, 1, 0.06)  // Manipulates Interlayer Exchange

//snapshot(regions)
//save(regions)
```

```
/** END MATERIAL PARAMETERS **/

/** f(H) SETTINGS **/

// Using mT because everything's in SI, program takes Tesla; 1 mT = 10 Oe
//Bmin:=0.0 //mT
//Bmax:=180.0 //mT
//Bstep:=10.0
//Bstepnum := (Bmax-Bmin)/Bstep
phi_H := 80 //0.1 // 0 degrees = x axis

f_cut := 20.0e9 //Hz
t_cut := 1/f_cut
t_sample := 0.5*t_cut
omega_cut := 2 * pi * f_cut

/** END f(H) SETTINGS **/

/** TABLE SETTINGS **/

tableadd(B_ext)
//tableadd(m.region(0))
//tableadd(m.region(1))
Bapp:=0.0
TableAddVar(Bapp,"Field","mT")
TableAddVar(phi_H,"phi_H","deg")
Amp := 0.005// T

/** END TABLE SETTINGS **/

/** EXCITATIONS **/

alpha = 0.5
print(Bapp)
B_ext.SetRegion(0, vector((Bapp)*cos(phi_H*pi/180)/1000,
(Bapp)*sin(phi_H*pi/180)/1000,  0))
B_ext.SetRegion(1, vector((Bapp)*cos(phi_H*pi/180)/1000,
(Bapp)*sin(phi_H*pi/180)/1000,  0))
// Start Ringdown

//save(m)  // Save Relaxed State

m.setRegion(0, uniform(cos(phi_H*pi/180), sin(phi_H*pi/180), 0))
```

```
m.setRegion(1, uniform(cos(phi_H*pi/180), sin(phi_H*pi/180), 0))
relax()

alpha = alphaFree

B_ext.SetRegion(0, vector((Bapp)*cos(phi_H*pi/180)/1000,
(Bapp)*sin(phi_H*pi/180)/1000,  Amp*sin(omega_cut*(t-5/f_cut))
/(omega_cut*(t-5/f_cut))))
B_ext.SetRegion(1, vector((Bapp)*cos(phi_H*pi/180)/1000,
(Bapp)*sin(phi_H*pi/180)/1000,  Amp*sin(omega_cut*(t-5/f_cut))
/(omega_cut*(t-5/f_cut))))

// There is no harm to save with a small time step for the table
tableautosave(5e-12)
autosave(m,10e-12)  //  Single Mode Only
run(25e-9)
t = floor(t)

/** END EXCITATIONS **/
```

A.2 Py/YIG Nanostructure

```
/*
*Py/YIG Nanowire simulations
*Full wire excitation with 5mT sinc pulse
*Code designed to capture information about spinwave modes
*/


/** GEOMETRY **/

length := 500e-9 // Sets X
Width := 200e-9 // Sets Y
thickness := 25e-9 // Sets Z

// Introduce thickness for Py and YIG layers.

t_Py := 5e-9
t_YIG := 20e-9

// Calculate relative postion in the grid since (0,0,0)
is located in the center of the world.
// Assuming  YIG is the bottom layer.
shift_up := thickness/2 - t_Py/2
```

```
shift_down := -(thickness)/2 + t_YIG/2

Nx := 100 // Grid Size in X
Ny := 40 // Grid Size in Y
Nz := 5 // Grid Size in Z

SetGridSize(Nx, Ny, Nz) //
SetCellSize(length/Nx, width/Ny, thickness/Nz) //
//SetPBC(5,5,0)


// Provide variables for shape defintion.
This makes Defregion and SetGeom easier.

cuboid_py := cuboid(length, width, t_Py).transl(0,0,shift_up)
cuboid_yig := cuboid(length, width, t_YIG).transl(0,0,shift_down)

SetGeom(cuboid_py.add(cuboid_yig)) // Sets Geometry Type

// Define regions

DefRegion(0, cuboid_py)  // Py Layer
DefRegion(1, cuboid_yig)  // YIG Layer


/** END GEOMETRY **/


/** MATERIAL PARAMETERS **/

Msat.SetRegion(0, 800e3)  // Py Msat = 800,000 A/m @77K
Msat.SetRegion(1, 235e3)  // YIG Msat = 237,000 A/m @77K


Aex.SetRegion(0, 1.3e-11)
// Aex_Py = 1.3e-6 erg/cm --> 1e-6 erg/cm = 10 pJ/m
Aex.SetRegion(1, 3.5e-12)
// Aex_YIG = 3.5e-7 erg/cm --> 1e-6 erg/cm = 10 pJ/m


alphaFree := 0.01 // Used for f(H) sinc
alpha.SetRegion(0, alphaFree)
alpha.SetRegion(1, alphaFree)
```

```
Ku1.setregion(1, 5200)
anisU.setRegion(1, vector(0, 0, 1))

g_fct := 2.05 // Used average for Py and YIG
mu_B := 9.2740091523E-24
h_bar := 1.05457173E-34
GammaLL = (mu_B/h_bar)*g_fct

ext_scaleExchange(0, 1, 0.06)  // Manipulates Interlayer Exchange

/** END MATERIAL PARAMETERS **/


/** f(H) SETTINGS **/

// Using mT because everything's in SI, program takes Tesla; 1 mT = 10 Oe
//Bmin:=0.0 //mT
//Bmax:=180.0 //mT
//Bstep:=10.0
//Bstepnum := (Bmax-Bmin)/Bstep
phi_H := 86 //0.1 // 0 degrees = x axis

f_cut := 20.0e9 //Hz
t_cut := 1/f_cut
t_sample := 0.5*t_cut
omega_cut := 2 * pi * f_cut

/** END f(H) SETTINGS **/


/** TABLE SETTINGS **/

tableadd(B_ext)
//tableadd(m.region(0))
//tableadd(m.region(1))
Bapp:=0.0
TableAddVar(Bapp,"Field","mT")
TableAddVar(phi_H,"phi_H","deg")
Amp := 0.005// T

/** END TABLE SETTINGS **/


/** EXCITATIONS **/
```

```
alpha = 0.5
print(Bapp)
B_ext.SetRegion(0, vector((Bapp)*cos(phi_H*pi/180)/1000,
(Bapp)*sin(phi_H*pi/180)/1000,  0))
B_ext.SetRegion(1, vector((Bapp)*cos(phi_H*pi/180)/1000,
(Bapp)*sin(phi_H*pi/180)/1000,  0))
// Start Ringdown

//save(m)  // Save Relaxed State

m.setRegion(0, uniform(cos(phi_H*pi/180), sin(phi_H*pi/180), 0))
m.setRegion(1, uniform(cos(phi_H*pi/180), sin(phi_H*pi/180), 0))
relax()

alpha = alphaFree


B_ext.SetRegion(0, vector((Bapp)*cos(phi_H*pi/180)/1000,
(Bapp)*sin(phi_H*pi/180)/1000,
Amp*sin(omega_cut*(t-5/f_cut))/(omega_cut*(t-5/f_cut))))
B_ext.SetRegion(1, vector((Bapp)*cos(phi_H*pi/180)/1000,
(Bapp)*sin(phi_H*pi/180)/1000,
Amp*sin(omega_cut*(t-5/f_cut))/(omega_cut*(t-5/f_cut))))

// There is no harm to save with a small time step for the table
tableautosave(5e-12)
autosave(m,10e-12)  //  Single Mode Only
run(25e-9)
t = floor(t)

/** END EXCITATIONS **/
```

Appendix B

E4407B Spectrum analyzer setting

B.1 Field-swept

- Span ⇒ Zero span
- Sweep ⇒ points(screen) ⇒ 401(numbers) ⇒ sweeptime(s) ⇒ 4.00ms
- System ⇒ Alignments ⇒ Auto Align ⇒ OFF
- BW/Avg ⇒ Average off
- Amplitude T-scale ⇒ Scale type ⇒ more ⇒ Y axis unit ⇒ Watts ⇒ Ref level ⇒ Scroll bottom (Note that: noise must be visible)

B.2 Frequency-swept

- Window ⇒ 1−3
- BW/Avg ⇒ Res BW=3.MHz, Video BW=3.0MHz, Average= on ⇒ 100
- System ⇒ Alignments ⇒ Auto Align ⇒ ON
- Sweeptime(s) ⇒ Cont
- Frequency ⇒ Manually ⇒ center freq: start freq: stop freq.

Appendix C

Fitting equation

C.1 Field-modulated FMR signal (H-domain)

```
2*aA*((1+4*((x-Br)/(2*s))^2)*(2*s))^(-1)
-8*sA*(x-Br)*(((1+4*((x-Br)/(2*s))^2)^2)*((2*s)^2))^(-1)
-16*aA*(x-Br)^2*(((1+4*((x-Br)/(2*s))^2)^2)*((2*s)^3))^(-1)
where,
Br = resonance field
sA = symmetric Lorentzian amplitude
aA = antisymmetric Lorentzian amplitude
s = Half Widthî Half Maxium linewidth (HWHM)

Anti-Symmetric -AHE-----Photovoltage (dispersive)
2*aA*((1+4*((x-Br)/(2*s))^2)*(2*s))^(-1)
-16*aA*(x-Br)^2*(((1+4*((x-Br)/(2*s))^2)^2)*((2*s)^3))^(-1)

Symmetric -SHE or ISHE---- Photoresistance (absorptive)
-8*sA*(x-Br)*(((1+4*((x-Br)/(2*s))^2)^2)*((2*s)^2))^(-1)
```

C.2 Frequency-modulated FMR signal (F-domain)

```
dSdB*(1+((x-fr)/s)^2)^(-1)
+dAdB*((x-fr)/s)*(1+((x-fr)/s)^2)^(-1)
+(1/s)*(2*SdfdB*
((1+((x-fr)/s)^2)^(-1))*
(((x-fr)/s)*(1+((x-fr)/s)^2)^(-1))
+AdfdB*((((x-fr)/s)*(1+((x-fr)/s)^2)^(-1))^(2)
-((1+((x-fr)/s)^2)^(-1))^(2))
+2*SdsdB*(((x-fr)/s)*(1+((x-fr)/s)^2)^(-1))^2
+AdsdB*(((x-fr)/s)*(1+((x-fr)/s)^2)^(-1))*(
(2*(((x-fr)/s)*(1+((x-fr)/s)^2)^(-1))^2)/
((1+((x-fr)/s)^2)^(-1))-1))
```

```
Note:
s = HWHM (half-width half-maximum)
fr = resonant frequency
```

C.3 Kittel equation (in-plane)

```
g*(1.3996245042181183e6)/1e9*sqrt((M-K+x)*(x-K))
where,
K=Anisotropy field
M=4piMeff
```

C.4 Kittel equation (out-of-plane)

```
g*(1.3996245042181183e6)/1e9*(x-M)
where,
M=4piMeff
```

C.5 Kittel equation (in-plane) for (111) orientation

```
(gamma/(2*pi)) * sqrt(
x*(x+uMeff) - B1 * sqrt(x*(x+uMeff)) + 14* (B1^2)
/ 9 + 32 * (B1^2) * cos(6*th*2*pi/360) / 9 )
where,
gamma=gyromagnetic ratio=g-factor*8794100.120472372752939715951173 6
uMeff=4piMeff
B1=Anisotropy field

Ref. Sethares J, Tsai T. Magnetic anisotropy of.
IEEE Transactions on Magnetics. 1977 Sep;13(5):1236-7.
```

C.6 Gilbert damping equation

```
714.4773451638277*(a/g)*x+b
where,
a=effective Gilbert damping
g=g-factor
b=inhomogeneous broadening
```

C.7 Two-magnon scattering equation

```
(Gamma)*(asin(sqrt((sqrt((6.28318530718*x*1e9)^2
+((g*8.794100120472373e6*M)/2)^2)-(g*8.794100120472373e6*M)/2)
/(sqrt((6.28318530718*x*1e9)^2+((g*8.794100120472373e6*M)/2)^2)
```

```
+(g*8.794100120472373e6*M)/2))))
where,
Gamma=Two-magnon scattering factor
g=g-factor
M=4piMeff
```

C.8 Spin pumping equation

```
Symmtric: [Spin-transfer torque (STT) - in-plane- Slonczewski---SHE]
(Vs / ( 1+(((x-Hr)^2)/S^2) ))

Anti-Symmetric: [Field-like Torque - (OOP----AHE)]
(Va* ((x-Hr)/S) / ( 1+(((x-Hr)^2)/S^2) ))

Sum:
(Vs / ( 1+(((x-Hr)^2)/S^2) ))+(Va* ((x-Hr)/S) / ( 1+(((x-Hr)^2)/S^2) ))
where,
Vs=Symmtric componen
Va=Anti-Symmetric
Hr=the resonant field
S=the linewidth
```